

EVALUATING SHALLOW CONVECTIVE MIXING AND PRECIPITATION PROCESSES  
USING ISOTOPE RATIOS IN WATER VAPOR

By

ADRIANA RAUDZENS BAILEY

B.Sc., Brown University, 2002

M.A., University of Colorado Boulder, 2010

A thesis submitted to the  
Faculty of the Graduate School of the  
University of Colorado in partial fulfillment  
of the requirement for the degree of  
Doctor of Philosophy  
Department of Atmospheric and Oceanic Sciences

2014

This thesis entitled:  
Evaluating Shallow Convective Mixing and Precipitation Processes  
Using Isotope Ratios in Water Vapor  
Written by Adriana Raudzens Bailey  
Has been approved for the Department of Atmospheric and Oceanic Sciences

---

Graham Feingold

---

David C. Noone

---

Balaji Rajagopalan

---

Karen Rosenlof

---

Darin W. Toohey

Date\_\_\_\_\_

The final copy of this thesis has been examined by the signatories, and we  
Find that both the content and the form meet acceptable presentation standards  
Of scholarly work in the above mentioned discipline.

Raudzens Bailey, Adriana (Ph.D., Atmospheric and Oceanic Sciences)

Evaluating Shallow Convective Mixing and Precipitation Processes Using Isotope Ratios in Water Vapor

Thesis directed by Associate Professor David C. Noone

Water vapor and clouds both respond to and influence global temperature. Consequently, understanding the processes that control humidity patterns and cloudiness is key for predicting future climate accurately. To elucidate the physical processes controlling water cycle feedbacks in the subtropics, this thesis applies new observational techniques to evaluate moisture and pollutant transport between the Hawaiian boundary layer—near ocean surface—and the dry free troposphere above. Beginning with a case study, paired measurements of humidity and the ratio of heavy-to-light oxygen isotopes in vapor are used to characterize vertical moisture transport as a simple mixing process. Strong mixing events are found to shape moisture transport for multiple days at a time, highlighting the need to understand which factors control the strength of convective mixing.

Large-scale dynamical controls on convective mixing near Hawaii are subsequently evaluated, and the relative importance of large-scale transport and microphysical processes in modifying humidity and pollutant distributions is investigated. Based on isotopic theory, strong convective events are classified as having either high or low precipitation efficiency. While the latter are associated with a branching of the subtropical jet, which facilitates advection of relatively high concentrations of methane and ozone from Eurasia, the former are associated with tropical plumes that transport relatively clean and moist air. Particle number concentrations, in comparison, exhibit clear sensitivity to the precipitation processes associated with convection, with higher precipitation efficiency events resulting in scavenging of pre-existing aerosol that, in

turn, appears to facilitate new particle formation at higher altitudes.

To determine whether the resultant variations in vertical distributions of moisture and pollutants influence cloud fields, isotopic retrievals from satellite are used to define precipitation efficiency over broader regions. Precipitation efficiency is shown to be a strong indicator of low-level cloud fraction but only in areas of active convection. This finding is consistent with the idea that as cloud evaporation is favored over precipitation, the resultant drying of the boundary layer inhibits low-cloud formation. The results thus provide critical observational constraints for future studies wishing to evaluate cloud feedbacks and, ultimately, climate model sensitivity.

## CONTENTS

### CHAPTER

I.	Introduction.....	1
II.	Characterizing moisture exchange between the Hawaiian convective boundary layer and free troposphere using stable isotopes in water.....	7
	1. Introduction.....	7
	2. Methods.....	10
	2.1. Instrumentation and configuration of sampling platform.....	10
	2.2. Isotopic calibrations.....	13
	2.3. Isotopic models for the convective boundary layer.....	17
	3. Results.....	21
	3.1. Moisture transport and stratification within the mixed layer.....	21
	3.1.1. Eastern mixed layer.....	21
	3.1.2. Western mixed layer.....	26
	3.2. Airmass mixing within the transition layer.....	29
	3.3. Processes influencing the moisture properties at CBL top.....	32
	4. Discussion.....	36
	5. Conclusion.....	39
III.	Considerations for the stability and calibration of laser absorption measurements of isotope ratios during long-term deployments.....	41
	1. Introduction.....	41
	2. Methods.....	45

2.1.	Instruments.....	45
2.2.	Mauna Loa, Hawaii.....	45
2.3.	Summit, Greenland .....	47
3.	Concentration-dependence.....	48
3.1.	Characterization .....	49
3.2.	Hysteresis.....	51
3.3.	Sensitivity to isotope ratio .....	55
3.4.	Long-term stability.....	56
4.	Isotopic drift.....	60
5.	Implications for field calibrations .....	66
IV.	Characterizing precipitation efficiency and distinguishing dynamical and microphysical controls on atmospheric constituents using isotope ratios in water vapor.....	71
1.	Introduction.....	71
2.	Methods.....	74
2.1.	Location .....	74
2.2.	Water vapor volume mixing ratio and isotope ratios.....	75
2.3.	Aerosols, ozone, and methane .....	76
2.4.	Reanalysis .....	77
2.5.	Precipitation efficiency .....	78
2.6.	Mixing model.....	79
3.	Results.....	83
3.1.	Strong and weak convection .....	83
3.2.	Large-scale controls on MLO convection.....	86

3.3.	Convective transport of atmospheric constituents .....	91
3.4.	Modeling convective transport for different precipitation efficiency.....	95
4.	Discussion .....	99
5.	Conclusion .....	103
V.	Linking precipitation efficiency and low-cloud cover using remotely-sensed isotope ratios in water vapor .....	106
1.	Introduction.....	106
2.	Data sets .....	109
2.1.	Remotely sensed isotope ratios.....	109
2.2.	Ground-based isotope ratios .....	110
2.3.	Remotely sensed cloud properties .....	111
3.	Results.....	111
3.1.	Linking precipitation efficiency and cloud cover near Hawaii .....	111
3.2.	Linking precipitation efficiency and cloud cover across four regions .....	115
4.	Discussion .....	122
5.	Conclusion .....	124
VI.	Conclusion .....	126
	BIBLIOGRPHAY .....	129
	APPENDIX	
A.	Uncertainties related to calibration choices .....	141

## TABLES

### CHAPTER II

- 2.1. Isotope ratio values of the five secondary standards used .....13
- 2.2. Coefficients of determination for the transition layers .....31

### CHAPTER III

- 3.1. Short-term isotopic drift for five distinct periods .....60
- 3.2. Long-term isotopic drift.....62

### CHAPTER IV

- 4.1. Best parameters for modeling high and low precipitation efficiency days.....96

### APPENDIX A

- A1. Percentage of the high or low precipitation efficiency events shared .....142

## FIGURES

### CHAPTER II

2.1.	Map of the Big Island of Hawaii.....	11
2.2.	The isotopic bias for raw $\delta^{18}\text{O}$ measurements .....	15
2.3.	The isotopic bias for raw $\delta\text{D}$ measurements.....	15
2.4.	Raw and corrected isotopic data .....	16
2.5.	An isotopic mixing diagram.....	20
2.6.	The first ten profiles with temperature, dew point temperature, and $\delta^{18}\text{O}$ .....	22
2.7.	Isotope ratio profiles on May 8 .....	24
2.8.	Isotopic mixing diagrams of the profiles shown in Figure 2.7 .....	26
2.9.	Aerosol number size distributions corresponding to Figure 2.7 .....	28
2.10.	An isotopic mixing diagram for nine profiles.....	30
2.11.	Aerosol number size distributions for select profiles .....	32
2.12.	Isotopic data and aerosols for the HIMK9 and MKSA9 profiles .....	34
2.13.	Wind direction as a function of height.....	35
2.14.	Two possible representations of the lower atmosphere near Hawaii.....	37

### CHAPTER III

3.1.	The total $\delta^{18}\text{O}$ bias for the Mauna Loa analyzer .....	50
3.2.	Fitting residuals as a function of the volume mixing ratio .....	50
3.3.	The $\delta^{18}\text{O}$ difference between various one-dimensional fitting procedures.....	52
3.4.	The $\delta^{18}\text{O}$ concentration-dependence for the Summit analyzers.....	53
3.5.	Characterizations with three different isotopic standards .....	56
3.6.	Characterizations for three-month periods.....	57

3.7.	Monthly mean $\delta^{18}\text{O}$ calibration points for the Summit analyzers .....	59
3.8.	Monthly mean $\delta\text{D}$ calibration points for the Summit analyzers .....	59
3.9.	Mauna Loa calibration points as a function of time .....	61
3.10.	The isotopic drift of the two Summit instruments .....	63
3.11.	Spiny deuterium excess, $\delta^{18}\text{O}$ , and $\delta\text{D}$ as a function of time.....	65

#### CHAPTER IV

4.1.	Profiles of the upward weighting function and modeled mixing ratio .....	82
4.2.	Frequency distributions of peak daytime and nighttime mixing ratios.....	84
4.3.	Bivariate frequency distributions of $q_{peak}$ and $\delta^{18}\text{O}_{peak}$ .....	85
4.4.	Bivariate distributions of $q$ and $\delta^{18}\text{O}$ for each hour of the day .....	86
4.5.	Composites of winds, total column water, and surface pressure .....	87
4.6.	Anomalies in winds, total column water, and surface pressure.....	88
4.7.	Three-day ensemble back trajectories.....	90
4.8.	Three-year means for each hour of the day representing diurnal cycles .....	93
4.9.	Initial vapor volume mixing ratio profiles used to model vertical mixing .....	97
4.10.	Observed and modeled diurnal cycles .....	98
4.11.	The Angstrom exponent.....	102

#### CHAPTER V

5.1.	Map of the four study regions.....	108
5.2.	Differences in cloud properties for high and low precipitation efficiency .....	112
5.3.	Differences in the fraction and cloud water path of low-level clouds .....	113
5.4.	Mean TES profiles near Hawaii.....	114
5.5.	Bivariate distributions of the $q$ and $\delta\text{D}$ profiles shown in Figure 5.4.....	115

5.6.	Distributions of the lower free tropospheric $\delta D$ value.....	116
5.7.	Maps of isotopic variables, low-cloud fraction, and vertical velocity.....	118
5.8.	Low-level cloud fraction versus the $\delta D$ gradient.....	119
5.9.	Low-level cloud fraction versus the lower free tropospheric $\delta D$ value.....	120
5.10.	The same as Figure 5.8 but for periods of active convection .....	121
5.11.	The same as Figure 5.9 but for periods of active convection .....	121

# CHAPTER I

## Introduction

Since the water cycle is integral to climate, moisture transport through convective mixing has important implications for future temperature change. As described by *Stevens* [2005], convection primarily transports boundary-layer moisture upwards through the formation of clouds, which evaporate—or detrain—into the drier free troposphere above. Since water vapor in the middle and upper free troposphere is particularly effective in absorbing and emitting thermal energy back towards Earth’s surface, moisture enhancements at these heights create a positive feedback on climate [*Held and Soden*, 2000]. There is large agreement that this feedback will double the warming caused by increasing carbon dioxide concentrations [*Held and Soden*, 2000; *Myhre et al.*, 2013].

As moist air is transported upward, warm and dry free tropospheric air is entrained, or drawn, downward. This process acts to increase surface temperatures and also decrease the relative humidity of the boundary layer. If the decrease in relative humidity is large enough, it will impede condensation and limit cloud formation. Computer simulations by *Rieck et al.* [2012], for instance, suggest stronger entrainment in a warmer climate will reduce the amount of low-level clouds—an alarming finding, since low-level clouds exert a cooling effect on Earth’s surface.

Problematically, models of varying resolution and complexity still struggle to represent the vertical exchange of moisture through convective mixing accurately. As a result, simulated climates remain highly sensitive to the way in which mixing between the boundary layer and free troposphere and mixing between low-level clouds and their dry environments are parameterized

[*Ayotte et al.*, 1996; *Hu et al.*, 2010; *Stevens*, 2002; *Zhao*, 2014]. *Stevens* [2005] discusses why this may be the case for the trade wind regime—where the moist boundary layer and dry free troposphere are separated by a sharp temperature inversion. There, a lack of understanding of the bulk atmospheric structure near the inversion layer may hamper accurate representations of convection.

Cloud processes associated with convection also present substantial challenges to modeling efforts and contribute some of the largest uncertainties to predictions of future temperature change [*Boucher et al.*, 2013]. As a case in point, *Sherwood et al.* [2014] argued that the large spread in climate model sensitivity, or the magnitude of the temperature response to a given greenhouse gas forcing, is controlled by lower-atmospheric mixing processes that regulate the efficiency with which low-level clouds detrain into their free tropospheric environment. Currently, the spread in climate sensitivity among general circulation models ranges from 2.1°C to 4.7°C [*Flato et al.*, 2013].

In addition to controlling humidity and cloud distributions, vertical-mixing processes also influence the distributions of other atmospheric constituents important for climate. Both observational [*Zhang and Rao*, 1999] and modeling studies [*Barth et al.*, 2002], for example, have shown that entrainment of ozone into the boundary layer can significantly increase ground-level concentrations. Convection also vents boundary-layer pollutants into the free troposphere [*Cotton et al.*, 1995]. Using large-eddy simulations to model the vertical transport of passive tracers, *Chen et al.* [2012] showed that shallow cumulus associated with moist convection loft pollutants more effectively than dry turbulent eddies.

However, it is not only the transport processes associated with moist convection that are important for pollutants like aerosol: cloud and precipitation processes can also fundamentally

change particle number size distributions. Some studies have observed reductions in small-particle concentrations and simultaneous enhancements in large-particle concentrations near evaporating clouds [Wonaschuetz *et al.*, 2012]. Others have suggested that precipitation helps scavenge pre-existing aerosol, which can facilitate new particle formation and increase concentrations of ultrafine particles [Clarke, 1993; Nilsson *et al.*, 2001]. In part, what makes aerosol-cloud interactions so complex is that while cloud and precipitation processes affect particle size distributions, aerosols also influence cloud and precipitation by altering cloud albedo [Twomey, 1977] and lifetime [Albrecht, 1989; Small *et al.*, 2009].

The complexity of these interactions and the small-scale at which they occur means that convective mixing, cloud processes, and precipitation are also notoriously difficult to observe. One approach for dealing with this problem is to use atmospheric tracers to characterize the bulk exchange of material in the vertical [e.g. Folkins *et al.*, 2006]. Betts and Albrecht [1979] epitomized this method by using conserved variables to model the convective boundary layer as a simple mixing line. This thesis considers whether another tracer—*isotope ratios in water vapor*—can accurately characterize convective mixing while providing additional information about cloud and precipitation processes and their effects on atmospheric constituents important for climate.

Isotopes of oxygen and hydrogen are powerful tracers of water cycle processes. Because isotopically heavy water vapor condenses preferentially [Bigeleisen, 1961; Dansgaard, 1964], paired measurements of humidity and the (heavy-to-light) isotope ratio in vapor distinguish air masses by their history of condensation and precipitation [Gat, 1996]. As a result, isotope ratios successfully distinguish the boundary layer and free troposphere and provide a way to capture mixing between these air masses [Noone *et al.*, 2011]. Within convective regions, isotope ratios

can also model the precipitation efficiency, or the efficiency with which cloud condensate is converted to precipitation [*Dansgaard, 1964; Jouzel and Merlivat, 1984; Noone, 2012*].

Consequently, it is expected that isotope ratios will shed light on the following key questions: how do convective mixing and the atmospheric structure of the trade wind regime influence one another?—how do vertical mixing processes alter the vertical distributions of moisture and other atmospheric constituents important for climate?—how does the efficiency with which cloud condensate forms precipitation modify particle size distributions and cloud fields?

This thesis attempts to answer these questions and demonstrate the utility of isotopic tracers for improving climate model simulations. The research is organized as follows. Chapter 2 describes a case study from the Big Island of Hawaii in which isotope ratios successfully model the transition layer—which develops, during convection, between the boundary layer and free troposphere—using a simple mixing line analysis. The results reveal that the mixing model is valid so long as the thermodynamic properties of the air mass at the top of the convective boundary layer are known. Deviations from the mixing line, meanwhile, identify thermodynamic boundaries in the atmospheric profile, which can persist from one day to the next. These findings indicate residual layers form during strong mixing events and regulate vertical moisture transport for multiple days at a time.

Chapter 3 explores the long-term stability of new laser absorption instruments used to measure water vapor isotope ratios in the field; and several calibration methods are evaluated to ensure that long-term measurements are precise and accurate. The analysis shows that one of the most effective ways to reduce measurement inaccuracies is to use an appropriate statistical-fitting procedure to characterize the isotopic dependence on water vapor concentration. Fortunately, these biases are stable in time, which suggests that the new technology is capable of

robustly evaluating multi-year relationships between isotope ratios and other meteorological variables.

Chapter 4 uses three years of isotope ratio measurements from Mauna Loa Observatory to characterize the precipitation efficiency of strong convection near Hawaii. Specifically, the effects of convective mixing and precipitation processes on vertical distributions of moisture, trace gases, and particle pollutants are examined. High and low precipitation efficiency events are found to occur under distinct synoptic regimes, with the former correlated with plume-like transport originating in the tropics and the latter associated with westerly transport, facilitated by a branching of the jet stream. While these distinct transport pathways modify the background concentrations of trace gases, particle number concentrations are found to be most sensitive to differences in local convection. During high precipitation efficiency events, for instance, rain likely scavenges pre-existing aerosol and facilitates new particle formation.

Chapter 5 extends the analysis of Chapter 4 by evaluating the effects of convective mixing and precipitation efficiency on low-level cloud fields. The results suggest that higher precipitation efficiency events near Hawaii are associated with greater low-level cloud cover. Moreover, deeper convection forms along a telltale southwesterly trajectory typical of moist tropical plumes. These relationships are evaluated more broadly by using remotely sensed isotope ratios across the Pacific Ocean. On average, precipitation efficiency is found to be a good indicator of low-cloud fraction only in regions of mean ascent, such as near the western Pacific warm pool. There, as the precipitation efficiency increases, so does the fraction of low-level cloud, which suggests that microphysical processes are important in determining cloud feedbacks on climate. Since a number of state-of-the-art climate models are now enabled with isotopic

tracers, metrics of precipitation efficiency, like those proposed here, may prove particularly useful for evaluating simulations and fine-tuning predictions of future climate.

Together, these chapters highlight the effects of large-scale dynamics and local atmospheric stability in regulating the exchange of moisture, trace gases, and aerosols between the boundary layer and free troposphere. They examine the relative importance of mixing and microphysical processes in modifying vertical distributions of these atmospheric constituents. And, they investigate the relationships among mixing, microphysics, and low-level cloud fields. Since moisture, trace gases, aerosols, and clouds all significantly influence climate, understanding how shallow convection influences their spatial and temporal distributions at a process-level is critical for improving model simulations and accurately predicting future temperature and hydrological changes.

## CHAPTER II

### Characterizing moisture exchange between the Hawaiian convective boundary layer and free troposphere using stable isotopes in water

#### 1. Introduction

The trade wind temperature inversion in the subtropics separates air masses representing two hydrological extremes: the moist marine boundary layer below and the dry free troposphere above. Shallow convection transports boundary layer moisture across the inversion, while boundary layer growth simultaneously entrains warm and dry free tropospheric air. Since these mechanisms regulate the vertical transport of energy, moisture, trace gases, and pollutants, they play a significant role in climate. Yet while numerous laboratory [Deardorff, 1980], observational [Nelson *et al.*, 1989; Lenschow *et al.*, 1999; Bretherton *et al.*, 1995; Faloona *et al.*, 2005; Träumner *et al.*, 2011], and modeling [Sullivan *et al.*, 1998; Brooks and Fowler, 2012] studies have investigated shallow convection and entrainment and their role in transporting material vertically, simulated climates remain sensitive to the choice of model parameterization [Ayotte *et al.*, 1996; Stevens, 2002; Hu *et al.*, 2010]. Such sensitivities suggest bulk features of vertical moisture exchange are still not fully understood. To improve our understanding of moisture transport processes in the subtropics, this study uses conserved variables to evaluate bulk mixing properties associated with the entrainment region near the top of the convective boundary layer (CBL). Our findings suggest the transition from boundary layer to free troposphere is well characterized as a simple mixing problem so long as the thermodynamic properties of the air mass at CBL top are known.

Conserved variable analyses provide a means to describe complex exchange processes in

terms of a simple mixing problem. *Betts and Albrecht* [1987] introduced a mixing line analysis to characterize shallow convective detrainment and entrainment in the CBL using a conserved variable diagram of total water mixing ratio ( $q_T$ ) and equivalent potential temperature ( $\theta_E$ ). In their approach, warm and moist tropical air from the well-mixed region of the boundary layer (i.e. the mixed layer) is represented by high  $q_T$  and high  $\theta_E$ . Deep convection, which transports mixed layer air upward via pseudoadiabatic motions, conserves  $\theta_E$  but reduces  $q_T$  by precipitation. Subsequent radiative cooling in the free troposphere decreases  $\theta_E$  but conserves  $q_T$ . In tandem, these processes establish the low  $q_T$ , low  $\theta_E$  values characteristic of air masses found at the top of the CBL. This free tropospheric air then mixes back into the boundary layer through entrainment, forming a transition layer characterized by a diagonal mixing line in  $q_T$ - $\theta_E$  space. *Betts and Albrecht* [1987] argued the thermodynamic properties of the air mass at CBL top are particularly important in shaping the slope of this mixing line, however their choice of tracers permitted only a cursory analysis of the origin of the dry end-member air mass.

The present study revisits the conserved variable analysis of the CBL in order to evaluate bulk thermodynamic features of the transition layer and identify sources of moisture to the air masses that bookend it. In contrast with *Betts and Albrecht's* [1987] work, the present analysis exploits stable isotope ratios in water as a tracer capable of distinguishing cloud processes and clear sky mixing. Because of saturation vapor pressure differences between heavy and light isotopologues, water vapor becomes depleted in isotopically heavy molecules during condensation and precipitation [*Bigeleisen*, 1961; *Dansgaard*, 1964]. As a result, stable isotope ratios in water help identify processes that moisten and dehydrate the atmosphere [*Worden et al.*, 2007; *Noone*, 2012] and distinguish air masses by their integrated condensation histories [*Gat*, 1996].

Various studies have used vapor isotope ratios to evaluate moist convective and mixing processes at multiple heights in the atmosphere. The departure of observed and simulated isotopic profiles from pseudoadiabatic models, for instance, suggests a role for lofting of frozen condensate by deep convection in moistening the upper troposphere [Nassar *et al.*, 2007; Bony *et al.*, 2008; Blossey *et al.*, 2010; Sayres *et al.*, 2010]. Gedzelman [1988] used isotope ratios in the lower and mid-free troposphere to distinguish air masses that had risen moist adiabatically but experienced different degrees of rainout and/or turbulent mixing. He also hypothesized that under certain advective conditions free tropospheric air masses conserve their isotopic composition, providing a robust tracer of atmospheric motions. This finding has since been supported by large-scale advection models that reproduce, to first order, the isotope ratios observed in the subtropical free troposphere near Hawaii [Galewsky *et al.*, 2007; Hurley *et al.*, 2012]. In addition, He and Smith [1999] characterized moisture transport between the land surface and free atmosphere by pairing measurements of humidity and the stable isotope ratio in a simple mixing model.

That isotope ratios distinguish air masses by their condensation histories and differentiate amongst moist convective and mixing processes enables the testing of several hypotheses regarding vertical moisture exchange in the subtropical CBL. We consider whether 1) the isotopic profile of the saturated mixed layer follows the Rayleigh distillation model predicted for pseudoadiabatic ascent, 2) the transition between mixed layer and free troposphere is accurately represented by a simple mixing process in terms of conserved isotopic variables, and 3) the top of the CBL is composed of free tropospheric air whose variations in isotope ratio are consistent with synoptic-scale transport. The desire to determine which processes control the isotopic structure of the air mass at CBL top builds on the expectation of Betts and Albrecht [1987] that

this air mass critically influences mixing between the boundary layer and free troposphere.

Vertical profile measurements of the water vapor mixing ratio ( $q$ ) and the stable isotope ratio  $^{18}\text{O}/^{16}\text{O}$  were made on the Big Island of Hawaii, May 6-9, 2010. Because of its remote Pacific setting and large vertical gain ( $\sim 4200$  m), the upper flanks of both Mauna Loa and Mauna Kea are exposed to free tropospheric air, while temperature and moisture at the Island's lower elevations are typical of the subtropical marine boundary layer. This unique geographical and topographical setting makes it possible to sample the transition layer with high frequency and high spatial resolution using ground-based instrumentation [Mendonca and Iwaoka, 1969].

## 2. Methods

### 2.1. Instrumentation and configuration of sampling platform

Measurements of the water vapor mixing ratio ( $q$ ), the oxygen and hydrogen isotope ratios, temperature, and submicron aerosol number size distributions were made during May 6-9, 2010 on the Big Island of Hawaii. Observed isotope ratios ( $obs$ ) are reported in the  $\delta$ -notation relative to Vienna Standard Mean Ocean Water ( $std$ ):

$$\delta D = \left( \frac{D/H_{obs}}{D/H_{std}} - 1 \right) \times 1000 \quad (2.1)$$

$$\delta^{18}O = \left( \frac{^{18}\text{O}/^{16}\text{O}_{obs}}{^{18}\text{O}/^{16}\text{O}_{std}} - 1 \right) \times 1000 \quad (2.2)$$

Vertical profiles were obtained by driving from sea level to either the summit of Mauna Kea (~4200 m) or the Mauna Loa Observatory (~3400 m). Both the eastern and western sides of the Island were profiled (Figure 2.1). Up to four profiles were driven each day, resulting in twelve profiles total. Because of nighttime driving restrictions near the astronomical observatory on Mauna Kea, two of the twelve profiles did not extend past the Mauna Kea Visitor Information Station (~2800 m). In addition, the last two profiles did not sample below the “Saddle,” the height of land on Route 200, commonly called Saddle Road (~2000 m).

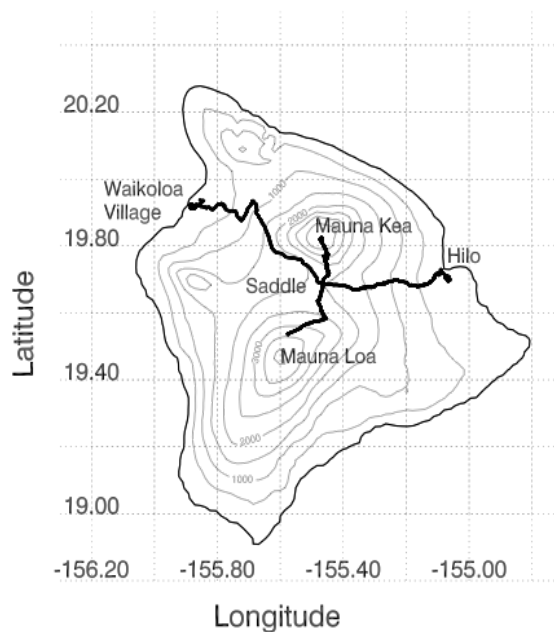


**Figure 2.1.** Map of the Big Island of Hawaii (topographic data source: [Amante and Eakins, 2009]). Profile starting and ending locations are labeled and driving routes measured by GPS are marked with solid lines.

The mixing ratio and isotope ratios were measured at 10-second frequency with a Picarro analyzer (the same instrument as Noone *et al.* [2013]), which uses cavity enhanced tunable diode laser absorption spectroscopy (Picarro model 1115-i, [Gupta *et al.*, 2009]). Submicron aerosol was measured across 99 diameter ranges spanning 55-1000 nm using a Particle Metrics Ultra-

High Sensitivity Aerosol Spectrometer (UHSAS, now sold by Droplet Measurement Technologies, Boulder, CO) [Yokelson *et al.*, 2007; Cai *et al.*, 2008]. Measurements of sub-micron aerosol number and size distributions were used to differentiate boundary layer and free tropospheric air masses and to assist in identification of cloud processes. Vehicle position and altitude were tracked with a Global Positioning System (GPS, Garmin model 60C). The Picarro and UHSAS were positioned inside the cab of a truck, and a 0.25-inch copper tube was strung through the rear passenger-side window for an inlet line. This line was nested inside a 1-inch schedule 80 polyvinylchloride (PVC) pipe, which was attached to the side of the vehicle to straighten the flow and reduce turbulence near the inlet. The inlet tip was angled backward to prevent rain drops and large debris from entering. Based on the pumping rate of the instruments, the flushing time of the inlet system was about one minute. (The elevation is not corrected for this time lag since the value is on the order of a few tens of meters, smaller than the error in the GPS-reported altitude.) A temperature probe was positioned within a second PVC pipe so that it was shielded from direct solar radiation. In addition, a LiCOR 7000 carbon dioxide and water vapor analyzer was operated to identify and exclude measurements affected by the exhaust of the truck and other vehicles on the road. The LiCOR measurements are not used otherwise or reported explicitly in this study.

In practice, the Picarro instrument measures the total of all moisture, including small cloud droplets that evaporate within the sampling system. Consequently, the Picarro vapor mixing ratio measurements ( $q$ ) should be nearly equivalent to the  $q_T$  measurements used by *Betts and Albrecht* [1987]. If the backward-facing inlet did reject some large cloud droplets, such a possibility does not critically change interpretation of the measurement. Indeed, *Albrecht et al.* [1979] suggested  $q$  is a reasonable approximation for  $q_T$  in conserved variable studies, and much

of the focus of this study is the unsaturated transition layer, where  $q$  and  $q_T$  are equal. Samples taken in rain and cloud are nevertheless flagged in the analysis for further discussion.

## 2.2. Isotopic calibrations

The isotopic measurements were calibrated to the SMOW-SLAP (Standard Mean Ocean Water – Standard Light Antarctic Precipitation) absolute isotopic scale [Coplen, 1994] using five secondary standards: Florida tap water; Boulder, Colorado tap water; water from West Antarctic Ice Sheet snow; water from Greenland snow; and water from surface snow from the Vostok drilling site in Antarctica. The isotopic values of these waters are shown in  $\delta$ -notation in Table 2.1. These secondary standards had been calibrated against International Atomic Energy Agency primary reference material on the University of Colorado Stable Isotope Laboratory’s Isotope Ratio Mass Spectrometer [B. Vaughn, *personal communication*, 2010].

**Table 2.1.** Isotope ratio values (permil) of the five secondary standards used to calibrate the Picarro vapor isotopic analyzer.

Standard Origin	$\delta^{18}\text{O}$	$\delta\text{D}$
Florida	-0.56	-3.75
Boulder	-14.88	-113.06
West Antarctica	-26.11	-204.06
Greenland	-38.45	-300.74
Vostok	-56.13	-427.52

Prior to field deployment, the secondary standards were measured on the vapor isotopic analyzer. A LEAP Technologies PAL auto-sampler was used to inject each standard by syringe into a Picarro vaporization module, which flash evaporated the liquid injection before delivery to

the Picarro instrument. Although *Schmidt et al.* [2010] found some difference in the way Picarro vapor isotopic analyzers measure  $\delta D$  when the sample is liquid versus vapor, no significant difference was found in  $\delta^{18}O$ . To reduce cross-contamination between standards, each standard was injected 15 times, and isotope ratios from the last four injections were averaged to determine the final measurement. A known concentration bias in the Picarro vapor isotopic analyzers causes the instrument to measure isotope ratios differently at both very low and very high humidity [*Schmidt et al.*, 2010; *Tremoy et al.*, 2011; *Aemisegger et al.*, 2012]. To account for this, the five waters were sampled at up to seven mixing ratios (approximately 0.3, 0.6, 1.2, 2.4, 3.3, 6.5, and 11.9 g/kg) that were generated by controlling the amount of liquid injected into the vaporizer.

Based on the 27 resulting calibration measurements, a locally-weighted second-degree polynomial in two dimensions was used to characterize the isotopic bias relative to the absolute SMOW-SLAP scale in terms of both the isotope ratio and water vapor mixing ratio. The locally-weighted surface was then used to predict isotopic biases for all combinations of isotope ratios and vapor mixing ratios measured in the field (Figure 2.2a-2.3a), and each field observation was corrected by subtracting its corresponding predicted bias. Standard errors from the prediction were used to characterize the uncertainty associated with the correction at each measurement point (Figure 2.2b-2.3b). At low humidity, such as observed on Mauna Kea's upper slopes, the isotopic bias can exceed 5.0 and 50.0 permil in  $\delta^{18}O$  and  $\delta D$ , respectively. The sign of the bias is instrument specific and differs between the two isotope ratios, a finding consistent with previous studies [*Tremoy et al.*, 2011; *Aemisegger et al.*, 2012]. Simultaneously correcting the concentration bias and performing the isotopic calibration in this manner, rather than in the step-wise fashion adopted by previous studies [*Schmidt et al.*, 2010; *Tremoy et al.*, 2011;

*Aemisegger et al.*, 2012; *Noone et al.*, 2013], was considered advantageous because it better accounts for covariation in measurement error in both humidity and isotope ratio, while avoiding the computational burden of Monte Carlo methods [cf. *Tremoy et al.*, 2011; *Noone et al.*, 2013].

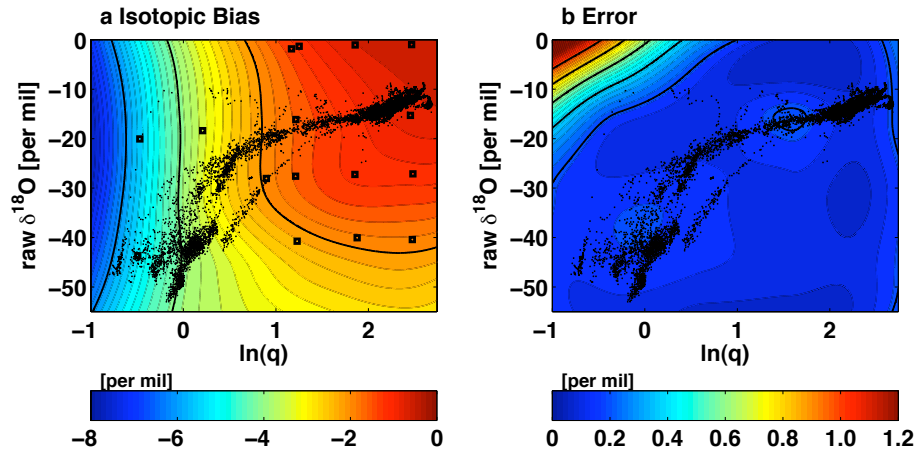


**Figure 2.2.** (a) The isotopic bias for raw  $\delta^{18}\text{O}$  measurements and (b) the errors associated with the bias characterization (permil) plotted as a function of both the raw isotopic value (permil) and the natural log of the vapor mixing ratio ( $q$ ) (g/kg). Contours are (a) every 2.0 permil and (b) 0.2 permil. The raw data (black dots) show the range of relevant biases. Nearby calibration points are represented by black squares on panel a.

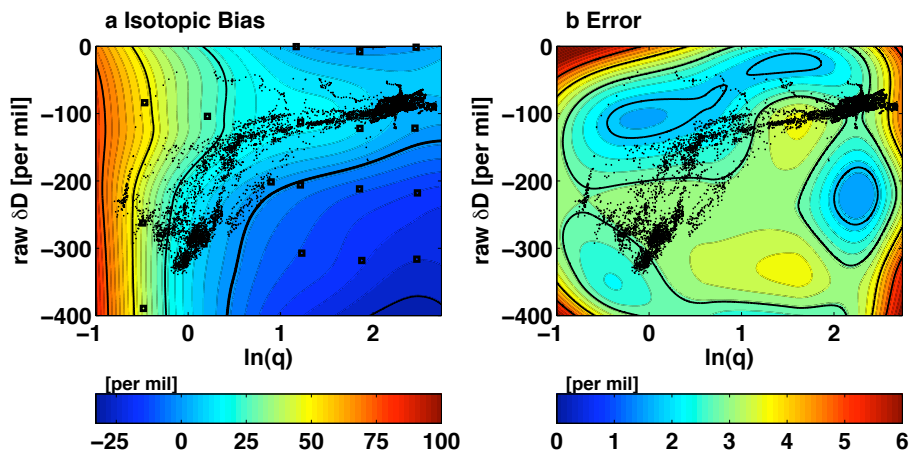


**Figure 2.3.** (a) The isotopic bias for raw  $\delta\text{D}$  measurements and (b) the errors associated with the bias characterization (permil) plotted as a function of both the raw isotopic value (permil) and the natural log of the vapor mixing ratio ( $q$ ) (g/kg). Contours are (a) every 25 permil, with the zero-line bolded, and (b) 5 permil. The raw data (black dots) show the range of relevant biases. Nearby calibration points are represented by black squares on panel a.

Nevertheless, the resulting analysis proves insensitive to subjective choices in the calibration procedure.

The dataset was further corrected by eliminating field measurements likely influenced by liquid water evaporation. These were identified by high values in either one isotope ratio or both. Since near-surface values are not the focus of this study, any measurements whose  $\delta D$  were higher than -60.0 permil or whose  $\delta^{18}O$  were higher than -6.0 permil were simply excluded from the analysis. Similarly, a handful of extreme outliers, whose absolute deuterium excess exceeded three standard deviations of the deuterium excess mean ( $0.0 \pm 17.0$  permil), were excluded. Figure 2.4 shows the effect of the calibration and data quality control procedures on the raw data. The large scatter is reduced, producing a linear regression of  $\delta D = 7.02 \times \delta^{18}O - 18.48$  (with an uncertainty on the slope of  $\pm 0.40$  and an uncertainty on the intercept of  $\pm 0.02$ ). This result differs from the 8:1 relationship typical of precipitation globally [Craig, 1961; Sharp, 2007], as expected for tropical locations [Dansgaard, 1964].

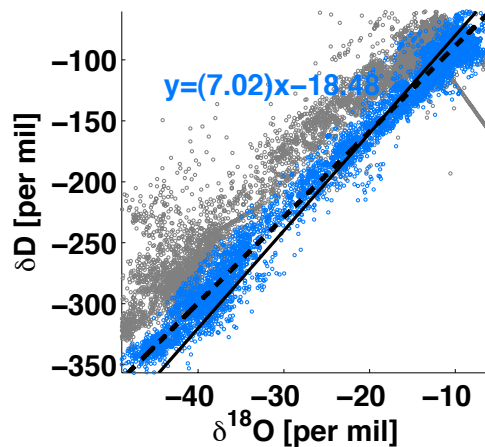


**Figure 2.4.** Raw (gray) and corrected (blue) isotopic data. The black line represents a meteoric water line with slope 8 and intercept 0. The dashed line is a simple linear regression fit to the corrected (blue) data.

Additional biases due to day-to-day drift while measuring in the field were not quantified, due to the impracticality of operating a syringe injection system while driving on dirt roads, however previous studies guide our expectation for drift. *Gupta et al.* [2009] found the same model Picarro instrument drifted by only 2.0 permil in  $\delta D$ —equivalent to an approximate 0.25 permil drift in  $\delta^{18}O$ —over a four-week period. Similarly, *Aemisegger et al.* [2012] detected a maximum drift in  $\delta^{18}O$  of 0.5 permil over a 14-day ambient sampling period. Therefore, to err on the side of caution, any differences in the corrected data less than 0.5 permil in  $\delta^{18}O$  are not considered significant.

Sensitivity analyses were also conducted to evaluate the effects of instrument operating temperature and the time rate of ambient pressure change, caused by driving up and down the Island, on the isotopic measurements. While the effects on  $\delta^{18}O$  measurements were found to be negligible, effects on  $\delta D$  boundary layer measurements were evident for one profile. As a result, and because  $\delta D$  exhibits a slower response time to ambient changes (a larger “memory effect”) and larger relative errors with calibration [*Schmidt et al.*, 2010; *Aemisegger et al.*, 2012],  $\delta^{18}O$  measurements are used preferentially throughout the analysis.

### ***2.3. Isotopic models for the convective boundary layer***

Due to differences in the saturation vapor pressures of heavy and light isotopologues of water [*Bigeleisen*, 1961], the relationship between the isotope ratio and observed vapor mixing ratio provide a valuable diagnostic for moisture fluxes [*Gat*, 1996; *He and Smith*, 1999; *Noone et al.*, 2011] and a means to distinguish moistening and dehydrating mechanisms [*Worden et al.*, 2007; *Noone*, 2012]. When conditions are unsaturated both  $q$  and the isotope ratio are conserved variables, and air mass mixing will cause observations to fall along a line in  $\delta-1/q$  space [e.g., *He*

and Smith, 1999; Noone et al., 2011]. In contrast, if an air mass experiences a pseudoadiabatic process, in which condensate is immediately removed as precipitation, its  $\delta$  value follows a theoretical Rayleigh distillation [e.g., Dansgaard, 1964]. By knowing  $q$ , temperature ( $T$ ), and the heavy-to-light isotope ratio ( $R$ ) at a certain height  $z_i$  and preceding height  $z_{i-1}$ , Rayleigh distillation predicts

$$R_i = R_{i-1} \left( \frac{q_i}{q_{i-1}} \right)^{\alpha-1} \quad (2.3)$$

where the subscripts  $i$  and  $i-1$  denote two points along the upward distillation trajectory. If condensation is slow and thermodynamically reversible,  $\alpha$  is the equilibrium fractionation factor, which determines the preferential removal of the heavy isotopes from the vapor phase as a function of  $T$ .  $T$  can be taken as the dew point temperature since  $q$  can be assumed at saturation during condensation. Furthermore, since all condensate is removed as precipitation,  $q$  is equivalent to  $q_T$ .

To account for the presence of cloud within an adiabatic plume, the Rayleigh model may be modified so that conversion of condensate to precipitation is less than 100% [Dansgaard, 1964; Jouzel and Merlivat, 1984; Noone, 2012]. By defining a precipitation efficiency parameter  $\epsilon$ , which varies from 0 if all condensate is held with the ascending vapor to 1 if all condensate is converted to precipitation, the isotope ratio of the vapor ( $R$ ) can be written for discrete vertical points in the profile as

$$R_i = R_{i-1} \left( \frac{q_i + \alpha(1-\varepsilon)(q_0 - q_i)}{q_{i-1} + \alpha(1-\varepsilon)(q_0 - q_{i-1})} \right)^{\frac{\alpha\varepsilon}{1-\alpha(1-\varepsilon)}-1} \quad (2.4)$$

(e.g. Noone 2012, Equation 11). A limitation of this model, however, is the assumption that the vapor and liquid components of an air mass are always distinct. If the cloud liquid re-evaporates at any point prior to observation or during sampling, as we expect was the case for our present experiment, then the isotope ratio measured will instead reflect a mixture of vapor and cloud. A better physical model for isotope ratio observations in the Hawaiian mixed layer is therefore given by a total water distillation (TWD) model:

$$R_T = (R_l l + R q) / (l + q). \quad (2.5)$$

Here,  $l+q=q_T$  is the total water remaining in the air mass after precipitation. The cloud liquid at any height is given by  $l = l_0 + (1-\varepsilon)(q_0 - q)$ , where the subscript 0 denotes the value at some initial point, and the isotope ratio of the cloud ( $R_l$ ) is simply a function of the equilibrium fractionation factor and the vapor isotope ratio predicted by Equation 2.4 (i.e.,  $R_l = \alpha R$ ). Note that in the case of a pseudoadiabatic process (i.e.  $\varepsilon = 1$  and  $l=0$ ), Equation 2.5 reduces to  $R_T = R$  and Equation 2.4 reduces to the Rayleigh distillation model of Equation 2.3.

Figure 2.5 illustrates the expected dehydration and depletion pathways of subtropical air masses for the different moist convective and mixing processes described. If mixed layer air rises pseudoadiabatically into the free troposphere and all condensate immediately precipitates (i.e.  $\varepsilon = 1$ ), the  $1/q$  and  $\delta$  values of the transition layer will follow the dashed curve expected for Rayleigh distillation (Equation 2.3). If instead some condensate is held with the vapor in an

adiabatic plume, total water isotope ratios will decrease less rapidly. The dotted curves show expected trajectories for air masses with precipitation efficiencies of 0.9 and 0.7. For a fully reversible moist adiabatic process, the total water and total water isotope ratio are conserved. On the other hand, if air mass mixing proves a better model for the vertical exchange of moisture between the boundary layer and free troposphere, then transition layer observations will form a straight line in the  $\delta-1/q$  space of the isotopic mixing diagram, similar to the  $q_T - \theta_E$  mixing line described by *Betts and Albrecht* [1987].

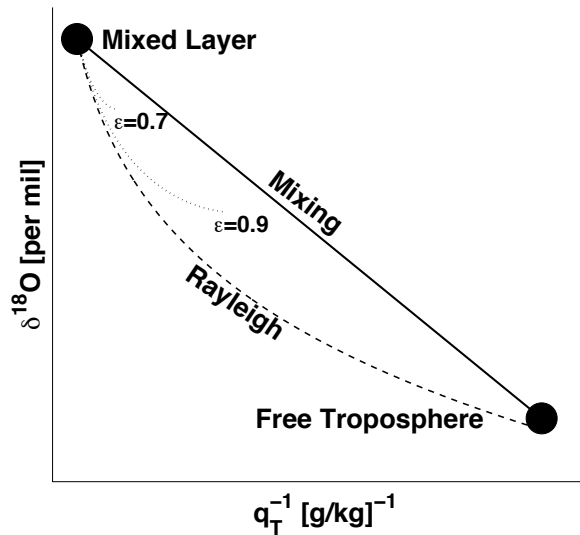


**Figure 2.5.** An isotopic mixing diagram of  $\delta^{18}\text{O}$  versus the inverse of the total water mixing ratio ( $q_T$ ). When mixed layer and free tropospheric air masses mix, observations fall along the straight (solid) line. Pseudoadiabatic processes result in Rayleigh distillation (dashed line), while moist adiabatic processes may follow one of the dotted lines, depending on their precipitation efficiency ( $\epsilon$ ). In a fully reversible moist adiabatic process ( $\epsilon=0$ ), the total water and total water isotope ratio are conserved.

### 3. Results

#### 3.1. Moisture transport and stratification within the mixed layer

To evaluate the processes regulating vertical moisture transport, we consider, in turn, moisture transport from the ocean surface to the top of the mixed layer and moisture transport from the top of the mixed layer, across the transition layer, to the top of the convective boundary layer (CBL). Ten vertical profiles of temperature, dew point temperature, and  $\delta^{18}\text{O}$  are shown in Figure 2.6. Dew point temperature is derived from the Picarro  $q$ , with hydrostatic pressure estimated from the GPS altitude. Each profile is labeled according to its geographic starting and ending points (HI = Hilo, MK = Mauna Kea Visitor Information Station or Summit, ML = Mauna Loa Observatory, WV = Waikoloa Village) and for the day in May 2010 on which measurements were taken. For instance, the first profile is labeled MLHI6, since it was obtained on May 6 by driving from Mauna Loa Observatory to Hilo, on the eastern side of the Big Island. Arrows indicate whether the profile was measured by driving from lower to higher elevations, and thus moist to dry conditions, or vice versa. Moist adiabatic models (dashed blue lines, Figure 2.6) were chosen to fit the regions below the trade wind inversion in which temperature and dew point converged to within 0.5 K, except in the cases of the WVMK7 and MKWV8 profiles, which were fit in discrete segments. Before fitting, the data were binned using a 25-m average. Two additional half profiles were obtained on May 9 by driving from Mauna Kea to the Saddle (MKSA9), and from the Saddle to the Mauna Loa Observatory (SAML9).

##### 3.1.1. Eastern Mixed Layer

Mixed layer air is readily identifiable by the gradual decrease in temperature, dew point temperature, and  $\delta^{18}\text{O}$  with height at altitudes below the level of the trade wind inversion,

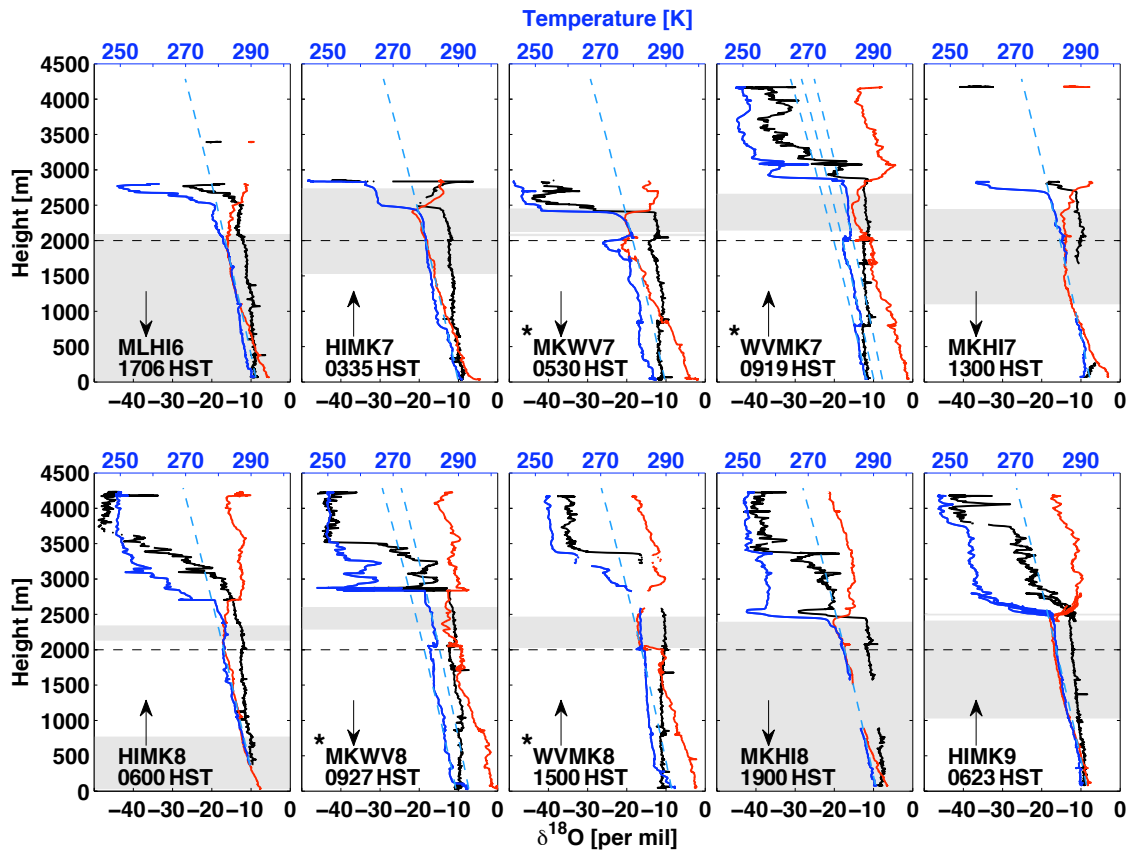


**Figure 2.6.** The first ten profiles with temperature (red), dew point temperature (blue), and  $\delta^{18}\text{O}$  (black) shown as a function of height. Modeled moist adiabats are shown as dashed blue lines. Arrows indicate the direction of profiling, and gray shading indicates regions where the vehicle passed through cloud or rain. The elevation of the Saddle (2000 m) is marked by the dashed black line. Profiles obtained from the Island’s dry west side are starred. Each profile is labeled according to its geographic starting and ending points (HI = Hilo, MK = Mauna Kea Visitor Information Station or Summit, ML = Mauna Loa Observatory, WV = Waikoloa Village) and for the day in May 2010 on which measurements were taken. For instance, the first profile is labeled MLHI6 because it was taken while driving from Mauna Loa Observatory to Hilo on May 6. Each profile is also labeled with the time at which sampling began (profiles took approximately two hours to complete).

however, there are clear differences in humidity structure between the east and west sides of the Island (Figure 2.6). On the east side of the Island (represented by the six Hilo profiles), a single moist adiabat describes each dew point profile to first order (root mean square error  $< 1.0$  K for the 500-2000 m layers of all but the HIMK7 profile). These findings are consistent with the

expectation that easterly trade winds force air up the orographic rise, maintaining the profile near saturation. As a result, the east side exhibits higher humidity, higher precipitation totals, and lush vegetation, compared with the Island's western slopes. A notable exception is the HIMK7 profile, in which dew point sharply decreases near 750 m and remains drier than the model adiabat to the Saddle at 2000 m. This discrepancy may result from nighttime stratification, since the profile was measured in the early hours before sunrise. Free air temperature measured by the Hilo radiosonde, launched at 0200 HST, also indicates multiple but weak stable layers below the inversion, which are no longer visible in the subsequent 1400 HST sounding (not shown).

Isotopic measurements confirm the importance of moist adiabatic processes in controlling the vertical humidity structure of the mixed layer on the Island's east side. Except for the MKHI7 profile, which was not modeled due to the lack of sufficient mixed layer isotope ratio data, isotopic profiles are matched by TWD models with precipitation efficiencies ( $\epsilon$ ) equal to or greater than 0.7. The HIMK8 profile is shown in Figure 2.7a as an example. Isotopic profiles were simultaneously fit above the lifting condensation level (LCL) using Equation 2.5 and below the LCL using a constant isotope ratio. Variables allowed to vary in the fitting were the LCL height, the  $\delta^{18}\text{O}$  value of the constant isotope ratio layer, and the precipitation efficiency ( $\epsilon$ ) in the layer of moist convection. The best parameters for each profile were selected by reducing the root mean square error of the fit for the 500-2000-m region. This region was selected to test adiabatic assumptions for each side of the Island separately—since above 2000 m the east and west air masses may converge—and to avoid heavily trafficked areas near the coast.

Though TWD models describe the eastern isotopic profiles to within 0.5 permil root mean square error over the 500-2000-m region, above the Saddle (2000 m) isotopic observations diverge from the modeled adiabatic profiles over a short but significant vertical distance. The

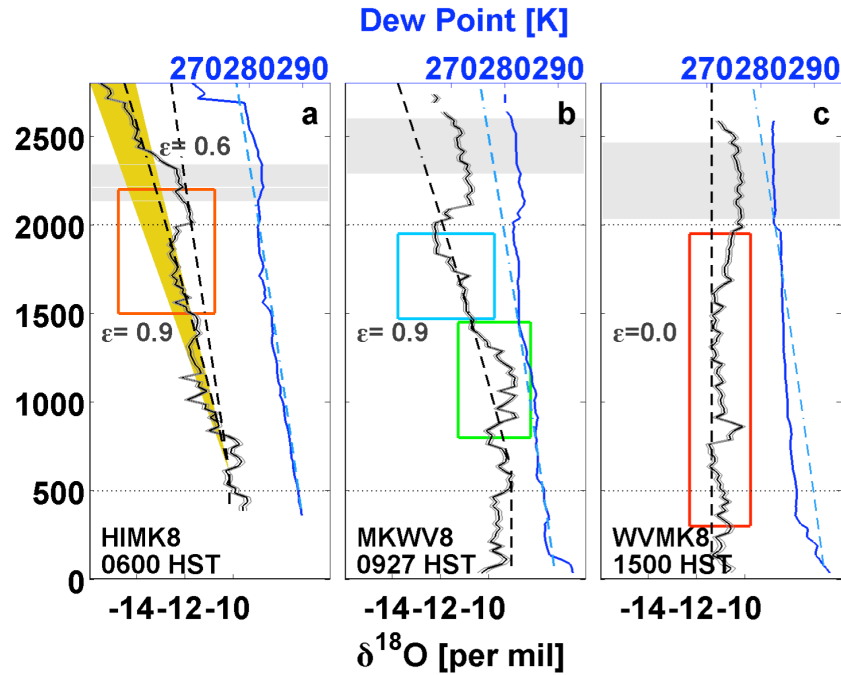


**Figure 2.7.** Isotope ratio profiles (solid black) with 1-sigma envelope (solid gray) from three distinct profiles on May 8: a) HIMK8, b) MKWV8, and c) WVMK8. The best fit total water distillation models (dashed black) for the 500-2000-m layer (bounded by dotted lines) are shown with their precipitation efficiencies ( $\epsilon$ ). Dew point profiles (solid blue) and moist adiabatic models (light blue dashed) are also shown for reference. Regions where the vehicle drove through cloud are shaded light gray. Yellow shading in panel (a) indicates the range of possible vapor-only models. The boxed regions are discussed in the text.

HIMK8 profile is a clear example (Figure 2.7a). In this profile, the  $\delta^{18}\text{O}$  value increases above the Saddle before returning to the predicted adiabatic value at higher altitudes. Note that this departure from the predicted profile is distinct from the large decrease in  $\delta^{18}\text{O}$  that occurs at 2700 m, associated with the transition to free tropospheric air. Instead, the layer of anomalously high  $\delta^{18}\text{O}$  near the Saddle coincides approximately, but not exactly, with the altitudes where the vehicle passed through cloud (indicated by gray shading in Figures 2.6 and 2.7).

The TWD model for the HIMK8 profile can be matched to the anomalous layer (2000-2300 m) to within 0.3 permil root mean square error if the precipitation efficiency is lowered to 0.6 (Figure 2.7a). This finding suggests less condensate was removed from this layer as

precipitation. Interestingly, the anomalously high  $\delta^{18}\text{O}$  signal is observed before the vehicle enters the cloud, which suggests some of the condensate re-evaporated within the Saddle region before the time of observation. Similar humidity “enhancements” have been documented around isolated cumulus clouds [Lu et al., 2003; Laird, 2005].

If instead of considering a TWD model, one considers a vapor-only model (Equation 2.4) for the HIMK8 profile, the predicted profile would fail to describe the 2000-2300-m layer no matter how much the precipitation efficiency were decreased. The yellow shading in Figure 2.7a shows the possible range of vapor isotope ratios predicted by Equation 2.4 using the same LCL height and  $\delta^{18}\text{O}$  value in the constant isotope ratio layer as selected for the best total-water fit. To match a vapor model to the 2000-2300-m layer would require increasing either the LCL height or its  $\delta^{18}\text{O}$  value, implying the anomalous air mass had lifted moist adiabatically at a different time or at a different location than the rest of the mixed layer profile. While either case is certainly possible, the fact that air masses above and below the anomalous layer can be explained by changing only the precipitation efficiency of the TWD model lends favor to the hypothesis that cloud re-evaporation humidified the Saddle region.

Thermodynamic boundaries within the HIMK8 profile can be assessed more readily by combining the  $\delta^{18}\text{O}$  and  $q$  characteristics of the mixed layer in a  $\delta^{18}\text{O}$ – $1/q$  isotopic mixing diagram. The orange data points in Figure 2.8a, which correspond to the boxed section of the atmospheric profile shown in Figure 2.7a, suggest condensate re-evaporation affects a deeper layer than Figure 2.7 indicates. The essential difference between these representations is that Figure 2.8 compares the adiabatic model with the isotope ratio and mixing ratio observations simultaneously, offering a more robust diagnostic of the water cycle histories of air masses than the isotope ratio alone.

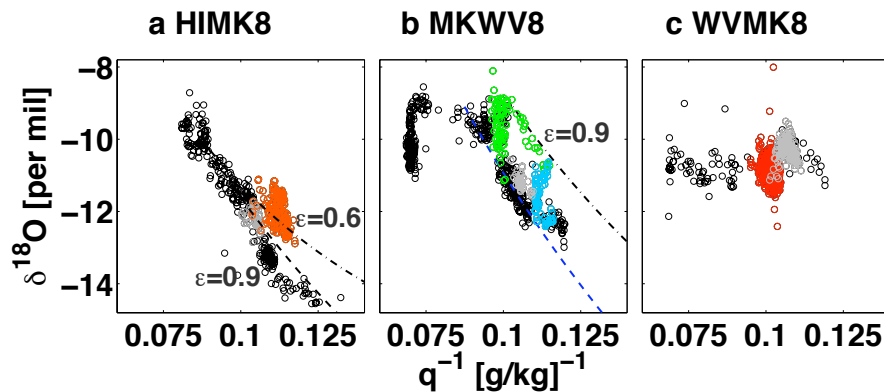


**Figure 2.8.** Isotopic mixing diagrams of the three mixed layer profiles shown in Figure 2.7: a) HIMK8, b) MKWV8, and c) WVMK8. In-cloud observations are shaded light gray. Orange, green, blue, and red shading correspond to the boxed sections of Figure 2.7. Modified distillation models with different precipitation efficiencies ( $\epsilon$ ) (dashed black) are shown in panels (a) and (b). The blue dashed line in panel (b) represents a hypothetical Rayleigh distillation that passes through the cloudy layer above the Saddle.

### 3.1.2. Western mixed layer

Because rainfall on the Big Island is chiefly controlled by orographic uplift and regional wind flow is predominantly easterly [Price and Pales, 1963], the mixed layer on the west side (the Waikoloa Village side) is climatologically drier than the mixed layer on the east side. As a result, western dew point temperature profiles from the May 2010 campaign exhibit greater stratification than the eastern profiles (Figure 2.6). Stable stratification is particularly evident in the early morning MKWV7 profile, whose dew point temperature, ambient temperature, and  $\delta^{18}\text{O}$  all decrease significantly in the layer below the Saddle. Although stratification persists and relative humidity remains low in mid-morning profiles WVMK7 and MKWV8, their dew point temperatures follow moist adiabatic lapse rates within discrete stable layers. (Figure 2.7b shows this in greater detail for the MKWV8 profile.) Such observations indicate a recent history of condensation and perhaps point to the east side as the origin of these air masses. Indeed, wind

fields around the Big Island provide a possible explanation for how eastern air masses may be transported to the west side: while the easterly trade winds split around the mountain barrier [Leopold, 1949; Garrett, 1980], turbulent vortices on the lee side cause easterly flowing air to reverse direction back towards the western coast [Yang *et al.*, 2008]. Furthermore, air masses that lose some condensate through precipitation—whether on the “rainy” east side or in another saturated environment—should preserve their adiabatic signature as they advect into the warmer, drier environment of the Island’s west coast, so long as they are not turbulently mixed. The western observations thus clearly show that moist convection influences the humidity structure of even the unsaturated regions of the mixed layer.

Differences in aerosol size distributions between the east and west sides of the Island further support the idea that moist convection sets the humidity structure of the west side. When a cloud evaporates, aerosol particle sizes should increase if droplets have been processed within the cloud, for example by coalescence [Hoppel *et al.*, 1986]. While aerosol number size distributions in the eastern mixed layer were always unimodal (within the detectable 55-1000-nm size range) with mean number diameters of ~130 nm (Figure 2.9), size distributions on the west side were frequently bi- or trimodal, exhibiting a pronounced mode at larger diameters (mean number diameters of ~300 nm) (Figure 2.9c). (Note that the measured aerosol diameters are distinctly larger than the marine boundary layer aerosol reported by Hoppel *et al.* [1986] in part because the aerosols were not dried prior to sampling by the UHSAS.) In the MKWV8 profile, for instance, the aerosol size distribution shows the pronounced 300-nm mode (blue shading, Figure 2.9c) where the isotopic profile is moist adiabatic (1450-1950 m, blue box, Figure 2.7b)—a finding consistent with the supposition that cloud droplets had coalesced before evaporating prior to observation—but is unimodal (green shading, Figure 2.9b) where the constant isotope

ratio with height indicates the boundary layer is fully mixed (800-1450 m, green box, Figure 2.7b). The  $\delta^{18}\text{O}-1/q$  mixing diagram, shown in Figure 2.8b, confirms that these adjacent sections of the profile are indeed distinct air masses.

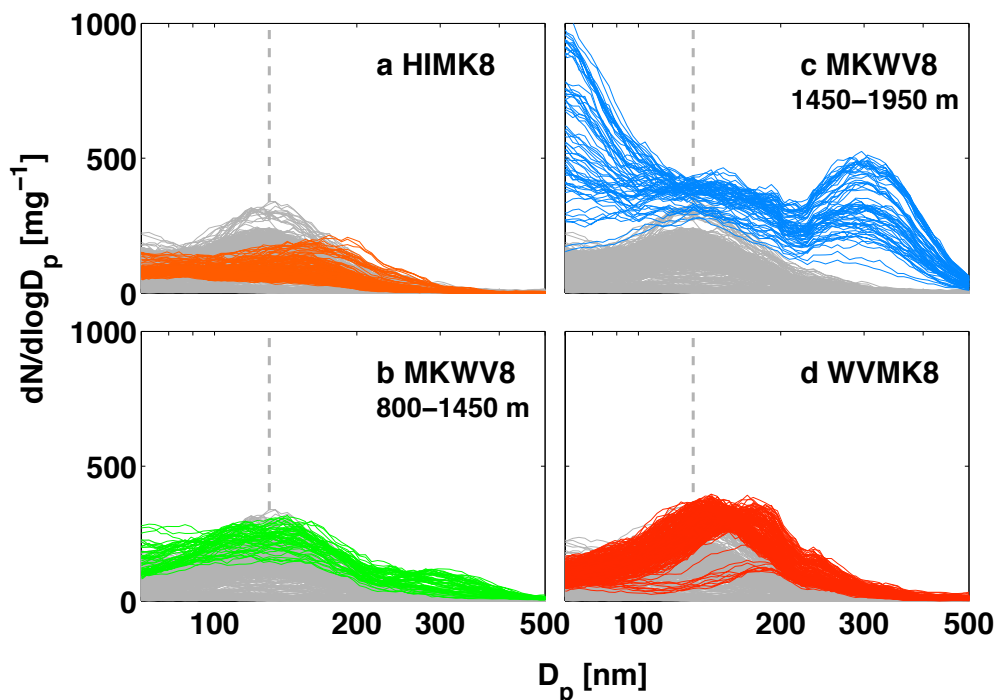


**Figure 2.9.** Aerosol number size distributions with 5-bin smoothing corresponding to the profile sections marked with boxes in Figure 2.7: a) HIMK8, b) MKWV8 lower profile, c) MKWV8 upper profile, and d) WVMK8. For comparison, May 7 and 9 aerosol size distributions sampled from the mixed layer of the east side of the Island are shown in light gray, and their mean size (130 nm) is marked by the gray dashed lines.

Once wind speed and dry turbulent mixing increased during the afternoon of May 8, the partly stratified MKWV8 profile was replaced by a constant isotopic profile (WVMK8, Figure 2.7c), and the disparate air masses highlighted on the isotopic mixing diagram were replaced by a single cluster of points (Figure 2.8c). Similarly, a unimodal aerosol size distribution was observed along the length of the mixed layer profile, including where a multi-modal distribution

had existed earlier (Figure 2.9d). These results suggest that because paired humidity and isotope ratio measurements distinguish atmospheric layers shaped by different moist convective and turbulent mixing processes, they can provide physical explanations for changes in aerosol observed. They also imply cloud re-evaporation and dry turbulent mixing can influence the humidity and isotopic composition of the base of the transition layer. A traditional Rayleigh model is therefore insufficient for characterizing moisture transport from the ocean surface to the top of the Hawaiian mixed layer; it cannot account for the discrete regions of airmass mixing observed.

### ***3.2. Airmass mixing within the transition layer***

Having established several mechanisms that influence the humidity and isotopic composition of the mixed layer, we now turn to evaluating the interaction between the mixed layer and free troposphere. Above the trade wind temperature inversion, the Hawaii dew point profiles clearly diverge from the moist adiabatic lapse rate and stabilize at very low values near the Mauna Kea summit (~4200m) (Figure 2.6). If moist convection were the dominant process transporting moisture above the inversion and into the lower free troposphere, the dew point temperature and  $\delta^{18}\text{O}$  should track the modeled moist adiabats and modified distillation models through the transition layer. Instead, both humidity and  $\delta^{18}\text{O}$  decline much more rapidly, as one might expect when mixing with very dry and depleted free tropospheric air occurs.

To test whether mixing is indeed the best model for moisture exchange between the boundary layer and free troposphere, the isotope ratio is plotted against the inverse of the vapor mixing ratio, and straight-line segments are identified. Figure 2.10 shows observations from nine

of the first ten profiles plotted on such an isotopic mixing diagram. The HIMK7 profile is excluded due to extensive inlet wetting when the vehicle passed through cloud.

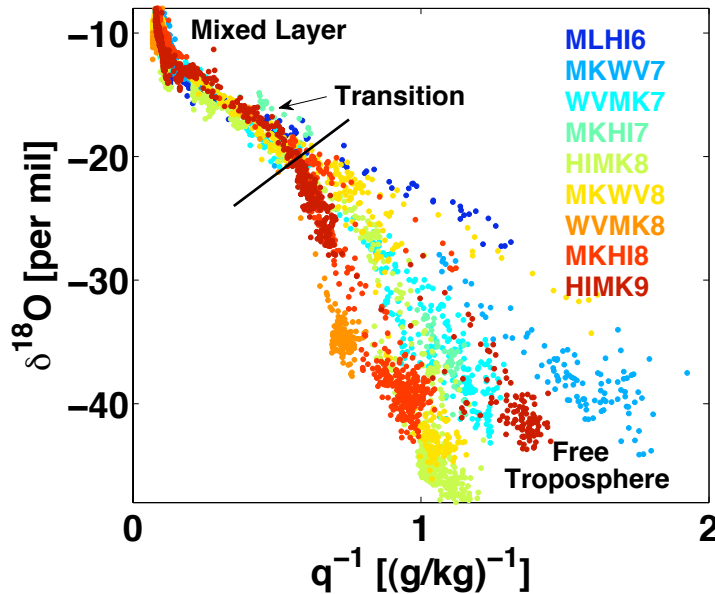


**Figure 2.10.** An isotopic mixing diagram for nine profiles. The transition layer is represented by the straight-line segments that lie largely to the left of the black line. Mauna Kea summit air masses are represented by the dry and isotopically depleted clusters to the right of the black line.

Contrary to expectation, in most profiles the region between the top of the mixed layer and the Mauna Kea summit (i.e. the driest and most depleted free tropospheric observations) is not well described by a single mixing line. Instead, the data are often characterized by bent-line structures, composed of multiple, adjoining straight-line segments. The approximate boundary between these segments is marked by a solid black line in Figure 2.10, however the exact location is profile dependent.

Straight-line segments to the left of the black line, in the region linking the top of the mixed layer with the free tropospheric air above the trade wind temperature inversion, are well described by simple linear regressions that are significant at the 0.01 level (Table 2.2).

(Observations from the top of the mixed layer were not included in the regressions to avoid inflating the  $r^2$  values.) Such high coefficients of determination confirm that mixing is a suitable model for vertical moisture exchange across the transition layer. In contrast the line segments to the right of the black line are not as well defined since they appear to represent vertical layering of free tropospheric air masses. Aerosol number size distributions provide supporting evidence. Within the transition layer, aerosol number size distributions span large ranges in number concentration, as might be expected with dilution or mixing (Figure 2.11). Above the transition layer (to the right of the black line), aerosol populations appear distinct and undiluted, as would be expected for distinct free tropospheric air masses.

**Table 2.2.** Coefficients of determination ( $r^2$ ) and number of points ( $n$ ) used in regressing the  $\delta^{18}\text{O}$  on  $1/q$  for the transition layers of the bent-line profiles shown in Figure 2.10.

<b>Profile</b>	<b><math>r^2</math></b>	<b><math>n</math></b>
MKHI7	0.91	23
HIMK8	0.98	149
MKWV8	0.96	203
WVMK8	- - -	0
MKHI8	0.96	21
HIMK9	0.81	123

Importantly, the isotopic mixing diagram shows that when the atmospheric profile above the mixed layer is characterized by a bent-line structure, the air at the top of the transition layer—the top of the CBL—is not the same air mass as that observed at the Mauna Kea summit. Variations in the vapor mixing ratio and  $\delta^{18}\text{O}$  of these distinct air masses reflect the diverse processes that regulate their thermodynamic properties.

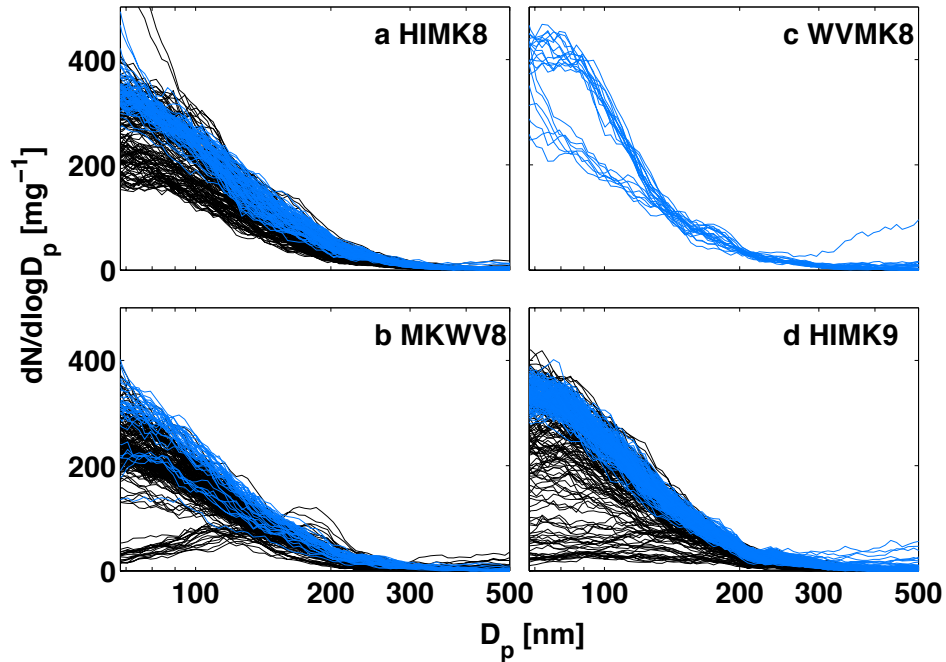


**Figure 2.11.** Aerosol number size distributions with 5-bin smoothing representing the transition layer (black) and free troposphere above (blue) for profiles a) HIMK8, b) MKWV8, c) WVMK8, and d) HIMK9.

### 3.3. Processes influencing the moisture properties at CBL top

Over the course of the four-day field campaign, the free tropospheric air near the Mauna Kea summit experienced large relative changes in humidity and isotope ratio. On hourly time scales, local vertical motions may have influenced the  $q$  and  $\delta^{18}\text{O}$  properties of this air mass. Close inspection of consecutive profiles HIMK8, MKWV8, WVMK8, and MKHI8, for instance, suggests variations in the summit air mass (isotopic range: -45.5 to -34.8 permil) aligned with a single vertical mixing line whose moist end-member was the subtropical mixed layer (Figure 2.10). On daily time scales, however,  $q - \delta^{18}\text{O}$  variability did not follow the same mixing pattern. Nor was it consistent with modified distillation expected during moist convection (refer to Figure

2.5). Instead, large variations along the x-axis in the isotopic mixing diagram (Figure 2.10) point to a probable role for large-scale transport, which previous studies have argued controls the isotopic composition of the free troposphere near Hawaii to first order [*Galewsky et al.*, 2007; *Noone et al.*, 2011; *Hurley et al.*, 2012].

Notably, the large variations in  $q$  and  $\delta^{18}\text{O}$  near the Mauna Kea summit had little effect on the air mass at CBL top. Variability in the latter was instead narrowly confined to the mixing line that defines the Hawaii transition layer, a behavior that suggests the mixing process influenced the  $q$  and  $\delta^{18}\text{O}$  properties of this air mass. The MKWV7 profile, for example, is the last profile in Figure 2.10 to exhibit a single straight-line structure. During subsequent profiles, the CBL top simply moves up and down the original MKWV7 mixing line, even as variations in air masses at higher elevation cause the “bend” to form on the isotopic mixing diagram. These findings suggest entrainment-mixing on May 7 set the  $q - \delta^{18}\text{O}$  composition of the air mass at CBL top, which then persisted as a residual layer through the morning of May 9. While vertical mixing remained weak during this period, the boundary layer would have entrained air from the residual layer rather than from the free troposphere above. Entrainment feedbacks on surface moisture and heat fluxes would have thus occurred in isolation of the free tropospheric changes driven by large-scale transport.

The development of strong convective mixing on May 9 eliminated evidence of the residual layer in the MKSA9 profile by resetting the thermodynamic structure of the transition layer. Figure 2.12 compares the MKSA9 profile (transition layer observed  $\sim 1000$  HST) with the preceding HIMK9 profile (transition layer observed  $\sim 0830$  HST); the MKSA9 profile shows a clear deepening of the transition layer by a full kilometer (Figure 2.12a). All observations above the mixed layer shift from a bent line to a straight line on the isotopic mixing diagram, and

clustering of these points near the moist end-member indicates dramatic humidification and enrichment of the upper slopes of Mauna Kea (Figure 2.12b). Changes in aerosol number size distributions are also consistent with stronger mixing and transition layer deepening (Figure 2.12c). During the early morning ascent of Mauna Kea (HIMK9), aerosol within the 2500-3700 m layer of the atmosphere were characterized by two largely distinct populations. By the time of the return trip down the mountain (MKSA9), a single gradient in number concentration was observed across this same vertical range.

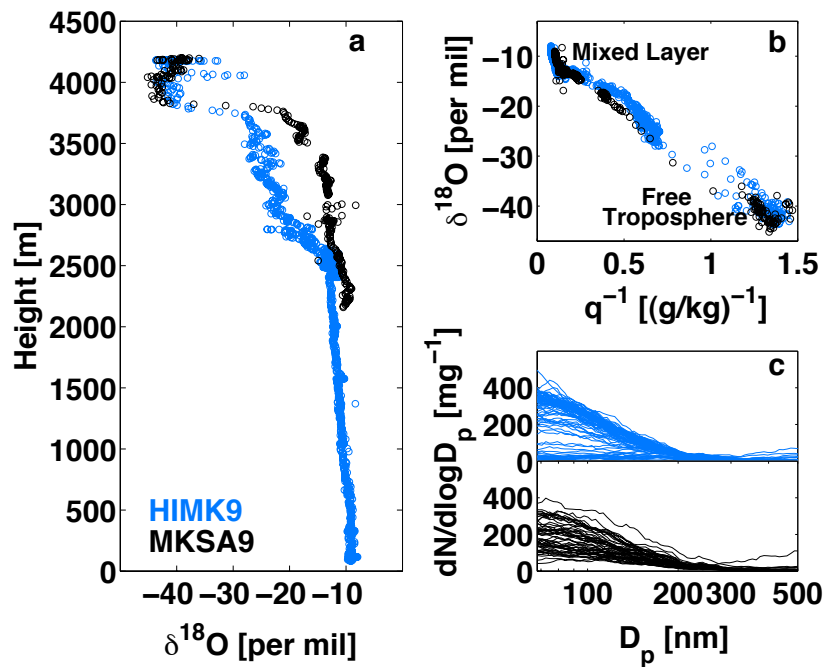


**Figure 2.12.** a) Isotopic profiles for the HIMK9 (blue) and MKSA9 (black) profiles, whose transition layers were observed at approximately 0830 and 1000 HST on May 9, respectively. b) On an isotopic mixing diagram, the HIMK9 profile shows a bent-line structure above the mixed layer while the MKSA9 profile is represented by a single straight-line. c) Their respective aerosol number size distributions (with 5-bin smoothing) in the 2500-3700 m layer.

Changes in wind profiles provide a possible physical explanation for the stronger mixing indicated by the isotope and aerosol data. The trade wind temperature inversion typically limits

convective activity on Hawaii's east side [Price and Pales, 1963; Garrett, 1980], however Noone *et al.* [2011] observed strong convective activity when regional winds shifted to southwesterly. Upper air radiosondes from Hilo show a clear westerly shift in the upper level wind direction on May 9 (Figure 2.13), which may have facilitated convective development throughout the morning. Though one coincident observation of a well-developed transition layer and a shift in upper level winds cannot test causality between regional wind flow and local convection, it nevertheless suggests future work should consider the effect of large-scale conditions in shaping entrainment-mixing and in setting the moisture properties of the residual layer that forms at CBL top.

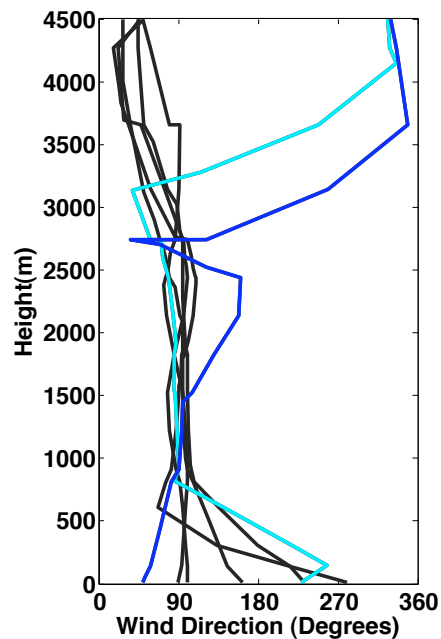


**Figure 2.13.** Wind direction as a function of height from the Hilo radiosondes for May 6-9, 2010. The aqua and blue profiles are the last two profiles for the period, launched at 0200 and 1400 HST, respectively, on May 9.

#### 4. Discussion

*Betts and Albrecht* [1987] suggested the dry air mass at CBL top was critical in determining the thermodynamic structure of mixing between the boundary layer and free troposphere. Our study affirms this hypothesis and also suggests the mixing process, in turn, influences the moisture properties of CBL top. In the MKWV7 and MKSA9 profiles, a single mixing line in  $\delta^{18}\text{O}-1/q$  space was observed to link the top of the mixed layer with the free tropospheric air near Mauna Kea. The slope of the CBL mixing line was therefore directly influenced by the isotopic composition of Hawaii's free troposphere (Figure 2.14a), which previous studies suggest is controlled to first order by large-scale transport [*Galewsky et al.*, 2007; *Noone et al.*, 2011; *Hurley et al.*, 2012]. In contrast, beginning with the WVMK7 profile and lasting until the HIMK9 profile, the top of the CBL was capped by a residual layer, whose isotopic composition had been influenced by previous mixing with the boundary layer (Figure 2.14b). These results imply that moisture properties at the top of the Hawaiian CBL can be set either by large-scale free tropospheric transport or by vertical mixing initiated by boundary layer convection. Assumptions that large-scale transport alone is responsible for the low humidity of the subtropical atmosphere clearly fail to account for the possible role of local vertical processes in moistening the climatically important free troposphere.

Whether or not residual layers cap the CBL appears to depend on the strength of entrainment-mixing. In the MKSA9 profile, strong convection caused a deep entrainment zone to develop, linking the top of the mixed layer with the free tropospheric air near the Island's summit. As all evidence of the residual layer was eliminated, upper-level winds concurrently

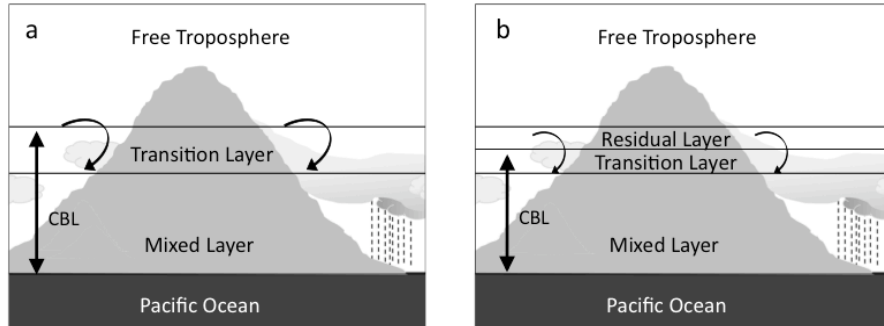


**Figure 2.14.** Two possible representations of the lower atmosphere near Hawaii (not to scale). In panel (a) the convective boundary layer (CBL) entrains air directly from the free troposphere, producing a single straight-line on an isotopic mixing diagram (see Figures 2.5 and 2.10). In panel (b) convective mixing is not as strong. The CBL entrains air from a residual layer formed during previous boundary layer growth. This, combined with free tropospheric advection, produces a bent-line structure on an isotopic mixing diagram.

shifted direction, suggesting a possible connection between free tropospheric dynamics and the strength of convection. Indeed, such a correlation is well supported by previous studies. While the trade wind inversion regulates convective strength on the Big Island [*Price and Pales*, 1963; *Garrett*, 1980], *Cao et al.* [2007] showed that synoptic conditions regulate the inversion. *Mendonca* [1969] further showed that stronger trade winds favor stronger convection on Hawaii. Yet it remains unclear whether changes in large-scale wind patterns are central to climatological moisture transport across the inversion layer. For this reason, testing the sensitivity of convective mixing to free tropospheric dynamics—using a longer isotopic observational dataset—would be an important direction for future study.

There are two principal reasons why isotopic “tracers” successfully track entrainment-mixing: their dynamic range at low humidity and their lifetime. The former makes it possible to differentiate air masses that have undergone unique dehydration histories despite being indistinguishable in terms of their vapor mixing ratios. On May 8, for instance, there were times

when the vapor mixing ratio at the top of the CBL was nearly identical to the vapor mixing ratio of the free tropospheric air near the Mauna Kea summit (Figure 2.10). Only in considering the isotope ratio was the CBL top identified as a distinct residual layer. Detection of this residual layer was also possible because vapor isotope ratios are conserved in the free troposphere unless altered by convective mixing or large-scale transport, precisely the processes expected to break up residual layers. Were isotope ratios characterized by a much larger time scale, the CBL top would tend toward a uniform  $\delta^{18}\text{O}$  value. A shorter time scale, and the isotopic signature of the residual layer would not persist from one day to the next.

In addition to characterizing the dry air mass at CBL top, isotope ratios provide valuable information about the processes that shape the moist air mass at the base of the transition layer. Using a total water distillation (TWD) model (in which the amount of condensate converted to precipitation is allowed to vary), adiabatic processes with different precipitation efficiencies were identified below the trade wind temperature inversion. Interestingly, a single  $\epsilon$  value was not always sufficient for describing adjacent sections of the same profile. In the HIMK8 mixed layer profile, for instance, adjacent layers were described by two distinct adiabatic models, with the lower precipitation efficiency model ( $\epsilon=0.6$ ) matching the layer in which cloud re-evaporation had likely occurred (Figure 2.8a). Although  $\epsilon=0.6$  produced the best fit for this layer, a model with  $\epsilon=0.7$  would have also produced a root mean square error less than 0.3. To distinguish amongst such models statistically, it will be necessary to reduce uncertainties in vapor isotope ratio measurements below 0.5 permil. Fortunately, rapid advancement in commercial isotope ratio measurement technologies has already resulted in substantial improvements in measurement precision.

One important remaining consideration is whether results from Hawaii may be extrapolated to the subtropics generally. Undoubtedly, radiative heating of the land during the day enhances convective development on the Island compared to the neighboring open ocean. Mechanical lifting may also cause air masses to slide upslope, creating an apparent CBL deepening due to the fact that ground-based measurements do not follow a truly vertical axis. For example, this study's *in situ* measurements identified the sharp changes in vapor mixing ratio and ambient temperature that mark the trade wind inversion as occurring at higher altitudes than free atmospheric measurements made by radiosonde indicate. *Mendonca and Iwaoka* [1969] found similar height differences between their on-island ground-based temperature measurements and off-island balloon soundings. Yet because such discrepancies primarily affect the absolute depths of the CBL and its transition layer, they are not necessarily relevant to the objectives of this study. Rather, the idea that vertical mixing processes observed on Hawaii are representative of the subtropics generally is demonstrated by the qualitative similarities between this work and the work of *Betts and Albrecht* [1987], whose dataset applies much more broadly to the tropical/subtropical region. In both studies, the transition layer near CBL top is characterized as a mixing line linking two distinct humidity regimes: the ocean-moistened mixed layer and the dehydrated free troposphere.

## **5. Conclusion**

This study has used stable isotope ratios in water to investigate processes that facilitate moisture transport from the ocean surface into the lower free troposphere near the Big Island of Hawaii. Below the trade wind temperature inversion, daytime isotopic profiles on the Island's

east side were always consistent with a moist adiabatic model of convection. Western profiles, in comparison, exhibited a range of stratification that varied daily, as well as evidence of dry turbulent mixing. Isotope ratios helped distinguish the influence of cloud processes and mixing on water vapor within the CBL, providing physical explanations for the dramatic differences in aerosol number size distributions observed. Moreover, since accounting for cloud condensate re-evaporation was important for explaining the isotope ratios measured near the top of the mixed layer, Rayleigh distillation proved inadequate for describing moisture transport within the Hawaiian boundary layer.

In contrast, moisture transport between the boundary layer and free troposphere was best characterized by a vertical mixing model, whose solution plots as a straight-line fit in the  $\delta^{18}\text{O}-1/q$  space of an isotopic mixing diagram. Deviations from the straight-line fit identified boundaries in the thermodynamic structure of the atmospheric profiles, marking, for example, residual layers that had formed during previous mixing events. Such residual layers capped the CBL in more than half the profiles sampled. During these periods, basic assumptions that synoptic-scale transport controls the air mass at CBL top were not sufficient for characterizing the vertical exchange of moisture in the lower subtropical atmosphere. Instead, it was the residual layer that shaped the mixing-line structure of the transition layer. Since strong mixing events likely set the residual layers that influence vertical mixing for multiple days at a time, understanding the factors that control the strength of convection is an important next step for predicting changes in vertical moisture transport between the subtropical boundary layer and free troposphere.

## CHAPTER III

### Considerations for the stability and calibration of laser absorption measurements of isotope ratios during long-term deployments

#### 1. Introduction

The isotope ratios of hydrogen and oxygen (D/H,  $^{18}\text{O}/^{16}\text{O}$ ) are powerful tracers of water cycle processes. Due to their lower saturation vapor pressure, the heavier isotopes (D and  $^{18}\text{O}$ ) preferentially condense, while the lighter isotopes preferentially evaporate [Bigeleisen, 1961; Dansgaard, 1964]. Paired with humidity information, isotope ratios thus provide clues about sources of moisture to the atmosphere and about the integrated condensation history of air masses [Gat, 1996].

With the recent advent of commercial vapor isotopic analyzers, measurements of isotope ratios in water vapor have become increasingly widespread. As a result, field experiments once limited to a small number of flask samples [e.g. Ehhalt, 1974; Galewsky *et al.*, 2007]—whose vapor content must be captured through a cryogenic trap for later liquid analysis in the lab—have been replaced by field experiments in which thousands of *in situ* observations are made continuously and in real time. Researchers using these new commercial technologies are resolving water cycle processes on a range of local-to-regional scales, investigating, for example, water recycling within the forest canopy [Berkelhammer *et al.*, 2013], evapotranspiration [Wang *et al.*, 2010] and its contribution to atmospheric moisture [Noone *et al.*, 2013; Aemiseggar *et al.*, 2014], mixing and convective processes in the atmosphere [Noone *et al.*, 2011; Tremoy *et al.*, 2012; Bailey *et al.*, 2013], and large-scale condensation and advection dynamics [Galewsky *et al.*, 2011; Hurley *et al.*, 2012; Steen-Larsen *et al.*, 2013].

Lessons learned from these early field programs are informing designs for longer-term observational campaigns, including the National Ecological Observatory Network's (NEON) plans to measure vapor isotope ratios for three decades at sites across the United States. Yet questions still remain about the long-term stability and absolute scaling of isotopic measurements made by commercial spectroscopy and, consequently, about the best approaches for calibrating in the field to ensure high-quality long time series. The goal of this chapter is to provide guidance for field deployments by evaluating the stability of the isotopic biases identified in three spectroscopic isotopic analyzers, made by Picarro, Inc., for periods of up to three years. In addition, the sensitivity of the observations to various calibration approaches is assessed.

While previous studies suggest isotopic biases are specific to each individual commercial analyzer [e.g. *Tremoy et al.*, 2011; *Aemisegger et al.*, 2012; *Wen et al.*, 2012], there are nevertheless shared characteristics upon which “best practices” for instrument operation and calibration can be based. Most prominent is the shared tendency for the isotope ratio measured to change as a function of the vapor volume mixing ratio, creating a so-called “concentration-dependence,” which numerous studies describe [e.g. *Lis et al.*, 2008; *Sturm and Knohl*, 2010; *Johnson et al.*, 2011; *Noone et al.*, 2011; *Rambo et al.*, 2011; *Tremoy et al.*, 2011; *Aemisegger et al.*, 2012; *Wen et al.*, 2012; *Bailey et al.*, 2013; *Noone et al.*, 2013; *Steen-Larsen et al.*, 2013]. While a few have found the concentration-dependence to be near linear [cf. *Lis et al.*, 2008; *Wen et al.*, 2012], most have found it to be non-linear and specific to both the instrument used and the isotope ratio measured (i.e.  $\delta\text{D}$  or  $\delta^{18}\text{O}$ , where  $\delta = (R_{\text{observed}}/R_{\text{standard}} - 1) \times 1000$  and  $R = \text{D/H}$  or  $^{18}\text{O}/^{16}\text{O}$ ). Moreover, biases in the individual isotope ratios can be quite significant: *Sturm and Knohl* [2010] showed that failing to account for the concentration-dependence of their analyzer

resulted in a bias in the second-order deuterium excess parameter ( $d = \delta D - 8 \times \delta^{18}O$ ) of upwards of 25 permil.

Though in principle characterizing the concentration-dependence can be achieved by measuring a standard of known isotope ratio across a range of vapor volume mixing ratios, in practice the characterization may be complicated by hysteresis, caused by water sticking to either the instrument cavities or inlet materials. Calibration tests using flash-evaporated, liquid isotopic standards have demonstrated that “memory effects” frequently affect the first injections following a change in standard water [Lis *et al.*, 2008; Gröning, 2011; van Gelden and Barth, 2012]. Other studies have shown that the inlet tubing material can slow the analyzer’s response time, with synflex particularly problematic for  $\delta D$  [Tremoy *et al.*, 2011]. Sturm and Knohl [2010] speculated that failing to account for such measurement inaccuracies might result in a poor characterization of the concentration-dependence and, ultimately, influence interpretation of scientific results.

Additional isotopic biases indicate deviations from the VSMOW (Vienna Standard Mean Ocean Water)-SLAP (Standard Light Antarctic Precipitation) scale [cf. Gröning, 2011]. These are characterized by fitting a simple linear regression between the known values of two (or more) standards and the isotope ratios measured by the instrument [cf. Tanweer *et al.*, 2009]. The precision of this bias is typically monitored by measuring the same isotopic standard at a constant humidity level at regular time intervals. Using such an approach, some studies have found no significant drift over multiple hours [Kohler and Wasenaar, 2011; van Geldern and Barth, 2012], while others claim significant variability in sample reproducibility on daily timescales [Gupta *et al.*, 2009; Tremoy *et al.*, 2011; Aemisegger *et al.*, 2012]. Steen-Larsen *et al.* [2013], for instance, reported large daily variability—as high as 4 permil in  $\delta^{18}O$  and 16 permil

in  $\delta D$ —and observed seasonal drift in one of two isotope ratios and one of two instruments deployed. *Sturm and Knohl* [2010] similarly observed consistent enrichment in one isotope ratio over the course of two weeks but no change in the other. Possible sources of such imprecision may be instrument sensitivities to fluctuations in ambient temperature [*Sturm and Knohl*, 2010; *Rambo et al.*, 2011] or uncertainties in the characterization of the concentration-dependence with time [*Sturm and Knohl*, 2010].

One common approach to calibrating spectroscopic isotopic measurements is to account first for the concentration-dependence and subsequently adjust the concentration-corrected isotopic measurements to the VSMOW-SLAP scale [e.g. *Noone et al.*, 2013; *Steen-Larsen et al.*, 2013]. However, it is also possible to account for all biases simultaneously. *Bailey et al.* [2013] demonstrated the latter by fitting a surface to isotopic biases as a function of the vapor volume mixing ratio and isotope ratio observed. These approaches may provide different estimates of calibration uncertainty if errors are estimated jointly or summed in quadrature.

Building on these previous analyses, this study extends our understanding of long-term stability in vapor isotopic analyzers by evaluating first whether there are significant changes in the concentration-dependence with time, and whether these changes are exacerbated by curve-fitting inaccuracies or measurement hysteresis. Second, isotopic deviation from the VSMOW-SLAP scale is examined over periods of 6 to 36 months. In light of plans to develop baseline measurements of isotope ratios in vapor over several decades, identifying and characterizing instrument-sensitivities on these longer time scales is critical. Recommendations for calibration strategies are discussed in the conclusions of this chapter.

## 2. Methods

The primary data for this study were collected using three Picarro, Inc. vapor isotopic analyzers, which were operated at two baseline observatories: the Mauna Loa Observatory (3400m) on the Big Island of Hawaii and the Greenland Environmental Observatory (3200 m) at Summit, Greenland.

### 2.1. Instruments

Picarro's spectroscopic analyzers are one of several available commercial vapor isotopic analyzers based on cavity-enhanced near-infrared laser absorption spectroscopy. Los Gatos Research, Inc. also makes an analyzer used widely in the field [e.g. *Noone et al.*, 2011; *Rambo et al.*, 2011]. These instruments exploit near-infrared light to measure the absorption spectra of three water isotopologues:  $^1\text{H}_2\text{}^{16}\text{O}$ ,  $^1\text{H}^2\text{H}^{16}\text{O}$  (i.e.  $^1\text{HD}^{16}\text{O}$ ), and  $^1\text{H}_2\text{}^{18}\text{O}$ . Cavity-enhanced techniques help create a longer effective absorption path length, which mitigates for the very weak absorption of water vapor isotopologues in the near infrared. This approach contrasts with mid-infrared isotopic analyzers (e.g. Aerodyne Research, Inc.'s), which take advantage of water vapor's stronger absorption at longer wavelengths.

### 2.2. Mauna Loa, Hawaii

Beginning during the fall of 2010, water vapor isotope ratios have been measured at the Mauna Loa Observatory (MLO) with a Picarro analyzer model L1115-i. The instrument, which is housed in the Charles Keeling building at the observatory, samples ambient air through 0.25-inch stainless steel tubing at a rate of approximately 300 cc/min. The stainless steel tubing protrudes through the roof of the building, through a plastic pipe, which has a rain cap to prevent

precipitation from entering. The bulk of the stainless steel inlet line is housed inside the building and thus maintained at room temperature, which far exceeds the ambient dew point.

To quality-control the vapor volume mixing ratio measurements ( $q$ ), the data were compared with MLO's hourly-averaged dew point values, which are measured by hygrometer. A simple linear regression between the two data sets—after converting the MLO dew points to volume mixing ratios and averaging and interpolating the Picarro data—produced a slope of 1.00, and an offset of 0.33 mmol/mol. This suggests a small uniform low bias in the uncalibrated  $q$  measurements. However, since the accuracy of the MLO humidity measurements is not fully known, no adjustments were made to the H<sub>2</sub>O volume mixing ratio data.

For most of the instrument's deployment, the isotopic measurements have been calibrated weekly using a LEAP Technologies PAL (Prep and Load) autosampler. Liquid samples from secondary standards spanning approximately -45 to 0 permil in  $\delta^{18}\text{O}$  and -355 to 0 permil in  $\delta\text{D}$  are injected by syringe into a vaporizer, which flash evaporates the liquid in a mixture of zero-grade dry air before delivery to the instrument. The volume of water injected controls the mixing ratio of the sample. One standard is injected 18 times at a variety of humidity levels, typically spanning 2-20 mmol/mol, and a second standard is injected 6 times at a humidity level near 10 mmol/mol or greater. Early in its deployment, however, the measurements were calibrated using only three injections of a single standard every six hours.

Additional calibrations were performed over a larger range of humidity values (0.2-20 mmol/mol) in February 2012. These were done with a manual syringe-pump system, which steadily pumps liquid standard into a stream of dry air. Unlike the PAL autosampler, the syringe pump provides a continuous flow of vapor to the instrument. Moreover, by altering the rates of both the liquid injection and the dry air, much lower mixing ratios can be achieved.

### **2.3. Summit, Greenland**

Two model L2120-i Picarro analyzers (designated Spiny and Gulper) were deployed at Summit, Greenland in summer 2011 through summer 2014. The instruments were housed in an enclosed rack in an underground laboratory. While the temperature of the laboratory was approximately 10° C for the duration of the experiment, the temperature of the enclosed rack was maintained at 15± 0.2° C.

Due to the need for the calibration system in Greenland to run autonomously for 11-month stretches, a custom dew point generator was developed to produce water vapor and calibrate both Summit instruments approximately every six hours. (Commercially available calibration systems were found unsuitable for this purpose.) In the custom system, dry air from an industrial regenerative drier (with a dew point temperature of -100° C) is supplied to a 10-L 51 Schott laboratory bottle containing liquid of known isotope ratio. Dry airflow bubbles through the liquid, producing vapor, whose isotope ratio ( $R_v = R_l/\alpha$ ) may be calculated as a function of the temperature-dependent fractionation factor  $\alpha$  and the isotope ratio of the liquid ( $R_l$ ). The temperature of the bubbler bottle was maintained near 20°C by applying heat to a copper sleeve enveloping the glass. (Effects of temperature deviations on the isotope ratio of the vapor produced are discussed later in this chapter.) The water vapor mixing ratio of the air stream delivered to the instruments was altered through dry air dilution; and a second-stage dilution was used to achieve the lowest mixing ratios. Since vapor and liquid within the bubbler bottle are always maintained at equilibrium, the removal of water with time will cause the isotopic composition of the remaining liquid reservoir to follow a theoretical Rayleigh distillation [Dansgaard, 1964].

Beginning in summer 2012, calibrations were performed every six hours. The mixing ratio of the air stream delivered to the instruments was maintained at approximately 4 mmol/mol and the air stream sampled for 15 minutes. Beginning in summer 2013, calibrations were performed at three different humidity levels by sampling air streams whose mixing ratios spanned 0.1-4 mmol/mol. While, at first, each of the three humidity levels was sampled for 20 minutes, beginning in September 2013, sampling at very low mixing ratios ( $<0.3$  mmol/mol) was extended to 40 minutes.

As with the Mauna Loa instrument, the concentration-dependences of Spiny and Gulper have been spot-checked at various times throughout their field deployment. This has been accomplished by slowly altering dry air dilution of the calibration system vapor stream to produce a large range of mixing ratios ( $\sim 0.1$ -8 mmol/mol) over several hours. Such extended concentration calibration periods have been performed both by increasing and by decreasing the vapor mixing ratio progressively. The isotopic deviation from the VSMOW-SLAP scale has also been checked using three standard waters and the syringe-pump system described in Section 2.2 of this chapter.

### **3. Concentration-dependence**

Characterizing the concentration-dependence is a key step in calibrating the isotopic measurements made by commercial laser analyzer. In this section, five isotopic standards are used to characterize the concentration-dependence of the Mauna Loa analyzer and evaluate its contribution to the total isotopic bias of the field observations. Then, using both the Mauna Loa and Summit instruments, uncertainties introduced through sampling hysteresis and curve-fitting

procedures are assessed. Finally, assumptions about the stability of the concentration-dependence with isotope ratio and with time are tested.

### **3.1. Characterization**

For the Mauna Loa analyzer, the concentration-dependence is the dominant factor controlling the variability of the total isotopic bias, which is shown for  $\delta^{18}\text{O}$  in Figure 3.1. The relationships between the isotopic bias and either time (i.e. drift) or the VSMOW-SLAP scale are in turn influenced by this strong humidity dependence. To characterize the unique concentration-dependence of this instrument, three curves are fit to the total isotopic bias as a function of the natural log of the vapor volume mixing ratio: a global quadratic polynomial [cf. *Rambo et al.*, 2011], a global cubic polynomial [cf. *Aemisegger et al.*, 2012; *Noone et al.*, 2013], and a local polynomial regression. A surface local polynomial regression, using both the natural log of the volume mixing ratio and the measured isotope ratio as predictors [cf. *Bailey et al.*, 2013], is also considered. (Note: typically, in correcting for the concentration-dependence, one would first normalize the total isotopic bias by isotope ratio and time in order to isolate the partial dependence on humidity, however, in order to compare the one- and two-dimensional functions herein described, no such normalization is performed prior to fitting.) To account for the small number of calibration points at low humidity, all four functions weight the data by  $1/q^2$ , where  $q$  is the volume mixing ratio in mmol/mol.

Subtracting these four functions from the observed isotopic bias produces the residual plots shown in Figure 3.2. Fitting residuals associated with the three one-dimensional functions (the three left-most panels) reveal that accounting for the concentration-dependence alone, even using a poor fit like the quadratic polynomial, reduces the range of the total isotopic bias in  $\delta^{18}\text{O}$

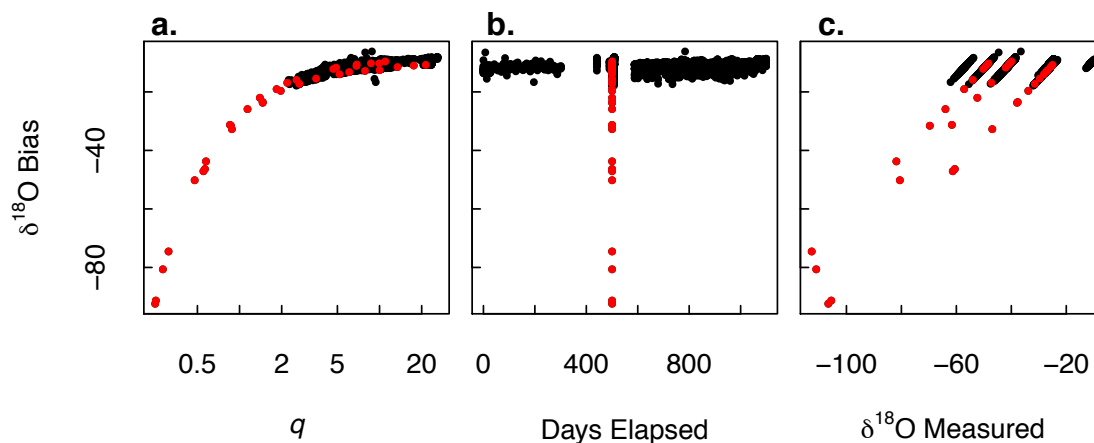


**Figure 3.1.** The total  $\delta^{18}\text{O}$  bias (permil) for the Mauna Loa analyzer as a function of a) the vapor volume mixing ratio in mmol/mol (shown on a log scale), b) time in days elapsed since October 1, 2010, and c) the raw isotope ratio measured in permil. Calibrations performed with the PAL autosampler are shown in black, while calibrations performed with the syringe pump are in red.

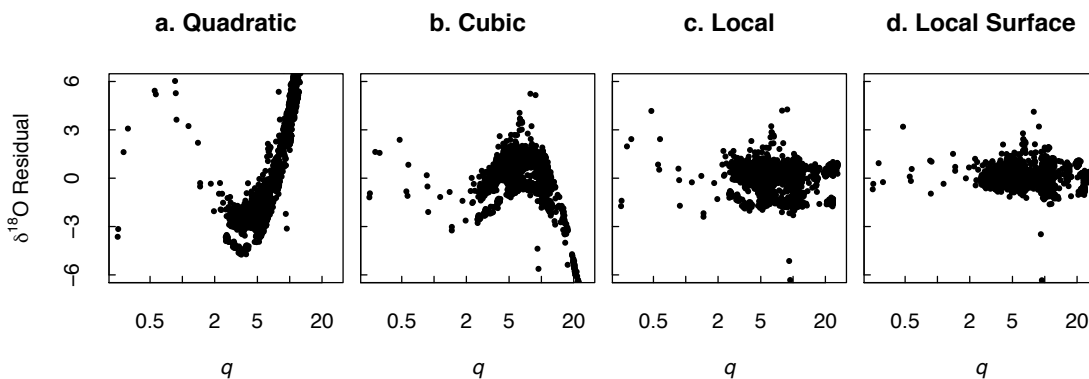


**Figure 3.2.** Fitting residuals (in permil) as a function of the volume mixing ratio in mmol/mol (shown on a log scale) for four different fitting procedures: (a) a global quadratic regression, (b) a global cubic regression, (c) a locally-weighted polynomial regression (degree = 2, smoothing parameter = 0.5), and (d) a locally weighted polynomial surface (degree = 2, smoothing parameter = 0.5) fit to both  $\ln(q)$  and the  $\delta^{18}\text{O}$  measured (permil).

by an order of magnitude. Of the three one-dimensional functions, the locally-weighted polynomial regression (with 2-degree polynomial and 0.5 spanning parameter) performs the best by lowering the root mean square error (RMSE: Quadratic = 7.41 permil, Cubic = 2.60 permil, Local Regression = 0.83 permil) and capturing the curvature of the bias at lower volume mixing ratios more accurately; however, it is worth noting that non-parametric fitting may not be appropriate in cases where few data points exist, since the degrees of freedom are reduced in order to perform the fitting locally.

The non-parametric surface (also with 2-degree polynomial and 0.5 spanning parameter) further reduces both the RMSE (0.57 permil) and the bias at low humidity, demonstrating the precision and accuracy gained by accounting simultaneously for the concentration-dependence and the isotopic deviation from the VSMOW-SLAP scale. Surface fitting may be particularly useful in cases where the concentration-dependence cannot be separated easily from other biases, as is the case at Mauna Loa. Though the autosampler is designed to reproduce higher volume mixing ratios (~20 mmol/mol) reliably, this experiment suggests it is unable to produce reliable lower mixing ratios (<10 mmol/mol). Consequently, it is not possible to normalize the isotope ratios of the standards injected to the same mixing ratio every calibration period. This is one additional challenge researchers may encounter when performing calibrations on isotopic analyzers in the field.

### ***3.2. Hysteresis***

To evaluate uncertainties in the concentration-dependence characterization introduced by sampling hysteresis, two subsets of the Mauna Loa calibration data are considered. The first subset is comprised of *filtered* autosampler injection points (which were also used to characterize

the Mauna Loa instrument's concentration-dependence in Section 3.1 of this chapter). Filtering is performed by eliminating the first two injections of each standard during every calibration period. (Eliminating the first three injections would have been preferable [cf. *Lis et al.*, 2008] but for the fact that during the first 500 days of the observational experiment each calibration period consisted of only three injections.) The second or *unfiltered* subset is comprised of all autosampler injections and therefore includes all possible memory effects for this calibration system.

Figure 3.3 shows the difference in the isotope ratio adjustment that would result if fitting the filtered data (solid lines) or the unfiltered data (dashed lines) with a quadratic polynomial (black), a cubic polynomial (blue), or a local polynomial regression (red). All curves are presented as a difference from the filtered local regression curve. Clearly, the choice of characterization function is much more important in determining the isotopic calibration for the

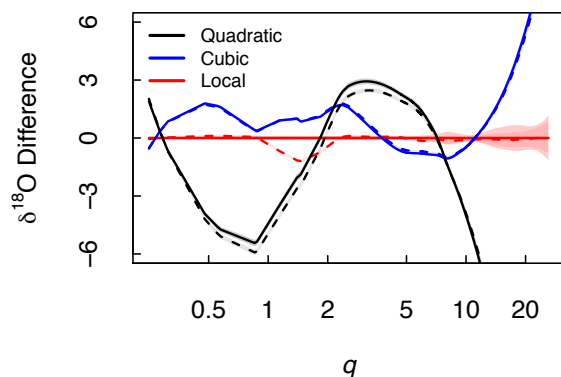


**Figure 3.3.** The  $\delta^{18}\text{O}$  difference (permil) for Mauna Loa between the various one-dimensional fitting procedures and the locally-weighted polynomial regression (Local=solid red line), as a function of  $q$  (mmol/mol, shown on a log scale). Curves fit to all data (unfiltered for hysteresis) are represented by dashed lines. Curves fit to filtered data are represented by solid lines. Standard errors are represented by shaded envelopes around each curve.

Mauna Loa instrument than any filtering of the autosampler data. While the maximum difference between the filtered and unfiltered data is about 1 permil, the differences between the cubic polynomial and local regression are several permil at both high and low humidity.

In contrast, at Summit, where the Spiny and Gulper analyzers are calibrated using a custom dew point generator, memory effects are much more critical in influencing the isotopic calibration. Figure 3.4, like Figure 3.3, shows differences in the isotopic adjustment that result from applying three one-dimensional functions: a global quadratic polynomial, a global cubic polynomial, and a local polynomial regression. All Summit isotopic values are normalized to the weekly mean isotope ratios measured in the humidity range 2.5-3.5 mmol/mol. (Shrinking this range or shifting it to higher mixing ratios does not change the qualitative features of the results). Because the Summit calibration data, in comparison with the Mauna Loa data, are more evenly distributed in time across the humidity range shown, no weighting is performed as part of the fitting.

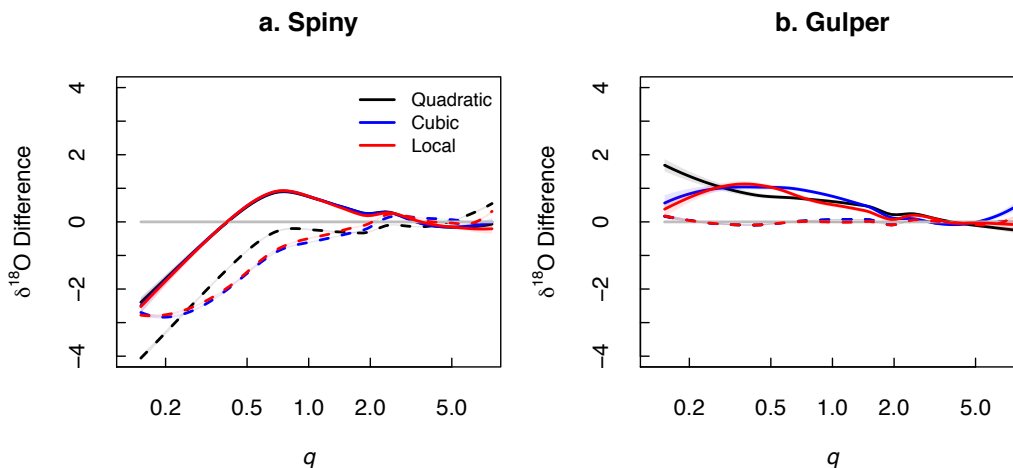


**Figure 3.4.** The difference in concentration-dependence for  $\delta^{18}\text{O}$  (permil) between concentration calibrations in which the vapor volume mixing ratio progressively increased (solid lines) or decreased (dashed lines) and the concentration-dependence obtained from all calibration data at Summit (solid gray line). Characterizations are shown as a function of  $q$  (mmol/mol, shown on a log scale) for various one-dimensional fitting procedures described in the legend. Standard errors are represented by shaded envelopes around each curve.

Hysteresis in the Summit system is evaluated by considering the different characterizations that result when isolating the extended concentration calibration periods in which the volume mixing ratio progressively increases (solid lines) or decreases (dashed lines). These are compared with the characterization obtained when all Summit concentration calibration data are used, including the six-hourly calibrations performed at three humidity levels. Unlike data from the extended concentration calibration periods, data from the six-hourly calibrations are already filtered in order to minimize memory effects. This is accomplished by discarding the first 9-19 minutes of isotopic data at each humidity level, with more data discarded at lower humidity.

Despite being very different in magnitude, the concentration-dependences of Spiny and Gulper are both sensitive to whether the humidity is progressively increased or decreased. Differences in the concentration-dependence characterization resulting from curve-fitting are, in contrast, negligible. This may be due to the fact that each curve in Figure 3.4 is comprised of at least 68 one-minute averages, and these data points are well distributed across the humidity range of interest. Differences between the solid and dashed lines, in comparison, suggest memory effects can be quite substantial in a bubbler-based calibration system. Indeed, the tubing connecting the glass calibration bottle to the instrument amplifies the surface area that the vaporized standard water contacts. As a result, equilibration may be slow. In the autosampler, in contrast, the syringe and the small cavities of the vaporizer and instrument may hold residual water molecules; however, dry air is flushed through the vaporizer and instrument following each injection. Thus the time to equilibration is reduced.

### ***3.3. Sensitivity to isotope ratio***

To verify that the concentration-dependence does not change with isotope ratio, data from the Mauna Loa syringe-pump calibrations, which were performed over the course of two days using three standard waters, are considered. Isotope ratios from each standard were normalized to the 10 mmol/mol humidity level prior to analysis. Figure 3.5 shows the difference in characterization that would be obtained from a single isotopic standard versus the characterization obtained from all the syringe-pump data. Differences are shown for two fitting procedures: a global cubic polynomial and a locally-weighted polynomial regression, whose degree and spanning parameter are chosen by generalized cross validation. While there is clear variability in the characterization curves obtained using the three standards, there is no evidence of a monotonic shift in concentration-dependence with isotope ratio. (Were a drift detected, frequent characterization of the concentration-dependence would be necessary to ensure internal consistency in the data.) Note that for any given vapor volume mixing ratio, at least two curves overlap within the standard error envelopes shown. Moreover, between 0.3 and 8 mmol/mol, the largest absolute difference between any individual curve and the curve obtained when using all the syringe-pump data is approximately 1.5 and 0.6 permil for the cubic and local regression functions, respectively. In contrast, the maximal difference between the two functions is clearly larger than 0.6 permil across this humidity range. This finding once again highlights the fact that great care is needed when fitting the concentration-dependence in order to improve the accuracy of the isotope ratio measurements. Variability in the concentration-dependence characterization is more likely to be caused by statistical fitting than by changes in the isotope ratio of the standard measured.

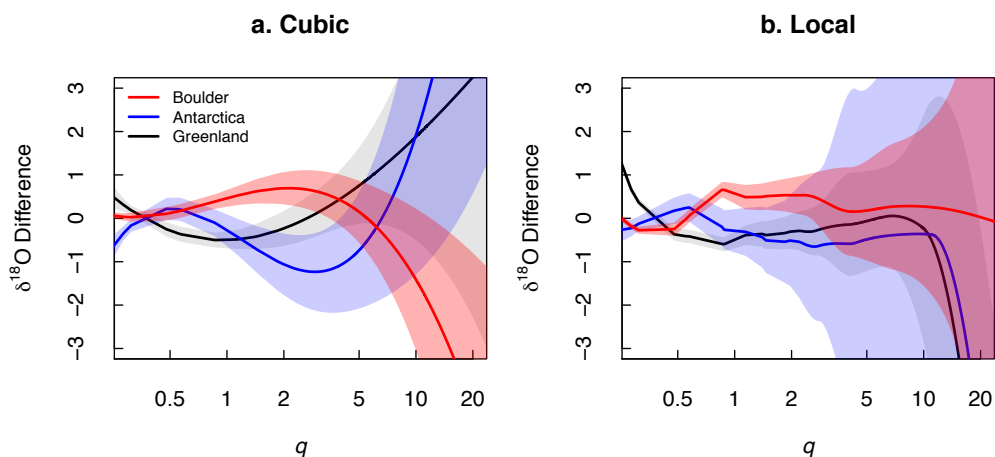


**Figure 3.5.** Concentration-dependence characterizations achieved with three different isotopic standards at Mauna Loa and fit with (a) a cubic polynomial or (b) a locally-weighted polynomial regression whose degree and spanning parameter are chosen by generalized cross validation. Curves are shown as differences (permil) from the concentration dependence obtained when data from all three standards are considered and are depicted as a function of  $q$  (mmol/mol, shown on a log scale). Standard errors are represented by shading.

### 3.4. Long-term stability

To identify possible changes in the concentration-dependence with time, the total isotopic bias in  $\delta^{18}\text{O}$  at Mauna Loa is evaluated as a function of the vapor volume mixing ratio for three-month periods, spanning October 2010 to September 2013. Only the autosampler calibrations are used for this purpose, and the isotope ratios measured are normalized, by standard, to the  $10 \pm 1$  mmol/mol humidity level. Figure 3.6 shows characterizations for three-month periods whose sample size exceeds 30. The concentration-dependence characterization for each period is displayed as a difference from the characterization obtained when all three years of data are considered. Characterizations are shown for both global cubic polynomials (left panel) and locally-weighted polynomial regressions, with degrees and spanning parameters chosen by generalized cross validation (right panel). Envelopes represent standard errors associated with

the fits and are larger near the humidity-range extremes, where fewer data points exist and instrument performance begins to degrade.

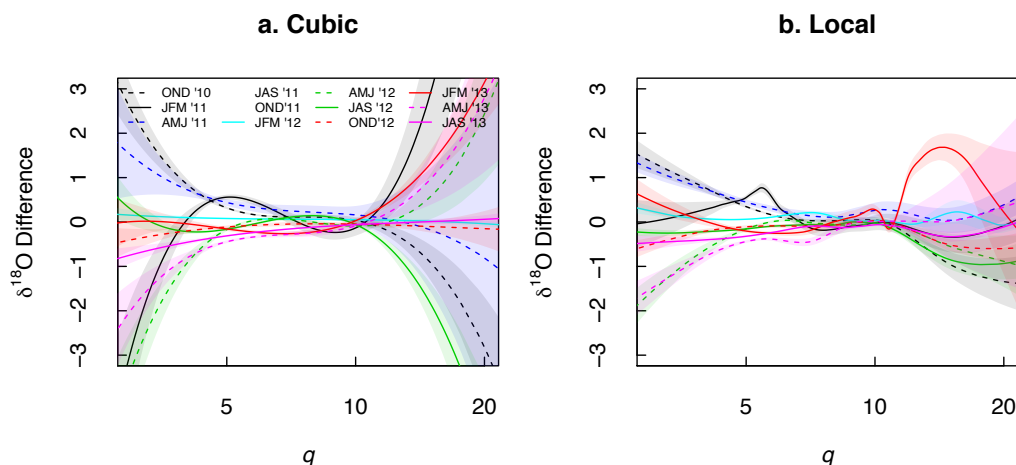


**Figure 3.6.** Concentration-dependence characterizations at Mauna Loa for three-month periods described in the legend. Characterizations are fit with (a) a cubic polynomial and (b) a locally-weighted polynomial regression whose degree and spanning parameter are chosen by generalized cross validation. Curves, which are shown for those periods with  $>30$  data points, are depicted as a difference (permil) from the concentration-dependence obtained when using all three years of data and are plotted as a function of  $q$  (mmol/mol, shown on a log scale). Standard errors are represented by shading.

Though differences between characterizations are apparent, there is no evidence of long-term drift. Instead, there is variability on the order of  $\pm 0.5$  permil over the humidity range approximately spanning 5-10 mmol/mol and greater variability outside this, where the data are sparse. The cubic fit exhibits much larger variability than the local regression near the humidity extremes, which again emphasizes the importance of statistical fitting in influencing the accuracy of the corrected isotope ratio data. When all three years of calibrations are considered, the standard error for both functions drops below 0.25 permil for the entire humidity range. These results suggest that while multiple calibrations may not be necessary for monitoring long-term

drift, they may nevertheless be useful for characterizing the concentration-dependence precisely, particularly at low humidity where the signal-to-noise ratio is very small.

The six-hourly calibration data at Summit, which span much lower volume mixing ratios, also show no trend in the concentration-dependence over a six-month period. Because of the design of the Summit calibration protocol (e.g. a large number of data at a small number of humidity levels), the data in a given month do not span a sufficient humidity range to characterize the concentration-dependence meaningfully. To address this challenge, we consider instead how well a single characterization—derived from all six months of one-minute-averaged data (where  $q > 0.15$  mmol/mol)—fits monthly mean clusters of calibration data. Figure 3.7 shows this “all data” characterization as a cubic polynomial (gray solid line) and as a local polynomial regression (gray dashed line) for both Spiny and Gulper. The colored crosses depict calibration data that are clustered by vapor volume mixing ratio and averaged in 30-day segments, approximately corresponding to the months shown in the legend. The width and height of the crosses show the one-sigma deviations of the clustered volume mixing ratios and isotope ratios, respectively. Figure 3.8 shows the same for  $\delta D$ . While there is clear variability within monthly means, especially at low humidity and more so for  $\delta D$  than  $\delta^{18}O$ , the “all data” curves pass within one standard deviation of nearly every cluster. Importantly, there are no instances in which more than one cluster per month lies farther than one standard deviation away from the “all data” curves. Thus, despite the fact that the Summit instruments exhibit substantially different biases, there is no clear evidence for long-term drift in the concentration-dependence of either Spiny or Gulper.

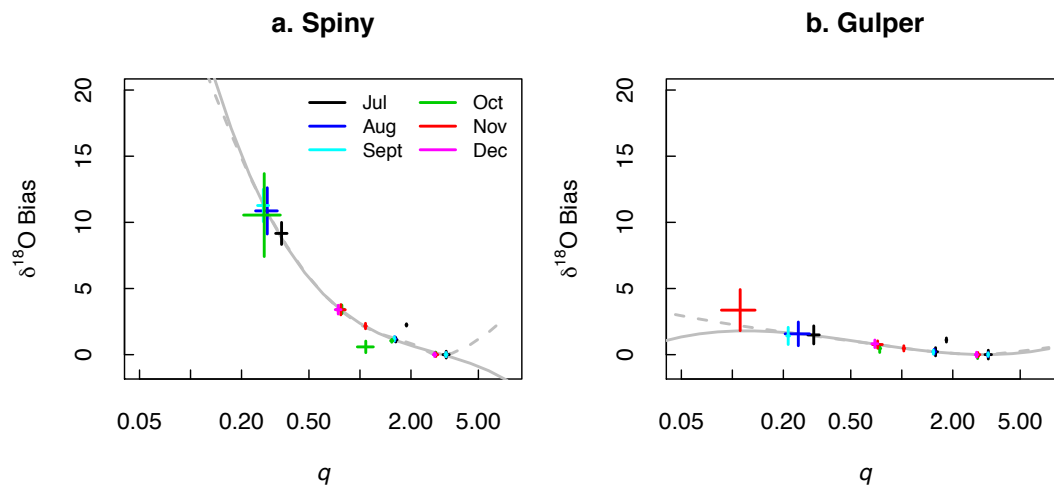


**Figure 3.7.** Monthly mean calibration points in  $\delta^{18}\text{O}$  (permil) for the Summit instruments shown as crosses whose width and height represent 1-sigma standard deviations in  $\delta^{18}\text{O}$  and  $q$  (mmol/mol). The gray lines, which represent the concentration-dependence characterizations obtained from a cubic polynomial (solid) and local polynomial regression (dashed) when all data are considered, are shown as a function of  $q$  (mmol/mol, shown on a log scale).

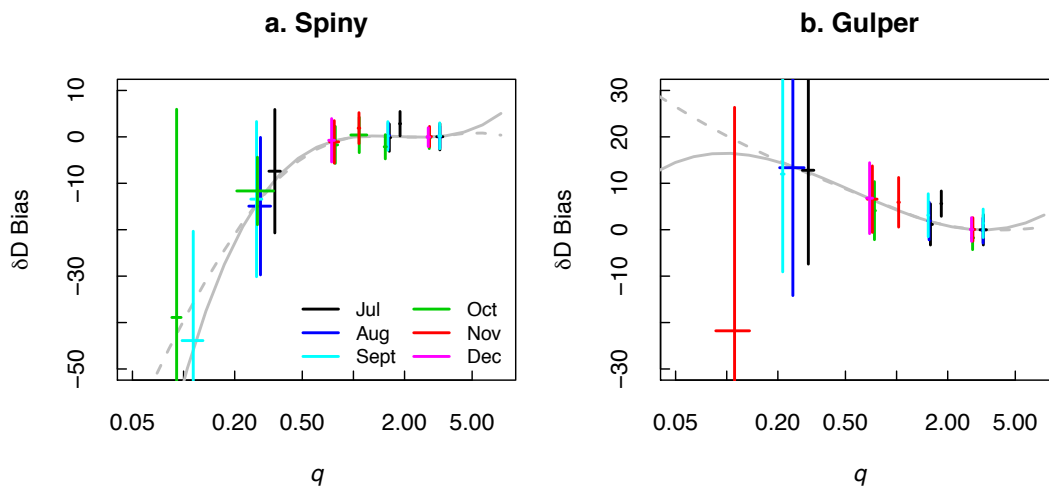


**Figure 3.8.** The same as Figure 3.7 but for  $\delta\text{D}$ .

#### 4. Isotopic drift

Once isotopic data are corrected for concentration-dependence, remaining biases indicate deviations from the VSMOW-SLAP scale. To evaluate the long-term stability of these deviations, drift in the five standards used in the Mauna Loa calibration routine is examined (Table 3.1). (The Boulder standard is ignored after February 2013, when it was replaced with new secondary standard water of different isotopic composition). Figure 3.9a shows the calibration points, corrected for concentration-dependence, with the observational mean removed for each standard. Fitting a simple linear regression to this normalized data reveals a small slope of less than 0.1 permil/year (significant at the 90% confidence level) with an error of 0.05 permil/year. To verify that this minimal and weakly significant slope is not the product of opposing slopes of larger magnitude associated with individual standards, Figure 3.9b compares the slopes of two standards, Greenland and Antarctic water, which together span the full experimental timeline. For neither standard is the slope different from zero. These results suggest long-term drift is negligible for the three-year Mauna Loa experiment and that deviation from the VSMOW-SLAP scale is stable.

**Table 3.1.** Short-term isotopic drift (permil/year) calculated for five distinct periods demarcated by dates on which the Mauna Loa standards were replaced.

Standard	Day of Experiment				
	1-279	280-499	500-859	860-1006	1007-1380
Vostok	1.74***	1.72*	0.56***	—	—
Greenland	1.59***	2.41**	-0.78***	—	—
Antarctica	—	—	-0.29***	2.54***	2.16***
Boulder	1.89***	1.91**	2.45***	—	—
Florida	—	—	0.86***	—	0.85

p-value legend \*\*\*<0.001 \*\*<0.01 \*<0.1

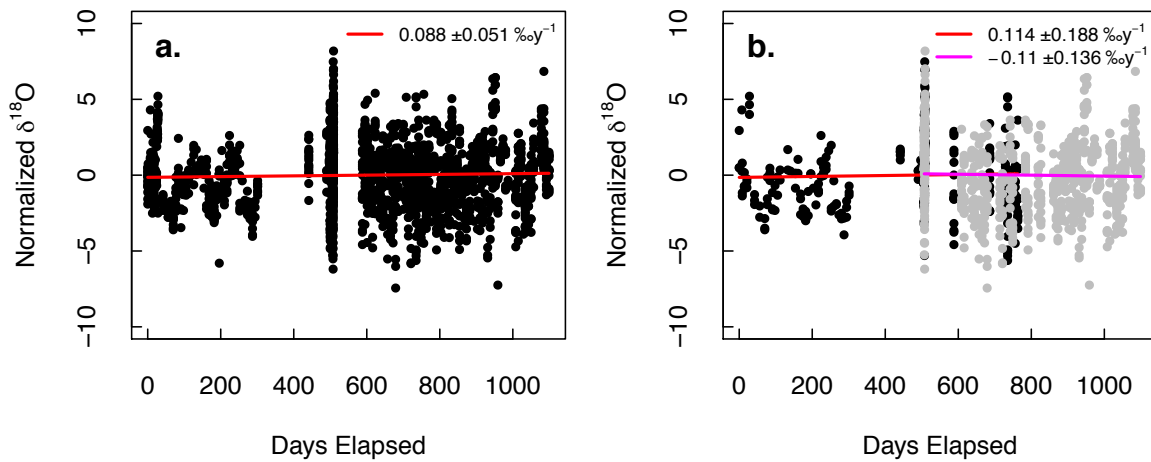


**Figure 3.9.** (a) Normalized and concentration-corrected calibration points ( $\delta^{18}\text{O}$ , permil) at Mauna Loa as a function of time. The red line—a simple linear regression—indicates isotopic drift. (b) Individual linear regressions fit to calibration points derived from two isotopic standards: Greenland melt water (black points, red line) and Antarctic melt water (gray points, magenta line).

However, upon closer inspection, drift on the order of  $-0.8$  to  $+2.5$  permil/year is evident during shorter periods that fall between dates on which the standards at Mauna Loa were replaced with new standard water (Table 3.1). To determine whether this shorter-term drift is caused by instrument imprecision or by changes in the standards themselves, calibration data are averaged for windows ranging from 20-60 days immediately following standard replacement dates. Table 3.2 shows the slopes of weighted linear regressions fit to these isotopic means. Only standards that span three standard-replacement dates are shown (so that the significance of their slopes may be discussed). While there is a tendency for greater enrichment the lower the isotope ratio, which would cause a flattening of the deviation from the VSMOW-SLAP scale with time, none of the individual slopes in Table 3.2 is significant, and all are within  $\pm 0.5$  permil/year, a much smaller range than found in Table 3.1. Furthermore, for the shortest averaging window, the slopes are all closer to zero. Though these findings do not exclude the possibility of drift in the

deviation from the VSMOW-SLAP scale, the insignificance of the slopes in Table 3.2 suggests long-term drift for any given isotope ratio is negligible so long as uncertainty of about 1 permil is acceptable (Figure 3.9a, RMSE = 0.839).

**Table 3.2.** Long-term isotopic drift (permil/year) evaluated by fitting a simple linear regression to isotopic averages calculated (for various averaging times) immediately following standard-replacement dates.

Standard	Averaging Time (Days)				
	20	30	40	50	60
Vostok	—	—	—	—	—
Greenland	0.18	0.38	0.38	0.44	0.45
Antarctica	-0.02	0.01	0.02	0.04	0.05
Boulder	-0.07	-0.15	-0.15	-0.15	-0.15
Florida	—	—	—	—	—

p-value legend \*\*\*<0.001 \*\*<0.01 \*<0.1

One possible explanation for isotopic variations between standard-replacement dates may be that the standards themselves drifted with time. Each week, the Mauna Loa instrument is calibrated by pipetting standard water—stored in a glass bottle—into small vials, which are loaded onto the autosampler. Over time, weekly opening and closing of the standards allows isotopic exchange between the water reservoir and the ambient vapor, which could have caused the drift shown in Table 3.1. Though this unfortunately impedes characterization of shorter-term instrumental drift, it importantly showcases the susceptibility of standards to drift in the field. Long-term campaigns wishing to characterize shorter-term drift will need to replace standards sent to the field every few weeks or use an onsite, airtight storage system for standards such as that described by *Tanweer et al.* [2009].

At Summit, in comparison, after correcting for concentration, the six-hourly calibrations show a clear enrichment in  $\delta^{18}\text{O}$  at an approximate rate of 1.4 permil/year (Figure 3.10a). This

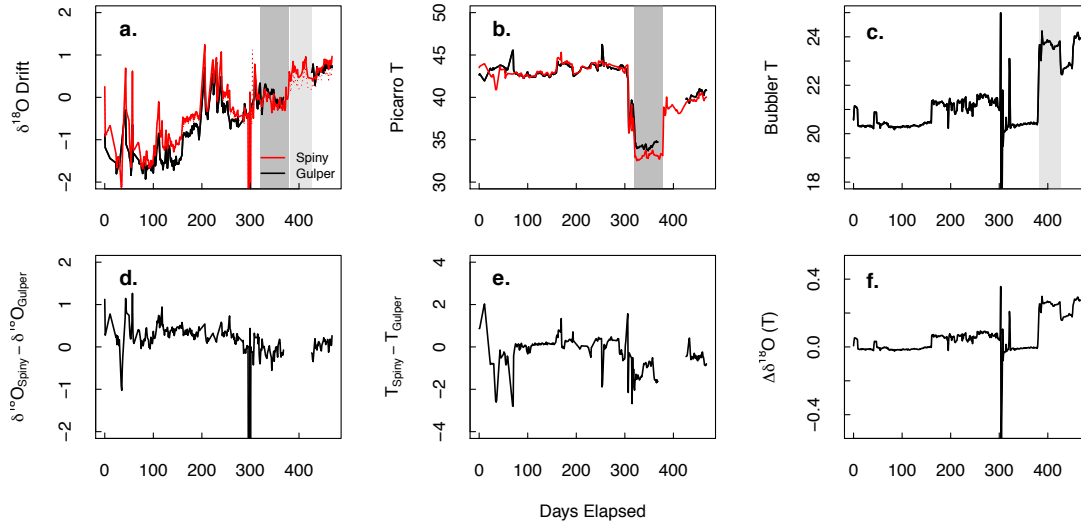


**Figure 3.10.** (a) The isotopic drift in  $\delta^{18}\text{O}$  (permil) of the two Summit instruments and (b) the difference in isotopic drift (permil) between the two. (c) Ambient temperature changes ( $^{\circ}\text{C}$ ) detected by the two instruments and (d) the temperature change difference ( $^{\circ}\text{C}$ ) between the two. (e) Temperature changes ( $^{\circ}\text{C}$ ) in the glass bubbler bottle used to calibrate the Summit instruments. (f) Changes in  $\delta^{18}\text{O}$  (permil) predicted as a result of bubbler temperature changes.

drift is nearly identical between Spiny and Gulper but for a few exceptional calibration points (Figure 3.10b), which suggests a source external to the instruments. Indeed, as water is continuously vaporized and removed from the bubbler bottle of the Summit calibration system, the isotopic composition of the remaining liquid reservoir should become more enriched, following a predictable distillation described by *Wang et al.* [2009]:

$$R_v(t) = \frac{R_{l0}}{\alpha} \cdot \left(1 - \frac{t}{\tau}\right)^{\frac{1}{\alpha}-1} \quad (3.1)$$

Here,  $R_v$  is the isotope ratio of the vapor produced,  $R_{l0}$  is the initial isotope ratio of the liquid

water,  $\tau$  is the time necessary to evaporate all liquid from the bottle,  $t$  is the time elapsed, and  $\alpha$  is the temperature-dependent equilibrium fractionation factor. Moreover, as a result of fractionation differences,  $\delta^{18}\text{O}$  should increase faster than  $\delta\text{D}$ , resulting in a decrease in the deuterium excess ( $d = \delta\text{D} - 8 \times \delta^{18}\text{O}$ ) as the liquid reservoir undergoes evaporation [Craig, 1961; Sharp, 2007].

Since  $\tau$  is unknown, a range of possible values is considered by estimating the drift in  $\delta^{18}\text{O}$  and  $d$  from the distillation model for the period following July 2013, when the glass bottle of the calibration system was refilled. These estimates are then compared with the slopes of isotopic change observed (for such a short period the observed drift is well-described by linear models).  $\tau$ 's spanning 1500-1800 days (or approximately 4-5 years) produce the smallest differences in slope between model and observations (e.g.  $< 0.04$  permil/year in  $\delta^{18}\text{O}$ ). Figure 3.11 shows the modeled curves associated with these  $\tau$ 's, normalized and plotted for the last 150 days of the experiment. This range of  $\tau$ 's is then used to extrapolate the distillation that would have occurred 421-727 days into the experiment, which should approximate the first year of calibration points plotted (days 0-306 in Figures 3.10-3.11). (Although the custom dew point generator was set up in summer 2011, the first six-hourly instrumental calibrations were not made until the following year, hence the discrepancy in dating). Normalizing and plotting these extrapolated curves (Figure 3.11) suggests the 1800-day distillation model best explains the drift in both isotope ratios and in deuterium excess.

Assuming the linear enrichment in  $\delta^{18}\text{O}$  in Spiny and Gulper is entirely explained by distillation of the calibration system, uncertainty due to imprecision can be estimated once the linear trend is removed. For the period following July 2013 the residual standard error is 0.21 permil. For the period before July 2013 the residual standard error is 0.72 permil.

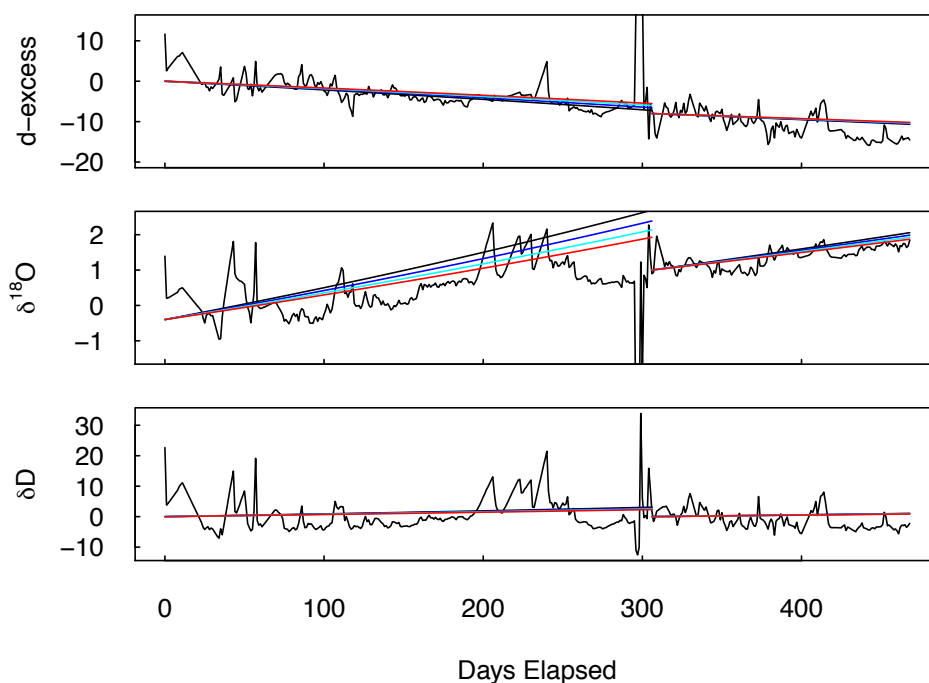


**Figure 3.11.** Normalized deuterium excess (top),  $\delta^{18}\text{O}$  (middle), and  $\delta\text{D}$  (bottom) for Spiny at Summit (permil) shown as a function of time. Colored lines represent distillation models where  $\tau$ , the total time required to remove all liquid from the bubbler bottle, equals 1500 (black), 1600 (blue), 1700 (cyan), or 1800 (red) days. All data, including the modeled data, are normalized.

Though previous studies have speculated that ambient temperature changes cause instrumental accuracy to change with time [cf. *Sturm and Knohl, 2010; Rambo et al., 2011*], the data presented here do not support this claim. During the summer of 2013 (represented by dark gray shading in Figure 3.10), the temperatures of the Summit analyzers plummeted following a change in the temperature of the underground chamber in which they were housed (Figure 3.10c-d). No concurrent change in either isotope ratio occurred, providing evidence that ambient temperature is not a strong control on instrumental drift.

In comparison, changes in the temperature of the bubbler bottle do appear to influence the isotopic calibrations. During the fall of 2013 (the period represented by light gray shading in Figure 3.10), the bubbler temperature increased from 20°C to 24°C (Figure 3.10e). A change of

this magnitude should have altered the rates at which heavy and normal water isotopes change phase relative to one another, resulting in an increase in  $\delta^{18}\text{O}$  of about a 0.25 permil (Figure 3.10f). Such enrichment is evident in the Spiny drift curve of Figure 3.10a. Moreover, the dramatic change in bubbler temperature near day 300 coincides with a sharp drop in  $\delta^{18}\text{O}$  in Spiny, causing large differences between the two instruments. Thus, changes in bubbler temperature of several degrees Celsius or more can have discernible effects on the isotopic accuracy of laser-based measurement systems.

## 5. Implications for field calibrations

There are a number of different factors that need to be considered in calibrating isotope ratio data, and, as described in the introduction of this chapter, many of these factors have been documented previously [e.g. *Sturm and Knohl*, 2010; *Johnson et al.*, 2011; *Tremoy et al.*, 2011; *Aemisegger et al.*, 2012; *Gröning*, 2011; *Noone et al.*, 2013; *Steen-Larsen et al.*, 2013]. However, only recently are data sets sufficiently long to evaluate the long-term stability of laser isotopic analyzers in the field. This analysis has evaluated the stability of the isotopic biases—beginning with the concentration-dependence, or the change in isotope ratio with vapor volume mixing ratio—in three field-operational vapor isotopic analyzers, which use cavity ring-down spectroscopy. The instruments, which are deployed at the Mauna Loa Observatory on Hawaii and at Summit, Greenland, include both the early model L115-i Picarro and the later L2120-i, which have been used in previous studies to study atmospheric hydrological phenomena [e.g. *Galewsky et al.*, 2011; *Noone et al.*, 2011; *Hurley et al.*, 2012; *Bailey et al.*, 2013] and water exchange between the land surface and atmosphere [e.g. *Berkelhammer et al.*, 2013; *Noone et*

*al.*, 2013; *Aemisegger et al.*, 2014]. While early models tend to exhibit larger concentration-dependences, factory pre-calibration has helped reduce such biases in the later 2000 series [cf. *Aemisegger et al.*, 2012].

The results of this work suggest that while these types of laser analyzers exhibit some variability in the concentration-dependence with time, there is no long-term drift. Thus, while repeated calibrations can reduce uncertainties associated with fitting the data statistically, they are not necessary to track long-term changes in the instrumental optics, at least not at relatively clean baseline stations like Mauna Loa and Summit. Still, there is always the possibility that instrumental biases may drift as the optics dirty, particularly at sites exposed to heavy concentrations of pollutants.

In addition, there is no clear evidence of sensitivity in the concentration-dependence to the isotope ratio of the standard used. Therefore, for field campaigns in which it is desirable to reduce calibration time and maximize ambient sampling, calibrations for the concentration-dependence should prioritize making single measurements across a wide range of humidity levels rather than repeating measurements at a single humidity level or using multiple standards. Maximizing the spread of the calibration points is particularly important for reducing uncertainties associated with statistically fitting the concentration-dependence curve.

How important statistical-fitting is for the overall accuracy of the isotopic measurements depends, at least in part, on the calibration system used. The Mauna Loa experiment showed that differences in the bias correction derived from fitting different functions to the autosampler data were much larger than any differences produced by filtering for memory effects. However, at Summit, where a bubbler-based dew point generator was used, the opposite was true. This result is likely influenced by two factors: 1) a reduced sensitivity to statistical-fitting associated with

the larger number of calibration points at Summit and 2) greater hysteresis associated with the bubbler system design, which, unlike the autosampler, does not flush the instrument with dry air between calibration points.

Both the Mauna Loa and Summit experiments suggest that, once the concentration-dependence is measured, a single global characterization may be used to correct all ambient data. Remaining isotopic biases represent deviations from the VSMOW-SLAP scale, and these may be corrected either simultaneously with the concentration-dependence or sequentially by fitting a simple linear regression between the known values of three or more standards and the (concentration-corrected) isotope ratios observed. Unfortunately, neither experiment presented here could determine conclusively whether this deviation changes with time. At Mauna Loa, while calibration data clearly drifted between the dates on which the standard waters were replaced—suggesting the standards themselves drifted—changes in the isotope ratios from one replacement date to the next were not significant. There was, however, a tendency toward greater enrichment the more depleted the standard. Over time, this would result in a change in the slope of the deviation from the VSMOW-SLAP scale, even if the drift associated with any particular isotope ratio were not significant. In comparison, at Summit, though the possibility of instrumental drift could not be ruled out, changes in the individual isotope ratios and deuterium excess of the calibration points were consistent with distillation of water in the bubbler bottle with time.

For future field experiments using laser-based isotopic analyzers, eliminating or accurately modeling drift in the standards used to calibrate the instruments will thus be paramount. Modeling distillation in a bubbler system, for example, will require knowing the exact time to remove all water from the liquid reservoir. This, in turn, depends on the initial

volume (or mass) of water and the flow rate of dry air through the bubbler. In contrast, for calibrations with an autosampler, large amounts of secondary standards should either be stored onsite in an airtight container, such as described by *Tanweer et al.* [2009], or shipped to the site every 2-3 weeks to avoid excessive fractionation associated with opening standard bottles in the field. Such precautions will make it possible to evaluate more accurately whether instrumental drift exists for laser-based isotopic analyzers or whether changes in deviations from the VSMOW-SLAP scale are significant with time.

Advancements in commercial technology over the last few years suggest that the accuracy and precision of laser isotopic analyzers will continue to improve. Nevertheless, the biases examined in this chapter remain critical to evaluate, particularly since they are unique to each instrument. To that end, the following recommendations are offered for long-term deployments.

The ideal *calibration system* should:

1. Enable very accurate evaluation of the concentration-dependence. This can only be achieved by producing very low and stable volume mixing ratios of water vapor for extended periods of time. This study found that a custom dew point generator could achieve volume mixing ratios  $< 0.3$  mmol/mol, but that a vapor stream of at least 30 minutes was necessary to obtain a stable 10-minute average and minimize hysteresis. The autosampler, in contrast, was unable to produce low volume mixing ratios reliably.
2. Exhibit minimal or carefully controlled drift. While the former can be achieved by storing standards in specially designed airtight containers [*Tanweer et al.*, 2009],

the latter requires both that the liquid reservoir be temperature-controlled and that distillation of the liquid be carefully modeled and spot-checked.

3. Allow multiple standards to be delivered to the instrument. At least three standards are recommended for sequential-calibration approaches, in which deviations from the VSMOW-SLAP scale are corrected after the concentration-dependence is accounted for. More standards will be necessary to reduce prediction errors associated with correcting the biases simultaneously, such as with a local polynomial regression surface. While an autosampler can easily accommodate any number of standards, a custom dew point generator would require a different bubbler bottle for each standard.

The ideal *calibration approach* should:

1. Characterize the concentration-dependence by sampling a single isotopic standard at a large number of humidity levels. Sampling at low humidity (e.g. <1 mmol/mol) should be repeated in order to bolster the signal-to-noise ratio. While frequently repeated characterizations of the concentration-dependence are not necessary for verifying the stability of this bias, field programs may nevertheless wish to recheck their characterizations every few months, particularly if operating in polluted environments.
2. Choose a statistical-fitting procedure that minimizes the magnitude of fitting biases introduced into the data.
3. Consider whether simultaneously correcting the concentration-dependence and deviation from the VSMOW-SLAP scale improves data accuracy.

## CHAPTER IV

### Characterizing precipitation efficiency and distinguishing dynamical and microphysical controls on atmospheric constituents using isotope ratios in water vapor

#### 1. Introduction

Shallow convection plays a critical role in climate by regulating the exchange of moisture between the boundary layer and free troposphere. While convective mixing results in a net upward transport of moisture, precipitation works to dry the atmosphere by removing condensate and returning liquid water to the surface [Sherwood *et al.*, 2010]. The efficiency with which a convective cloud system produces precipitation (i.e. the precipitation efficiency, or  $e$ ) thus determines the proportion of water detrained above the boundary layer through cloud evaporation. Not all studies agree, however, as to how the precipitation efficiency affects low-level cloudiness. Sherwood *et al.* [2014], for example, hypothesized that as convective mixing in the lower troposphere increases, the bulk precipitation efficiency is reduced, moistening the free troposphere at the expense of the boundary layer. Drying of the boundary layer subsequently reduces low-level cloud and enhances climate warming. Zhao [2014], in contrast, claimed that climate models with lower precipitation efficiency maintain higher liquid water paths and thus exhibit greater low-cloud cover, which reduces warming through albedo effects. To help resolve these divergent hypotheses, observational assessments of precipitation efficiency and cloud fields are needed.

In addition to modifying moisture exchange in the vertical, precipitation processes influence climate by regulating vertical distributions of aerosol. Indeed, precipitation is the principal mechanism by which aerosol are cleansed from the atmosphere [Ramanathan *et al.*,

2001]; and recent work suggests rain removal is more important than proximity to an emission source in determining particle number concentrations near marine low-cloud [Wood *et al.*, 2012]. Some particle scavenging may, however, be offset by new particle formation. Indeed, by removing pre-existing particles and reducing the vapor condensation sink for aerosol-forming gases like SO<sub>2</sub>, precipitation may facilitate particle nucleation [Nilsson *et al.*, 2001]. As a result, recently formed particles are often observed in the vicinity of precipitating convective systems [Clarke, 1993]. In contrast, cloud-processing in the absence of precipitation can enhance particle number concentrations above the boundary layer [Ridley *et al.*, 1997] and shift particles toward larger diameters [Hoppel *et al.*, 1986]. Since both concentration and size influence aerosol optical properties [Yu *et al.*, 2006], and since aerosols also affect the albedo [Twomey, 1977] and lifetime [Albrecht, 1989] of clouds, interactions between aerosols, clouds, and precipitation have important implications for climate.

Unfortunately, using observations to quantify precipitation efficiency is no small task. To estimate precipitation efficiency using satellite retrievals of rainfall and cloud liquid water content, for instance, Lau and Wu [2003] required a weather and climate model parameterization, which assumes that the autoconversion of cloud drops to raindrops depends on a critical value of cloud water content. Other observational estimates of precipitation efficiency require knowledge of large-scale hydrological fields, such as water vapor convergence and surface evaporation [Sui *et al.*, 2005; Sui *et al.*, 2007], which cannot be measured directly. To evaluate the relationships among convective mixing, precipitation, aerosols, and cloudiness, a much simpler method for estimating precipitation efficiency is desirable.

Isotope ratios in water vapor provide a unique way to characterize the precipitation efficiency of convection [Bailey *et al.*, 2013], since heavy isotopes—with their lower saturation

vapor pressures—preferentially and predictably condense and rain out [Dansgaard, 1964]. Consequently, under conditions in which all condensate is immediately converted to precipitation, the depletion of heavy isotopes can be described using a simple Rayleigh distillation model:

$$R_i = R_0 f^{\alpha-1}, \quad (4.1)$$

where  $R$  is the heavy-to-light isotope ratio of an ascending moist adiabatic parcel, 0 denotes a reference level,  $f$  is the fraction of water remaining, and  $\alpha$  is a temperature-dependent fractionation factor. If, in contrast, some condensate remains with the ascending plume (i.e. the precipitation efficiency  $0 \leq e < 1$ ), isotopic depletion of the air mass will not be as great as Equation 4.1 predicts and will instead follow a modified distillation model [Dansgaard, 1964; Jouzel and Merlivat, 1984; Noone, 2012]:

$$R_i = R_{i-1} \left( \frac{q_i + \alpha(1-e)(q_0 - q_i)}{q_{i-1} + \alpha(1-e)(q_0 - q_{i-1})} \right)^{\frac{\alpha e}{1-\alpha(1-e)}-1}, \quad (4.2)$$

where  $q$  represents the vapor volume mixing ratio. By fitting this modified model to vertical profiles of  $q$  and the heavy-to-light oxygen isotope ratio ( $^{18}\text{O}/^{16}\text{O}$ ), Bailey *et al.* [2013] identified diurnal changes in the precipitation efficiency of convection on the Big Island of Hawaii.

This study seeks to identify the synoptic controls on the precipitation efficiency of strong convective events near Hawaii and to determine the influence of dynamical and microphysical (precipitation) processes on vertical distributions of atmospheric constituents important for

climate. We begin by evaluating the ability of Eulerian measurements of isotope ratios in water vapor to characterize the precipitation efficiency of strong convection using three years of spectroscopic measurements from the Mauna Loa Observatory (MLO). We then evaluate the large-scale dynamics associated with high and low precipitation efficiency events. By linking our findings with large-scale fields well resolved by climate models, we reveal how the bulk precipitation efficiency of the subtropics may change with climate. Finally, we model the strength of convective mixing associated with different precipitation efficiency events in order to distinguish dynamical and microphysical controls on vertical distributions of moisture, trace gases, and particle pollutants. The results suggest that while variations in synoptic circulation clearly influence the trace gas concentrations observed, convective mixing and microphysical processes—which also vary by precipitation efficiency—are found to be more important in regulating particle scavenging and growth.

## **2. Methods**

### ***2.1. Location***

Mauna Loa Observatory (MLO), located at 3400 m on the Big Island of Hawaii has served as a baseline observatory since the 1950s, measuring key climate-altering constituents including numerous greenhouse gases. With its remote Pacific setting and high-altitude location, the Observatory is often exposed to the free troposphere at night and boundary-layer influenced air masses during the day, making it an ideal location for studying convective activity from a fixed location. Moreover, the long history of meteorological, trace gas, and particle

measurements at MLO provides a rich data context in which to evaluate the new isotopic measurements used in this analysis.

## **2.2. Water vapor volume mixing ratio and isotope ratios**

Since the fall of 2010, a Picarro vapor isotopic analyzer (model L1115-i) has measured vapor volume mixing ratios and isotope ratios at MLO. The analyzer samples from a hooded stack on the Charles Keeling building through 0.25-inch stainless steel tubing maintained at room temperature, which exceeds the ambient dew point. Consequently, the instrument essentially measures the total water mixing ratio; however, this chapter follows the tradition of previous studies in referring to the observations as vapor volume mixing ratios ( $q$ ) [cf. *Noone et al.*, 2011, *Bailey et al.*, 2013]. Isotopic calibrations, which are described in detail in Chapter 3, are performed weekly using a LEAP Technologies PAL (Prep and Load) autosampler. For each injection sequence of a liquid standard, the first two injections are eliminated in order to minimize memory effects. Additional characterizations of the analyzer's "concentration dependence" [cf. *Lis et al.*, 2008; *Sturm and Knohl*, 2010; *Johnson et al.*, 2011; *Rambo et al.*, 2011; *Tremoy et al.*, 2011; *Aemisegger et al.*, 2012; *Wen et al.*, 2012; *Bailey et al.*, 2013; *Steen-Larsen et al.*, 2013]—which describes changes in isotope ratio caused solely by changes in the vapor volume mixing ratio—have been obtained with a syringe-pump system. The  $q$  measurements are not calibrated, since they are within 0.33 mmol/mol of the volume mixing ratios estimated from regular MLO meteorological observations.

Three years of the MLO isotopic record, spanning October 2010 – September 2013, were selected. Data were first converted to 15-minute, mass-weighted averages before calibration corrections were applied. Using both the autosampler and syringe-pump calibration points,

isotope ratio observations were simultaneously corrected for their concentration dependence and for deviations from the VSMOW (Vienna Standard Mean Ocean Water) – SLAP (Standard Light Antarctic Precipitation) scale. This one-step correction was accomplished using a locally-weighted two-degree polynomial regression (with a spanning parameter of 0.5) [cf. *Bailey et al.*, 2013]. However, because statistical fitting choices can significantly affect the accuracy of bias corrections (see Chapter 3), a series of sensitivity tests was performed prior to choosing this particular approach. As described in Appendix A, uncertainties based on calibration choices reduce confidence in the selection of high and low precipitation efficiency events to 90%; nevertheless, the conclusions of this analysis are robust and insensitive to any of the statistical-fitting choices considered.

A peak  $q$  value ( $q_{peak}$ ) was calculated for each day by identifying the top 10% of  $q$  values observed between 1200 HST and 1800 HST and taking the mean for measurements whose  $\delta^{18}\text{O}$  values also exceeded the 90<sup>th</sup> percentile. Similarly, a peak  $\delta^{18}\text{O}$  value ( $\delta^{18}\text{O}_{peak}$ ) was calculated for each day by identifying the top 10% of  $\delta^{18}\text{O}$  values observed between 1200 HST and 1800 HST and taking the mean for measurements whose  $q$  values also exceeded the 90<sup>th</sup> percentile. Nighttime  $q$  and  $\delta^{18}\text{O}$  values ( $q_{night}$ ,  $\delta^{18}\text{O}_{night}$ ) were calculated by averaging observations taken between midnight and 0600 HST.

### **2.3. Aerosols, ozone, and methane**

To evaluate dynamical and microphysical controls on vertical distributions of atmospheric constituents, mean values of particle number concentration, total light scattering coefficient ( $\sigma_{sp}$ ), the backwards-hemispheric light scattering coefficient ( $\sigma_{bsp}$ ), ozone concentration, and methane concentration were calculated for each hour of the diurnal cycle from

NOAA-Earth System Research Laboratory data collected as part of routine long-term monitoring efforts. Particle number concentrations are measured at MLO with a TSI 3760 particle counter. One-minute averages of these data [P. Sheridan, *personal communication*, 2014] were converted to STP by assuming an instrument temperature of 12°C and a pressure of 680 hPa (resulting in a uniform scale factor of 1.555), and 15-minute-averages were created that aligned temporally with the isotopic data. Scattering coefficient and backscattering coefficient are measured at three wavelengths (450 nm, 550 nm, and 700 nm) with a nephelometer (TSI 3563). This study utilizes one-minute averages of these data [P. Sheridan, *personal communication*, 2014]—averaged again to 15-minutes—and reports scattering and backscattering coefficients measured at the 550 nm wavelength. Only those nephelometer measurements made with the normal 10 μm cut size and corrections for both STP and truncation applied are used. Hourly methane data—measured by gas chromatography—are available by anonymous ftp to [ftp://ftp.cmdl.noaa.gov/data/trace\\_gases/ch4/in-situ/surface/mlo/](ftp://ftp.cmdl.noaa.gov/data/trace_gases/ch4/in-situ/surface/mlo/) [Dlugokencky *et al.*, 2014]; and five-minute surface ozone data—measured by ultraviolet absorption photometer—are available by anonymous ftp to <ftp://ftp.cmdl.noaa.gov/ozwv/SurfaceOzone/MLO/> [McClure-Begley *et al.*, 2014].

#### **2.4. Reanalysis**

To study the large-scale conditions under which different convective events arise, composites of horizontal and vertical winds, geopotential height, and total column water were created using the  $0.75^\circ \times 0.75^\circ$  ECMWF Reanalysis ERA-Interim. The analysis was repeated using the  $2.5^\circ \times 2.5^\circ$  NCEP-NCAR Reanalysis—which is used to generate the back trajectories derived through NOAA’s HYSPLIT (Hybrid Single Particle Lagrangian Integrated Trajectory)

Model (<http://ready.arl.noaa.gov/HYSPLIT.php>)—and the results presented here are insensitive to the choice of reanalysis data. The three-dimensional back trajectories were calculated using vertical velocity reported from the NCEP-NCAR Reanalysis.

## ***2.5. Precipitation efficiency***

Previous studies suggest the precipitation efficiency, or the ratio of the rates at which precipitation and condensation form, may be calculated in one of several ways. For example, while the ratio of the surface rain rate to the sum of vapor convergence and evaporation rates defines a bulk precipitation efficiency, it is typically the ratio of the surface rain rate to the sum of vapor condensation and deposition rates that defines the precipitation efficiency in cloud-modeling studies [*Sui et al.*, 2007]. Yet depending on how these large-scale and microphysical efficiencies are estimated, they need not necessarily agree [*Sui et al.*, 2005].

Isotope ratios in water vapor offer an independent estimate of precipitation efficiency that follows the trajectory of an air mass. Since a Rayleigh model (Equation 4.1) assumes that all condensate is immediately removed as precipitation, isotopic observations following such a distillation indicate maximal precipitation efficiency ( $e=1$ ) [*Bailey et al.*, 2013]. If, on the other hand, some condensate remains with the ascending moist adiabatic plume, the isotope ratios will be less depleted than the Rayleigh model predicts. And, in the extreme case that no precipitation occurs ( $e=0$ ), both the isotope ratio and total water mixing ratio of the ascending parcel will be conserved, at least until the cloudy air mass mixes with a drier one. One might thus expect that low-precipitation efficiency convective events at MLO would resemble a mixing process in which water vapor and cloud condensate are exchanged between the saturated boundary layer and the dry subtropical free troposphere. The same mixing line might, of course, also describe

the exchange of moisture between two unsaturated air masses in the vertical, however differentiating amongst these cases is not critical for the purposes of this study given that ventilation of moisture from the boundary layer to the free troposphere would occur regardless.

Based on their resemblance to either Rayleigh or mixing processes, strong convective events near Hawaii are thus classified as having high or low precipitation efficiency, respectively. The validity of these definitions will be tested as part of the analysis. The resemblance to Rayleigh or mixing processes is determined by identifying anomalies in the peak daytime isotope ratio after its dependence on  $q_{peak}$  has been removed. This is accomplished by regressing the calibrated  $\delta^{18}\text{O}_{peak}$  values on  $1/q_{peak}$  using a simple linear regression (since the relationship between  $\delta^{18}\text{O}$  and  $q$  is approximately log-linear). Once the predicted  $q$ -dependence is subtracted from the  $\delta^{18}\text{O}_{peak}$  values, anomalies are categorized by percentile. Convective events whose isotopic anomalies fall below the 25<sup>th</sup> percentile are considered more Rayleigh-like, and thus higher in precipitation efficiency; and convective events whose anomalies exceed the 75<sup>th</sup> percentile are considered more mixing-like, and thus lower in precipitation efficiency. Bivariate distributions of these populations in  $\delta^{18}\text{O}$ - $q$  space are presented in Section 3 of this chapter.

## **2.6. *Mixing model***

A column model with five variable parameters is constructed to 1) capture the mixing process associated with convective transport and to 2) distinguish dynamical from microphysical controls on atmospheric constituents. Mixing is expressed as non-local entrainment into a transition layer, which *Bailey et al.* [2013] found regularly developed between the boundary layer and free troposphere near Hawaii. The model assumes that early in the day, mixing is

dominated by turbulent eddies, which carry boundary-layer constituents upward. Later in the day, as downslope winds replace upslope winds on the Big Island [Garrett, 1980], the mixing of free tropospheric air into the transition layer is assumed to dominate. The five variable parameters of the model are the initial boundary layer value of the mixed constituent (in the case of vapor volume mixing ratio:  $q_0$ ), the times at which upward mixing starts ( $t_{up,start}$ ) and peaks ( $t_{up,peak}$ ), the mixing coefficient ( $m$ ), and the height to which the transition layer—defined as the region of mixed boundary-layer and free tropospheric air—grows ( $z_{trans}$ ). Optimal values for the latter four were selected by reducing the root mean square error (RMSE) between the model output and station observations of  $q$ . These optimal values were then used to model diurnal patterns in other trace gases, including the  $H_2^{18}O$  concentration (which is later converted to  $\delta^{18}O$ ), and particle number concentration—with only the initial boundary-layer value varying for each constituent.

The mass balance of the column for  $q$  is

$$\frac{Dq}{Dt} = w_{up}m(q_0 - q) + w_{down}m(q_{z_{max}} - q) , \quad (4.3)$$

where  $q_{z_{max}}$  is a value chosen from nighttime observations to represent the free troposphere and  $w_{up}$  and  $w_{down}$  are the weighting functions that control whether upward or downward mixing dominate, respectively.

The model is discretized at 79 levels in the vertical, spanning 100-4000 m and spaced 50 m apart. The top of the boundary layer is set at 2000 m, which is within the range of heights at which Ridley *et al.* [1997] observed the trade wind temperature inversion by aircraft. At model initiation, heights spanning 100 to 2000 m are assigned the initial boundary-layer  $q$  value, which

is chosen by reducing the RMSE between model output and observations, while heights above are assigned the free tropospheric value estimated from nighttime observations. The model time step is 36 seconds.

An example of the upward weighting function and its effect on the modeled  $q$  profile is shown in Figure 4.1. At model initiation, weights at all heights are set to zero. When upward mixing commences, weights remain zero above the transition layer but are set to one within the boundary layer. The weight at the bottom of the transition layer increases linearly from zero to one as a function of time and reaches its maximum when upward mixing peaks (Figure 4.1a, solid lines). Weights across the transition layer, meanwhile, decrease linearly with height. After upward mixing peaks, the weight at the bottom of the transition layer decreases linearly from one to zero until 9 hours past model initiation (1500 HST), and the weights across the transition layer decrease accordingly (Figure 4.1a, dashed lines). In this manner, upward mixing gradually ramps up and then tails off before the downward mixing phase commences.  $W_{up}$  is zero everywhere once upward mixing ends, just as during upward mixing,  $w_{down}$  is zero everywhere.

To mimic the settling of the atmosphere once the boundary layer is no longer supported by active daytime convection, the weighting function for downward mixing is approximately the reverse of  $w_{up}$ . Once downward mixing commences (after 9 hours past model initiation), weights above the transition layer are set to one, while weights within the boundary layer are set to zero; and, it is the weight at the top of the transition layer—which increases linearly from zero to one—that determines the weights across the transition layer. These decrease linearly to zero at the top of the boundary layer with each time step. Downward mixing ramps up until 14 hours after model initiation (2000 HST), after which point the weighting function remains constant in time. All mixing stops completely 18 hours after model initialization (local midnight).

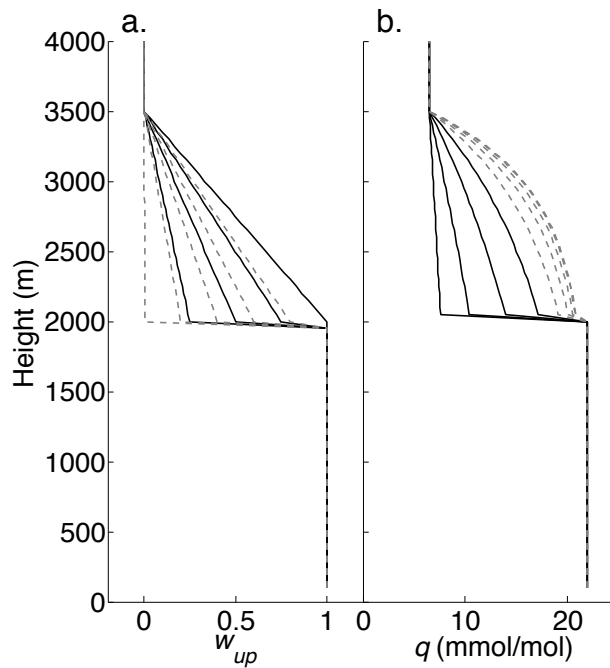


**Figure 4.1.** Profiles of (a) the upward weighting function ( $w_{up}$ ) and (b) the modeled vapor volume mixing ratio ( $q$ ) before (solid) and after (dashed) upward mixing peaks.

In order to select the best parameters for the model, the following parameter values were considered: upward mixing start times were examined for every hour between 0 and 3 hours past model initiation, upward mixing peak times were examined for every hour between 4 and 9 hours past model initiation, mixing coefficients were examined every  $0.1 \text{ hr}^{-1}$  between  $0.2$  and  $1.5 \text{ hr}^{-1}$ , and transition layer heights were examined every 100 m between 3400 m (100 m above MLO) and 4000 m (the top of the model). The best choice for each of these parameters was selected by minimizing the RMSE between model output and  $q$  observations—averaged to each hour of the day—for high and low precipitation efficiency events separately. The best-fit parameters are discussed in Section 3 of this chapter.

### 3. Results

#### 3.1. Strong and weak convection

Peak humidity ( $q_{peak}$ ) and  $\delta^{18}\text{O}$  ( $\delta^{18}\text{O}_{peak}$ ) values were calculated for 1056 days during the three-year experiment (total days = 1096; the instrument did not sample ambient data on the remaining 40 days due to calibrations and maintenance). As Figure 4.2 shows, peak humidity exhibits a bimodal distribution at Mauna Loa Observatory (MLO), with a dry mode centered around 4 mmol/mol and a larger moist mode near 11-12 mmol/mol. (While the location of the moist peak represents an average of winter and summer peaks, the bimodality is present in both seasons.) Since strong convection deepens the boundary layer more effectively than weak convection, it is expected that higher vapor volume mixing ratios will be recorded at MLO when strong convection efficiently lofts boundary-layer moisture upward. (One would expect to see strong convection moisten the lower atmosphere off-island as well, though perhaps to a lesser extent, since diabatic heating of the Hawaiian landmass amplifies convection and the humidity values observed at MLO.) On dry days, in comparison, the fact that the low vapor volume mixing ratios are similar to nighttime values ( $q_{night}$ ) indicates that little if any boundary-layer moisture reaches the height of the Observatory when convection is weak. Consequently, the bimodality in  $q_{peak}$  is used to devise an operational definition for strong and weak convection: we define moist or strong convective days as those in which  $q_{peak} > 7$  mmol/mol and dry or weak convective days as those in which  $q_{peak} \leq 7$  mmol/mol. Accordingly, 790, or 74.8%, of the measurement days are characterized by strong convection at MLO.

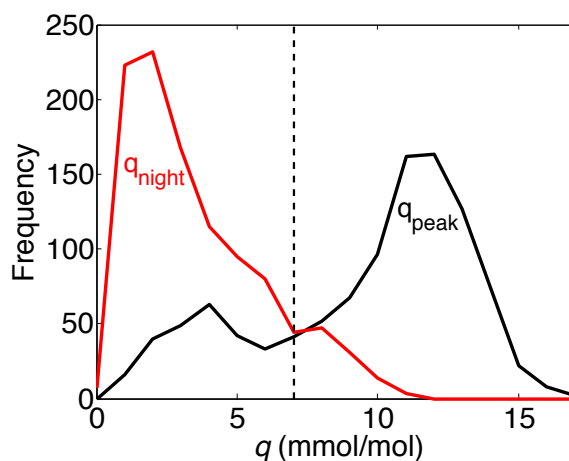


**Figure 4.2.** Frequency distributions of the peak daytime (black) and nighttime (red) vapor volume mixing ratios ( $q$ ) at Mauna Loa Observatory for the period October 2010-September 2013.

Using the isotope ratios to further distinguish amongst strong convective days at MLO, 180 moist days are classified as having low precipitation efficiency (22.8% of moist days) and 146 moist days as having high precipitation efficiency (18.5% of moist days). Figure 4.3 illustrates the bivariate distributions in  $q_{peak}$  and  $\delta^{18}O_{peak}$  associated with these two types of strong convective events, which are henceforth simply referred to as high and low precipitation efficiency days. Bivariate distributions for all measurement days and dry days are also shown for comparison. Although each day's classification is based on a single pair of points, the data nevertheless cluster around lines representing the temporal evolution of physical processes. Indeed, while the peak humidity and  $\delta^{18}O$  values for all low precipitation efficiency days (low  $e$ ) cluster around the dashed mixing line, the values for all high precipitation efficiency days (high  $e$ ) cluster along the solid Rayleigh distillation line. This finding suggests that a single pair of  $q$  and  $\delta^{18}O$  values is both a physically representative and efficient way to distinguish Rayleigh and mixing processes during a 24-hour period at MLO. Figure 4.4 lends additional support to this

claim by showing three-year means in  $q$  and  $\delta^{18}\text{O}$  calculated for each hour of the diurnal cycle for high and low precipitation efficiency days. These, too, follow the Rayleigh distillation (solid) and mixing (dashed) lines, respectively.

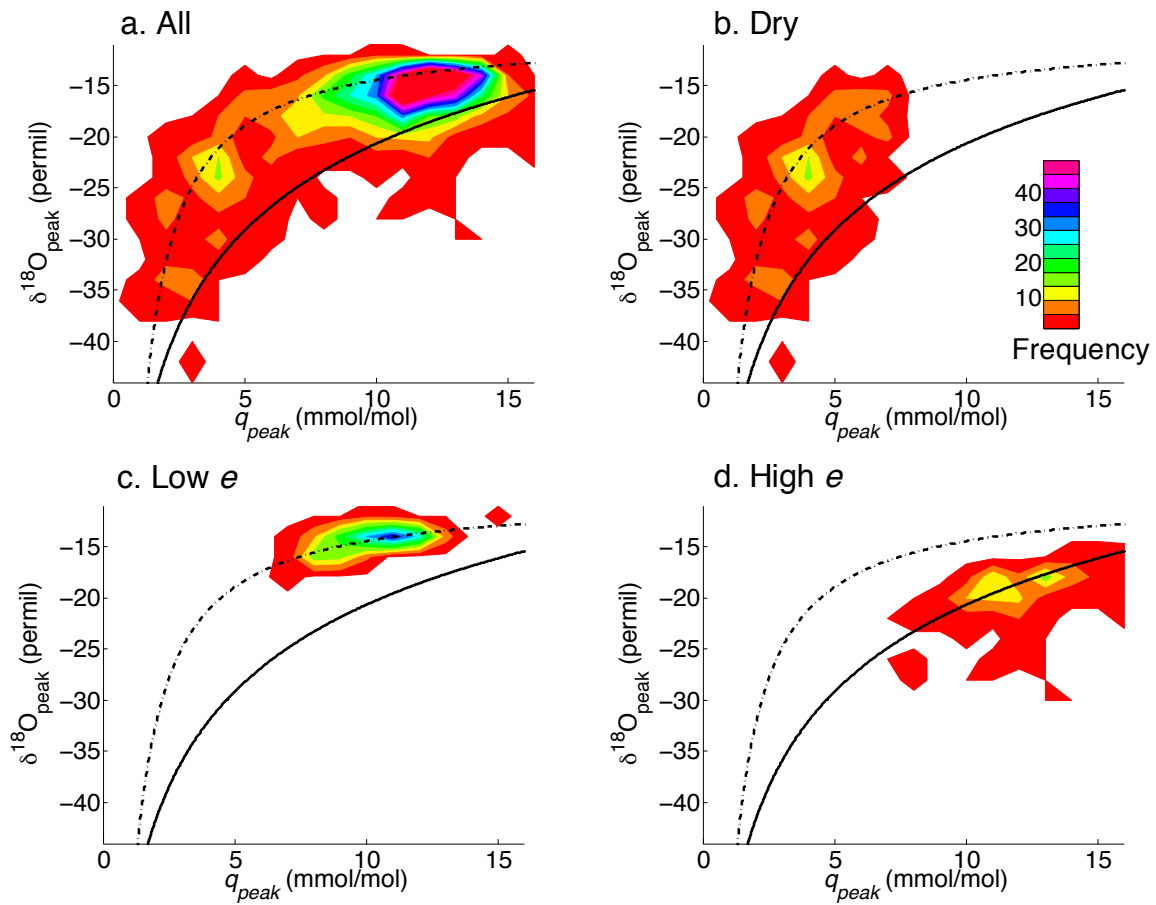


**Figure 4.3.** Bivariate frequency distributions of MLO  $q_{peak}$  and  $\delta^{18}\text{O}_{peak}$  for (a) all days during the three-year measurement campaign, (b) dry days, when convection is weak and boundary-layer air masses fail to reach the height of the Observatory, (c) low precipitation efficiency days, and (d) high precipitation efficiency days.

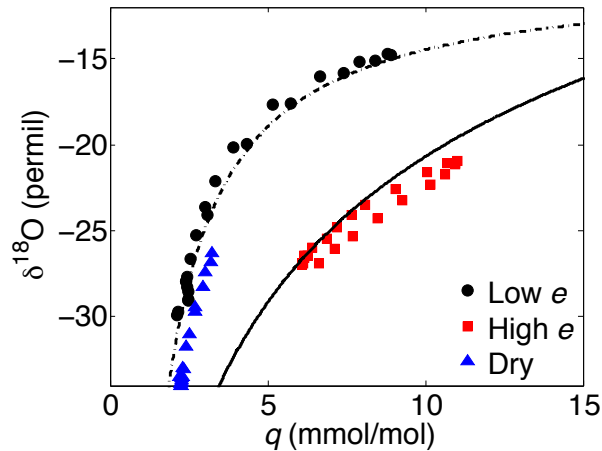


**Figure 4.4.** The bivariate distributions of  $q$  and  $\delta^{18}\text{O}$  values for low precipitation efficiency days (black circles), high precipitation efficiency days (red squares), and dry or weak convective days (blue triangles). The symbols represent three-year means for each hour of the day. The solid line represents a hypothetical Rayleigh distillation process, while the dashed line represents idealized mixing between the subtropical boundary layer and free troposphere.

### 3.2. Large-scale controls on MLO convection

While the Hawaiian Islands are located within or very near the perennial subtropical high, differences in large-scale circulation are nevertheless apparent when we distinguish moist days from dry days and moist days with high isotopic anomalies from moist days with low isotopic anomalies. Figure 4.5 shows composites from the ECMWF Reanalysis ERA-Interim of jet-level winds, total column water (TCW), and surface-level wind and pressure fields for the mixing-like (low  $e$ ), Rayleigh-like (high  $e$ ), and dry days (weak convection) at MLO. Figure 4.6 shows the same variables as anomalies from the three-year mean.

On days in which the precipitation efficiency is defined as low, a branching of the mid-latitude jet occurs, creating a westward retraction and strengthening of 200-hPa winds near Hawaii (Figure 4.6a). This pattern is stronger during winter (DJF) than other seasons (not shown). Near the jet exit region, a low-pressure anomaly forms at the surface ( $\sim 45^\circ\text{N}$ ,  $150^\circ\text{W}$ ),

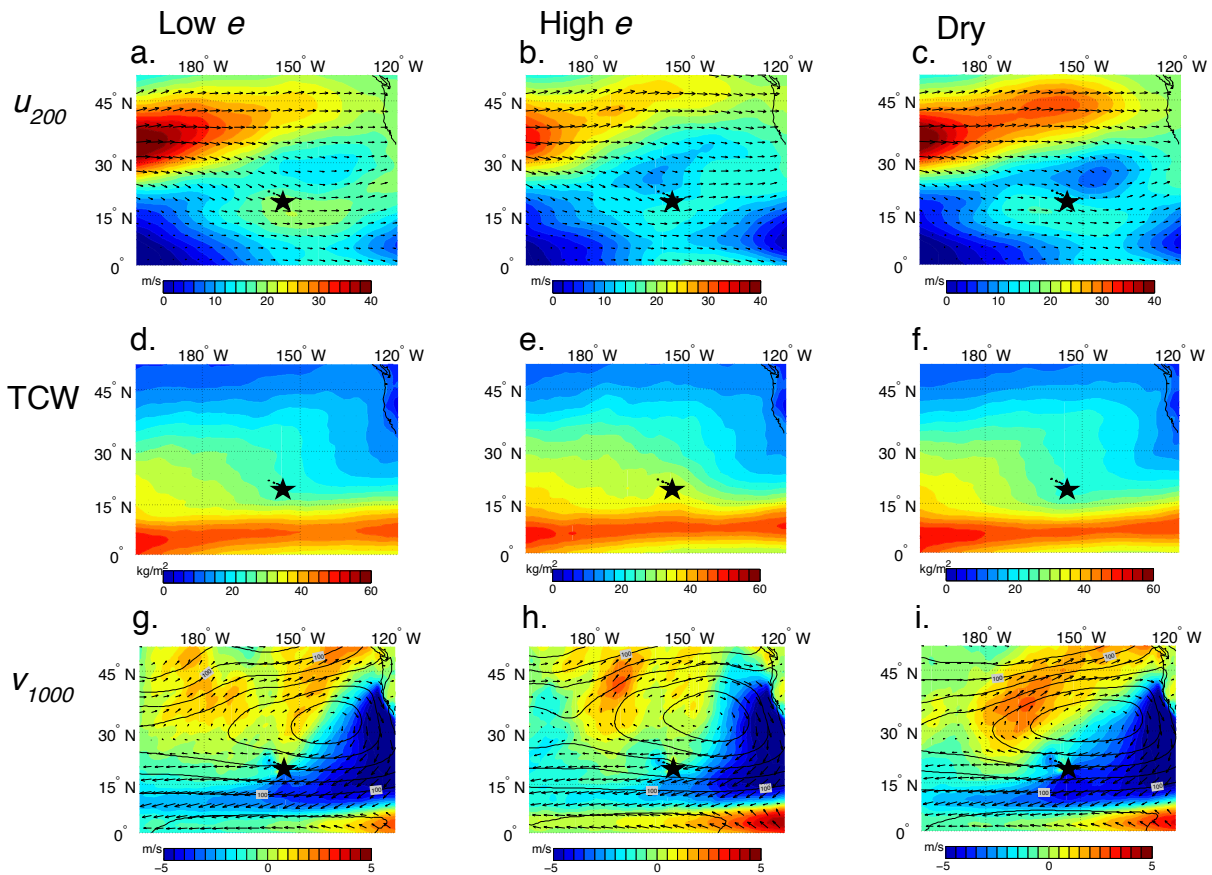


**Figure 4.5.** Annual composites of (a-c) 200-hPa zonal winds, with mean 200-hPa wind vectors represented by arrows, (d-f) total column water (TCW), and (g-i) 1000-hPa meridional winds, with mean 1000-hPa wind vectors represented by arrows. Black contours in panels (g-i) represent mean 1000-hPa geopotential heights, and the 100-m contour is labeled. Contours are every 20 m. From left to right, columns represent low precipitation efficiency days, high precipitation efficiency days, and dry, or weak convective, days. In each panel, the Big Island of Hawaii is marked by the black star.

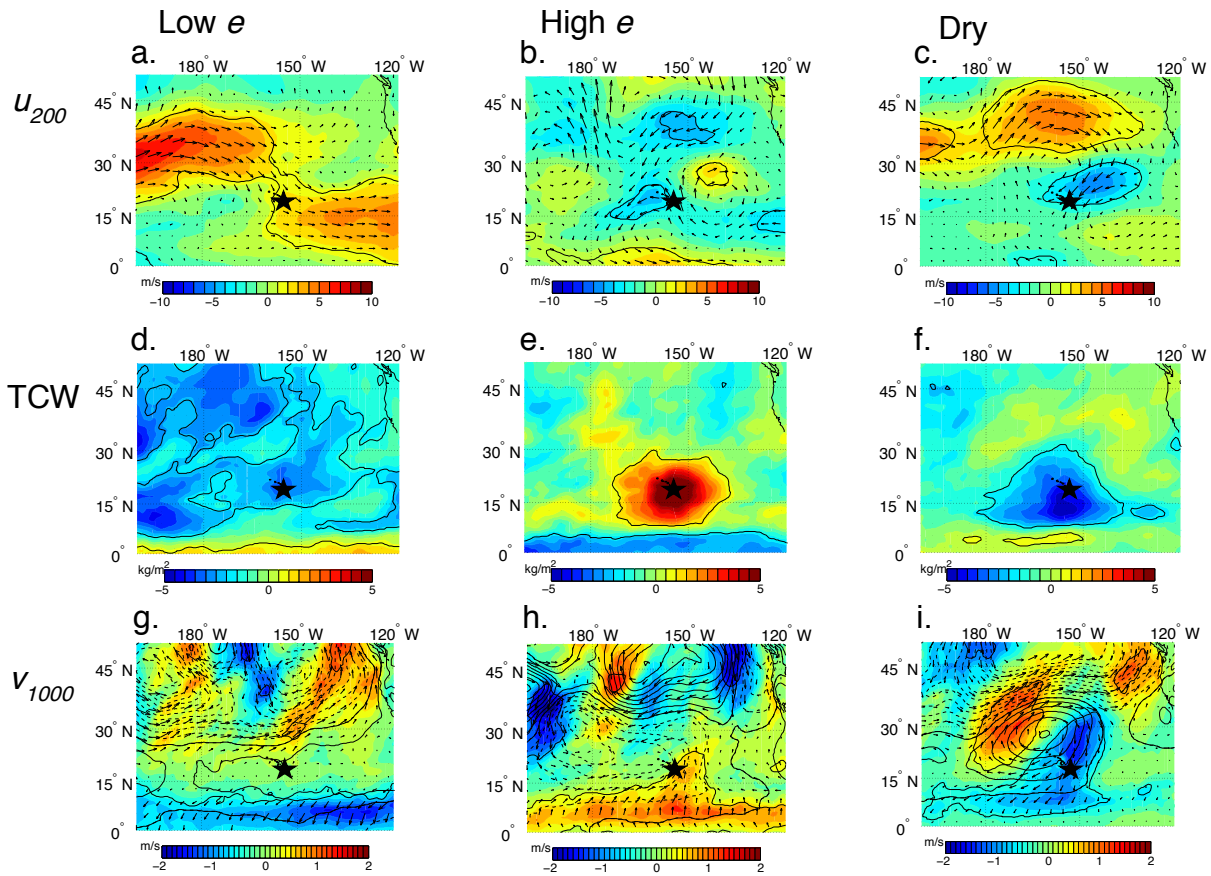


**Figure 4.6.** Anomalies of (a-c) 200-hPa zonal winds and wind vectors (arrows), (d-f) total column water (TCW), and (g-i) 1000-hPa meridional winds and wind vectors (arrows) for low precipitation efficiency, high precipitation efficiency, and dry days (left to right). Anomalies are calculated as differences between mean annual composites for each type of convective classification and the October 2010 – September 2013 mean. Anomalies that are significant at the 95% confidence level are outlined in black. Black contours in panels (g-i) represent anomalies in 1000-hPa geopotential heights, with positive contours solid and negative contours dashed. Contours are every 2 m. In each panel, the Big Island of Hawaii is marked by the black star.

which forces the subtropical high eastward (Figure 4.6g). Anticyclonic flow around the high-pressure region directs easterly (low-level) winds toward Hawaii. With the strengthening of the westerlies aloft, wind shear—defined as the magnitude of the vector difference between the 850-hPa and 200-hPa levels [*DeMaria and Kaplan, 1994*])—is enhanced, and this likely facilitates convection over the Big Island. Indeed, wind shear is significantly stronger at the 95% confidence level for low  $e$  days ( $5.7 \times 10^{-3} \text{ s}^{-1}$ ) than for high  $e$  days ( $4.8 \times 10^{-3} \text{ s}^{-1}$ ) or dry days ( $5.1 \times 10^{-3} \text{ s}^{-1}$ ). Yet though convection is strong, the atmospheric column is relatively dry (Figure 4.6d), which is consistent with the idea that ageostrophic flow near jet exit regions allows dry mid-latitude air to descend into the subtropics [*Cau et al., 2007*]. The mixing of a moist convective boundary layer with a drier-than-normal free troposphere would, in turn, likely promote cloud evaporation and limit precipitation. Consequently, this circulation pattern lends credence to the hypothesis that mixing-like days at MLO represent low  $e$  days.

When the precipitation efficiency is defined as high, there is little anomalous activity at the jet level (Figure 4.6b). Instead, the surface high shifts northward, weakening the anticyclonic circulation that typically transports dehydrated air from the eastern Pacific towards Hawaii. As a result, more tropical air is able to move northeast toward the islands (Figure 4.6h), and an overall moistening of the atmospheric column occurs (Figures 4.5e and 4.6e). This pattern, like the jet-level anomaly pattern associated with low  $e$  days, is stronger in winter (DJF) than during other seasons.

Dry days, in contrast, show both a strengthening and northward shift of the mid-latitude jet (Figure 4.6c) and the formation of a surface high-pressure anomaly over the Hawaiian Islands (Figure 4.6i). As a result of the pressure anomaly, MLO experiences enhanced subsidence, which suppresses convection, as well as enhanced northeasterly flow, which transports dehydrated air

masses from the eastern Pacific. These weak convective days are, consequently, also associated with a drier-than-normal atmospheric column (Figure 4.6f).

Ensemble back trajectories associated with persistent strong convective events (i.e. those lasting three or more days, with no more than one day of separation in between) further illustrate the differences between high and low precipitation efficiency days at MLO (Figure 4.7). Air masses associated with high precipitation efficiency days are more likely to have originated at lower latitudes and to have come from the southeast, in particular. This finding supports the previous conclusion that as anticyclonic circulation in the vicinity of Hawaii weakens, moisture-laden air masses from the tropics are more likely to extend northward. In contrast, for low precipitation efficiency days, MLO air masses are more likely to have traveled from the

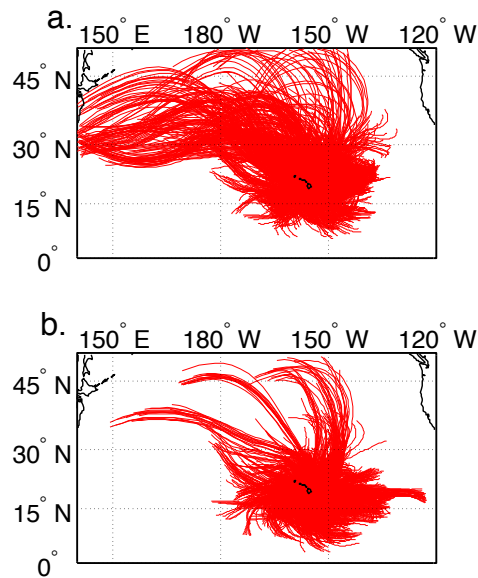


**Figure 4.7.** Three-day ensemble back trajectories calculated from the NOAA HYSPLIT model, using the NCEP-NCAR Reanalysis, for air masses arriving at Mauna Loa Observatory on (a) low or (b) high precipitation efficiency days.

northwest, originating from as far away as the Asian continent. These air masses presumably cross the Pacific following the enhanced southern branch of the jet stream depicted in Figure 4.6a.

Though higher latitude air masses are typically more depleted than lower latitude air masses, the MLO observations reveal higher daytime isotope ratios associated with Figure 4.7a, which depicts numerous northwesterly trajectories. Consequently, vertical mixing and microphysical processes—which determine how much condensate is removed as rain—appear to be more influential in determining the peak water vapor isotope ratio near Hawaii than the zonal origin of the air mass. This finding has key implications for paleo-climate research efforts that aim to interpret isotopic proxy records in terms of moisture source regions. Indeed, for paleo-proxies such as speleothems, which are sensitive to the isotopic composition of water vapor [LeGrande and Schmidt, 2009], the results here suggest understanding how local hydrological processes modify the isotopic signature of the moisture source region will be critical for accurate interpretation of past climate.

### ***3.3. Convective transport of atmospheric constituents***

While variations in transport pathways, brought about by differences in large-scale circulation patterns, may influence the concentrations of atmospheric constituents at MLO, differences in the strength of vertical mixing and microphysical processes may also play an important role. To evaluate the relative importance of vertical mixing versus large-scale transport in regulating vertical distributions of atmospheric constituents during different precipitation efficiency events, we examine the diurnal cycles of eight variables measured at MLO:  $q$ ,  $\delta^{18}\text{O}$ , precipitation, particle number concentration, aerosol scattering coefficient (550 nm), aerosol

backscattering coefficient (550 nm), ozone, and methane. Figure 4.8 shows three-year means of each of these variables for each hour of the day during high  $e$ , low  $e$ , and dry events.

Weak convective or dry days at MLO serve as a helpful reference for variations in atmospheric constituents observed during high and low  $e$  days. As expected, they show the least variation in all eight variables and are characterized by very low values in  $q$ ,  $\delta^{18}\text{O}$ , and particle number concentration. Relatively high ozone values, meanwhile, confirm that the Observatory lies within the free troposphere on these days, which supports our interpretation that convection is too weak to mix boundary-layer moisture upward. Yet though convection is weak during dry days, Figures 4.8b and 4.8d indicate some vertical motion occurs. Indeed, while  $q$  and ozone are nearly constant throughout the 24-hour period, the isotope ratio and particle number concentration both increase during the afternoon, demonstrating their greater efficacy in tracing free tropospheric air masses.

During strong convective days, much higher values of  $q$ ,  $\delta^{18}\text{O}$ , and particle number concentration are observed, and large differences between nighttime and daytime concentrations indicate a clear transition from free tropospheric to boundary-layer air. As shown in Figure 4.8a, the large diurnal variations in humidity for low precipitation efficiency days signify a substantial jump in  $q$  between a relatively moist boundary layer and very dry free troposphere. Mixing between such air masses would dehydrate the boundary layer and limit precipitation. It is therefore no surprise that, on average, precipitation is zero at MLO on low  $e$  days (Figure 4.8c). In contrast, when  $e$  is high, measurable precipitation is evident, and elevated humidity during both day and night suggests sustained convective activity. Small variations in isotope ratio support this claim: *Noone et al.* [2011] observed similar isotopic enrichment over the course of several nights when a tropical plume crossed the Hawaiian Islands and generated heavy

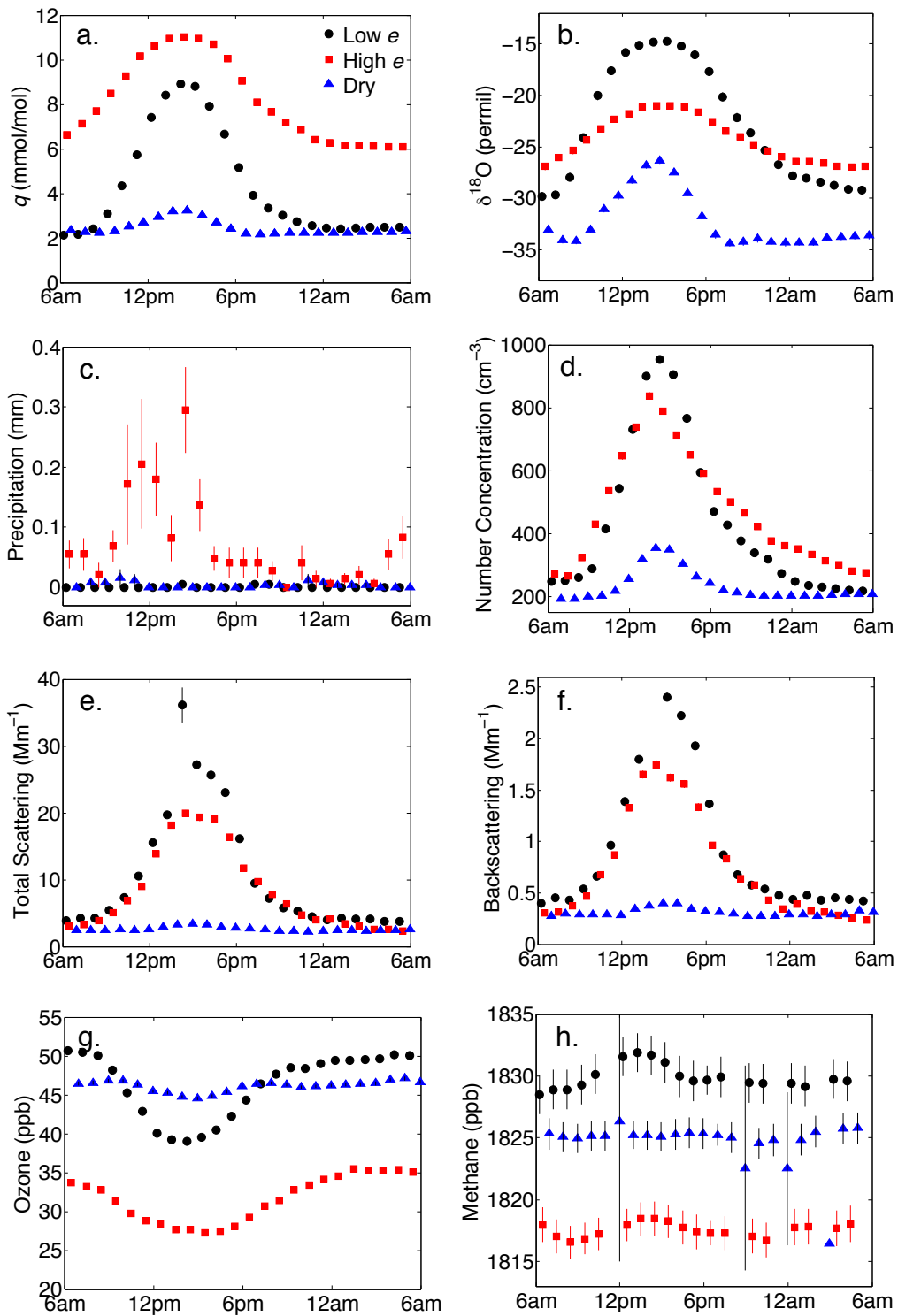


**Figure 4.8.** Three-year means for each hour of the day representing diurnal cycles for low precipitation efficiency (black circles), high precipitation efficiency (red squares), and dry, or weak convective, days (blue triangles). Diurnal cycles are shown for the following variables: (a)

the water vapor volume mixing ratio ( $q$ ), (b) the isotope ratio ( $\delta^{18}\text{O}$ ), (c) precipitation, (d) particle number concentration, (e) aerosol total scattering coefficient, (f) aerosol backscattering coefficient, (g) ozone, and (h) methane. Standard errors for each mean are represented by vertical lines; however, in many cases, the symbols are larger than the errors.

precipitation.

Absolute differences in nighttime isotope ratios among high  $e$ , low  $e$ , and dry days (Figure 4.8b) are consistent with the different transport pathways identified previously. High precipitation efficiency nights, which are often influenced by tropical moisture, exhibit the highest isotope ratios. Meanwhile weak convective nights—during which enhanced anticyclonic circulation channels dry and depleted eastern Pacific air toward the islands—exhibit the lowest isotope ratios. Low  $e$  nights are more depleted than high  $e$  nights, due to the fact that low  $e$  air masses often originate north of Hawaii. However, they are less depleted than weak convective nights since low  $e$  air masses are more likely to have traveled directly from the comparatively enriched western Pacific, instead of undergoing extensive mixing with even higher-latitude air masses.

Similar conclusions may be drawn from the diurnal plots of ozone and methane (Figures 4.8g-h). Concentrations of both trace gases are lowest for high  $e$  days, consistent with relatively clean tropical outflow. In contrast, they are highest for low  $e$  days, when enhanced westerly winds are able to transport pollutants from the Asian continent towards the Hawaiian Islands. Other studies based at MLO have likewise observed high methane or ozone concentrations with westerly or northerly trajectories and low concentrations with southerly trajectories [*Harris et al.*, 1992; *Lin et al.*, 2014; *Oltmans et al.*, 1996; *Ridley et al.*, 1997]. Ozone and methane thus clearly reflect the distinct transport pathways created by the large-scale circulation differences observed.

Aerosol properties, in contrast, are quite similar among the three convective cases at night but exhibit stark differences during the day (Figures 4.8d-f). High precipitation efficiency days show relatively high particle number concentrations during the rise and fall of the boundary layer but lower concentrations (than low  $e$  events) at midday. One possibility, which may be supported by observed precipitation patterns (Figure 4.8c), is that aerosol are effectively scavenged during higher precipitation efficiency conditions. Such findings would support the hypothesis that precipitation processes are more important than proximity to the emission source in controlling number concentrations of particulates [Wood *et al.*, 2012]. A second possibility is that these differences in tracer concentration reflect differences in boundary layer height: were the boundary layer to remain elevated throughout a high  $e$  diurnal cycle but peak at a lower altitude than a low  $e$  event, this could explain the diurnal patterns in number concentrations observed.

### ***3.4. Modeling convective transport for different precipitation efficiency***

To better evaluate whether microphysical processes influence differences in particle number concentration at MLO, we consider whether the mixing model, described in Equation 4.3, can explain the diurnal variations observed. It is assumed that if mixing can fully replicate the diurnal patterns for both high and low  $e$  days, then precipitation scavenging and other microphysical processes are likely negligible. If, on the other hand, mixing can replicate the pattern on low  $e$  days but not high  $e$  days, then microphysical processes may contribute to the tracer concentration differences evident for the two types of strong convective events.

As described in Section 2.6 of this chapter, we use a column model, in which the initial boundary-layer value, the times marking the start and peak of upward mixing, the mixing

coefficient, and the height of the transition layer are allowed to vary. Optimal values for the last four parameters are selected by fitting the model to the  $q$  observations, while initial boundary layer values are selected independently for each tracer by reducing the RMSE between the hourly-averaged model output and the corresponding diurnal pattern. Initial free tropospheric values are set to the nighttime values observed. The best-fit parameters for high and low precipitation efficiency days are listed in Table 4.1.

**Table 4.1.** Best parameters for modeling high and low precipitation efficiency days.

	<b>Low <math>e</math></b>	<b>High <math>e</math></b>
$m$	0.7hr <sup>-1</sup>	0.6hr <sup>-1</sup>
$t_{up,start}$	0700 HST	0600 HST
$t_{up,peak}$	1200 HST	1000 HST
$z_{trans}$	3700 m	3500 m
$q_{BL}$	16 mmol/mol	22 mmol/mol
$q_{FT}$	2 mmol/mol	6.5 mmol/mol
$\delta^{18}\text{O}_{BL}$	-13 permil	-17 permil
$\delta^{18}\text{O}_{FT}$	-30 permil	-27 permil
$O_{3BL}$	27 ppb	14 ppb
$O_{3FT}$	50 ppb	33 ppb
$NC_{BL}$	2400 cm <sup>-3</sup>	3100 cm <sup>-3</sup>
$NC_{FT}$	380 cm <sup>-3</sup>	380 cm <sup>-3</sup>

$m$  = mixing coefficient,  $t_{up,start}$  = start of upward mixing,  $t_{up,peak}$  = peak of upward mixing,  $z_{trans}$  = height at the top of the transition layer,  $BL$  = initial concentration of the boundary layer,  $FT$  = initial concentration of the free troposphere, and  $NC$  = particle number concentration

Although precipitation processes will reduce  $q$  so that it no longer serves as a conserved tracer in the strictest sense, such reductions should be negligible compared to the hourly changes brought about by vertical mixing near Hawaii. The  $q$  observations should thus effectively track mixing during both high and low precipitation efficiency days; and several findings give us confidence that this is the case. First, comparison of the initial model  $q$  profiles with mean

profiles derived from Hilo radiosondes for October 2010-September 2013 (available at <http://weather.uwyo.edu/upperair/sounding.html>) suggests the model initiation is physically reasonable (Figure 4.9). Second, ozone, unlike the moisture variables or particle number concentrations, should be insensitive to cloud and precipitation processes. Therefore, the model's ability to reproduce ozone patterns for both types of strong convective events (Figure 4.10c) suggests the relevant processes are adequately resolved for characterizing vertical motions near Hawaii.

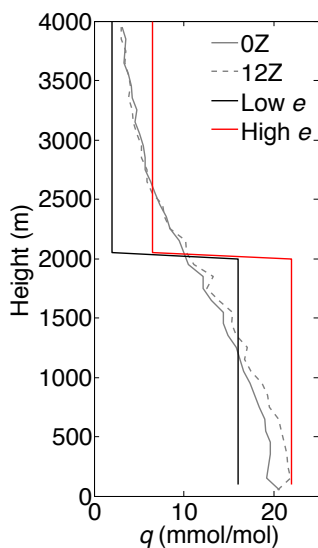


**Figure 4.9.** Initial vapor volume mixing ratio ( $q$ ) profiles used to model vertical mixing during high (red) and low (black) precipitation efficiency convection. Mean 0Z (solid gray) and 12Z (dashed gray)  $q$  profiles derived from Hilo, Hawaii upper air radiosondes for October 2010-September 2013 are shown for comparison.

As indicated by Figure 4.10, vertical mixing readily explains the diurnal variations in  $q$ ,  $\delta^{18}\text{O}$ , and ozone observed during both high and low precipitation efficiency days. (As with  $q$ , large variations in  $\delta^{18}\text{O}$  across the diurnal cycle will first and foremost reflect the transition from free troposphere to boundary layer and back.) While mixing on low  $e$  days begins later than on

high  $e$  days, the mixing coefficient is higher and the transition layer is deeper (Table 4.1). Thus even though the atmospheric column is drier, vertical transport of atmospheric constituents is slightly stronger for a punctuated period of time.

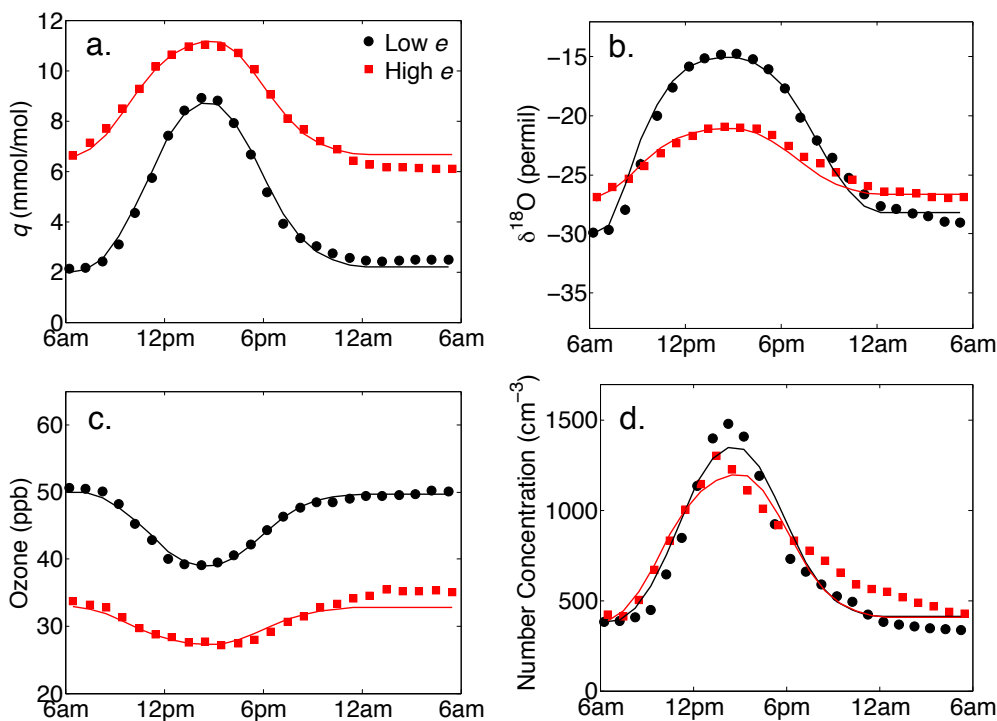


**Figure 4.10.** Observed and modeled diurnal cycles for (a) the water vapor volume mixing ratio ( $q$ ), (b) the isotope ratio ( $\delta^{18}\text{O}$ ), (c) ozone, and (d) particle number concentration on high (red) and low (black) precipitation efficiency days. Lines represent results from the single-column mixing model.

The mixing model also does a fair job of replicating the aerosol diurnal cycle on low  $e$  days; however, it underestimates the peak number concentration (Figure 4.10d). Since there is little or no precipitation when  $e$  is low, vertical mixing should indeed be the principal process regulating MLO number concentrations during these times. Nevertheless, particle nucleation and growth—which are not included in the model formulation—may amplify the boundary-layer concentrations observed in the early afternoon.

In contrast, the model cannot reproduce the observed diurnal pattern on high  $e$  days: the particle number concentration peaks at 1300 HST, well before the predicted peak at 1500 HST, and then declines slowly throughout the afternoon and evening. The model, meanwhile, follows a steeper hyperbolic curve. These discrepancies suggest particles are scavenged from boundary-layer air, which reaches MLO near midday, and produced at altitudes above the Observatory, creating the appearance of higher-than-expected number concentrations at night. Together, these findings provide evidence that microphysical processes may be particularly active in shaping vertical distributions of aerosols on high  $e$  days.

Finally, while it is possible to reproduce diurnal patterns in  $q$ ,  $\delta^{18}\text{O}$ , and ozone by treating the top of the boundary layer as a material surface that moves up and down over the course of the day, this is only the case so long as a transition layer—in which mixing between the boundary layer and free troposphere has previously occurred—is included in the initial tracer profile. Consequently, not all of the vertical mixing influencing the diurnal patterns discussed need have occurred on a single day; mixing may have occurred over the course of several days.

#### **4. Discussion**

This chapter has used isotope ratios in water vapor to characterize the precipitation efficiency ( $e$ ) of strong convective events at the Mauna Loa Observatory (MLO) and to examine how large-scale circulation, vertical mixing, and microphysics vary between high and low precipitation efficiency days. The analysis shows that while high precipitation efficiency days are associated with a weakening of anticyclonic circulation that allows moist tropical air to reach the Hawaiian Islands, low precipitation efficiency days are associated with strengthened westerly

flow and enhanced wind shear. These results are consistent with model studies of deep convection by *Ferrier et al.* [1996], which found higher precipitation efficiency where atmospheric moistening was greater and upshear convection reduced. The circulation patterns identified, as well as the associated background concentrations of methane and ozone, are also consistent with what previous studies report. Several papers, for example, have studied the westerly transport pathway—which is found here to be associated with low  $e$  and higher concentrations of ozone and methane—[*Harris and Kahl*, 1990; *Merrill et al.*, 1989; *Ridley et al.*, 1997]. Westerlies not only transport high concentrations of trace gases and particles from Eurasia [*Harris et al.*, 1992; *Ridley et al.*, 1997; *Perry et al.*, 1999], but they also tend to occur more frequently in winter, when emissions of pollutants like methane are higher [*Harris et al.*, 1992]. In addition, cyclonic variability associated with enhanced jet flow may encourage stratosphere-troposphere exchange, which has been linked to high ozone at Hawaii [*Oltmans et al.*, 2004]. Importantly, if the circulation patterns that channel westerly flow toward Hawaii become more frequent, either as a result of climate forcing or decadal climate variability, as recent work has suggested possible [*Oltmans et al.*, 2006; *Lin et al.*, 2014], this chapter’s findings indicate lower precipitation efficiency events will become more prevalent. Since the position of the subtropical high—a well-resolved climate model feature—appears to be a distinguishing characteristic of the circulation patterns identified, future work might effectively use general circulation model simulations to test how the frequency of high and low precipitation efficiency events near Hawaii will change with future warming.

Despite clear differences in methane and ozone concentrations between high and low precipitation efficiency days, background (nighttime) particle number concentrations for the two types of strong convection were quite similar. This is not surprising: previous research suggests

high particle and trace gas concentrations do not always coincide [Ridley *et al.*, 1997]. Indeed, while westerly flow often transports high ozone concentrations toward Hawaii, cloud and precipitation processes may wash out aerosol en route. Similarly, low-ozone air from the tropics may be characterized by higher-than-expected particle number concentrations due to recent vertical mixing between boundary-layer and free tropospheric air. Thus, both mixing and microphysical processes can obfuscate the expected positive correlation between trace gas and particulate concentrations, which highlights the value of the isotopic measurements in distinguishing these processes.

Vertical mixing and microphysical processes also clearly regulate *daytime* particle number concentrations at MLO, with microphysical processes more influential on high *e* days. As discussed by Clarke [1993] and Nilsson *et al.* [2001], scavenging of aerosol—for example by clouds and precipitation—reduces the condensation sink for particle-forming gases like SO<sub>2</sub>, which may ultimately facilitate new particle formation. Scavenging could therefore explain the unexpected decline in particle number on high *e* days, while subsequent nucleation could account for the higher-than-expected concentrations observed later during boundary-layer collapse. Convective activity may also enhance particle formation by lofting pre-cursor gases [Nilsson *et al.*, 2001]—a mechanism that may be particularly effective in nucleating sulfate particles over volcanic islands like Hawaii [Thornton *et al.*, 1997]—or by increasing the environmental relative humidity [Hegg *et al.*, 1990; Perry and Hobbs, 1994].

Disparities in particle size provide further evidence of microphysical differences between high and low *e* days. The Angstrom exponent, which is calculated, following Bodhaine [1996], from the scattering coefficients measured at three wavelengths, gives a very approximate indication of particle size distribution [Schuster *et al.*, 2006]. (To minimize uncertainties in the

data, mean scattering is first calculated for all three wavelengths for each hour of the day and the Angstrom exponent estimated from these averages.) During low  $e$  nights and when convection is weak, the Angstrom exponent is close to the free tropospheric baseline value of 0.77 reported by *Kaufman et al.* [2001], indicating older particles (Figure 4.11). Uncertainties in the measurement of the total scattering coefficient (see Figure 4.8g) likely influence the outlier at 1400 HST. In contrast, when  $e$  is high, values near 2.0 are observed throughout the 24-hour period, indicating that at least half the aerosol concentration is composed of fine mode particles with an effective radius less than 200 nm [cf. *Schuster et al.*, 2006]. Smaller radii are consistent with recent nucleation and support the idea that precipitation processes associated with convective mixing facilitate new particle formation.

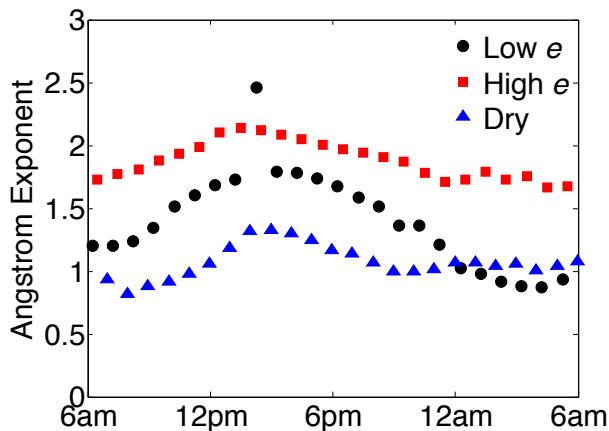


**Figure 4.11.** The Angstrom exponent on low precipitation efficiency days (black circles), high precipitation efficiency days (red squares), and dry, or weak convective, days (blue triangles), calculated from three-year means in the total scattering coefficient at three wavelengths for each hour of the diurnal cycle.

Though Hawaii’s unique topography no doubt enhances convective activity on the island, the fact that the convective events evaluated in this chapter are associated with robust large-scale circulation features suggests the results presented here are representative regionally. Note, too,

that increases in total column moisture during high  $e$  days occur over a much larger geographic area than the Hawaiian archipelago (Figure 4.6e). Nevertheless, a global evaluation of large-scale controls on precipitation efficiency is still needed. With satellite-borne instruments like NASA's Tropospheric Emission Spectrometer able to retrieve isotope ratios from space [e.g. *Worden et al.*, 2012], future studies could expand the present analysis to a much larger geographic area and link precipitation efficiency and cloud and moisture fields on a global scale.

## 5. Conclusion

This chapter has used a three-year time series of measurements of the water vapor  $^{18}\text{O}/^{16}\text{O}$  ratio to characterize the precipitation efficiency of convective activity at the Mauna Loa Observatory (MLO) on the Big Island of Hawaii. Of the 74.8% of observational days during which boundary-layer growth was significant and convection defined as strong, 22.8% exhibited low precipitation efficiency (low  $e$ ) and 18.5% high precipitation efficiency (high  $e$ ). Events with medium values of precipitation efficiency were excluded from the analysis in order to emphasize differences between microphysical processes. Diurnal patterns of MLO measurements—comprised of means calculated for each hour of the day—confirm that precipitation is only measureable for high  $e$  days.

Using the isotopic information to identify synoptic drivers of strong convection, two distinct large-scale circulation patterns were identified. These suggest low precipitation efficiency days are associated with a branching of the subtropical jet and strengthened westerly winds, which facilitate the transport of pollution from Eurasia. In contrast, high precipitation efficiency days are associated with enhanced tropical outflow, resulting in relatively clean and

moist conditions. While concentrations of ozone, methane, and the nighttime (background) isotope ratios reflect these distinct transport pathways, particle number concentrations are more sensitive to local vertical mixing and microphysical processes.

A single column model demonstrated that while vertical mixing associated with strong convective activity explains most of the diurnal variations in particle number concentration on low  $e$  days, it cannot replicate the diurnal patterns observed on high  $e$  days. During high  $e$  events, number concentrations declined before the peak in boundary-layer growth and around times when precipitation was typically observed at MLO. In contrast, later in the evening, number concentrations were higher than model predictions. These discrepancies suggest precipitation scavenging may play a key role in removing pre-existing aerosol and facilitating particle nucleation at altitudes above the Observatory.

If westerly transport patterns continue to become more frequent, for example as a result of decadal climate variability [Lin *et al.*, 2014], the results of this work suggest precipitation scavenging and its associated enhancement of new particles will become less prevalent at MLO. Since both the concentration and size of particles regulate aerosol direct and indirect effects, these changes could have important implications for climate. Moreover, if precipitation efficiency also influences low-cloud cover by altering vertical distributions of moisture, as recent studies claim [e.g. Stevens *et al.*, 2014; Zhao, 2014], these circulation changes could further modify the shortwave cloud feedback on climate. It is still unclear, however, whether reductions in precipitation efficiency will increase or decrease shortwave cloud forcing. With isotopic tracers an effective tool for characterizing precipitation efficiency and global observations of isotope ratios in water vapor available through remote-sensing, future work will be well poised to evaluate the relationships between precipitation efficiency and cloud properties from an

observational perspective.

## CHAPTER V

### Linking precipitation efficiency and low-cloud cover using remotely-sensed isotope ratios in water vapor

#### 1. Introduction

Cloud processes in climate models continue to contribute large uncertainties to predictions of future climate [Boucher *et al.*, 2013]. In particular, differences in how models represent lower-tropospheric mixing—the process by which low-level clouds mix with and evaporate into their free tropospheric environment—may explain the large spread in global temperature rise predicted by models [Sherwood *et al.*, 2014]. Because such mixing reduces the bulk precipitation efficiency and moistens the lower free troposphere at the expense of the boundary layer, Sherwood *et al.* [2014] claimed it is responsible for decreasing low-cloud cover. This hypothesis complements earlier studies that suggest enhanced dry air entrainment with warming will reduce boundary layer humidity and inhibit low-cloud formation [Rieck *et al.*, 2012; Brient and Bony, 2013].

Yet not all studies support the idea that more mixing and lower precipitation efficiency reduce low-level cloudiness. In a series of sensitivity tests and global warming experiments, Zhao [2014] showed that models with more mixing and lower precipitation efficiency have higher, not lower, fractions of low-level cloud. The increased cloud fraction strengthens shortwave cloud radiative forcing, resulting in greater cooling of Earth's surface. Such discrepancies underscore the need for observations that can verify the relationships among mixing, precipitation efficiency, and cloudiness and ultimately help evaluate the accuracy of general circulation model simulations.

Isotope ratios in water (e.g. D/H,  $^{18}\text{O}/^{16}\text{O}$ ) provide such an observational tool. Since heavier isotopes condense more readily than their lighter counterparts, the isotope ratio of water vapor in a convective plume follows a predictable distillation. When moisture ascends pseudoadiabatically, such that all condensate immediately rains out, the isotopic profile follows the well-known Rayleigh distillation:  $R = R_0(q/q_0)^{\alpha-1}$ , where  $R$  is the ratio of heavy-to-light isotopes,  $q$  is the vapor mixing ratio, 0 represents a reference level, and  $\alpha$  is a temperature-dependent fractionation factor [Dansgaard, 1964]. When the precipitation efficiency, or the conversion of condensate to precipitation, is less than 100%, the distillation process is modified such that isotopic depletion of the air mass will not be as great [Dansgaard, 1964; Jouzel and Merlivat, 1984; Noone, 2012]. And, in the case that no precipitation forms, the isotopic composition of the ascending parcel is conserved, until mixing with another air mass takes place. Hence, while convection with high precipitation efficiency should, by definition, adhere to a Rayleigh model, empirical evidence suggests low precipitation efficiency convection will resemble a mixing process, in which moisture is exchanged between a cloudy boundary layer and a dry free troposphere (see Chapter 4). Isotopic theory places constraints on the bivariate distributions of specific humidity and vapor isotope ratios expected in both cases [Worden *et al.*, 2007; Noone, 2012].

Exploiting such constraints, Lee *et al.* [2011] used remotely sensed estimates of the D/H isotope ratio from NASA's Tropospheric Emission Spectrometer (TES) aboard the Aura spacecraft to qualify the importance of mixing between the boundary layer and free troposphere in regulating humidity patterns across the tropics. Because they observed that clear sky regions were isotopically similar to regions with non-precipitating cloud, they surmised that detrainment from low-level clouds broadly influences free tropospheric humidity—a conclusion also backed

by other TES-based work [Brown *et al.*, 2013]. Yet no research to date has directly compared TES isotope ratios with observations of cloud fraction to link lower-tropospheric mixing, precipitation efficiency, and shortwave cloud feedbacks.

With global observations spanning the last decade, TES retrievals of water vapor isotope ratios are well suited for examining climatologies of lower-tropospheric mixing and precipitation efficiency across broad regions. This study pairs TES retrievals with observations of cloud properties from MODIS (the Moderate Resolution Imaging Spectroradiometer) to evaluate whether isotopically-derived estimates of vertical mixing and precipitation efficiency are correlated with low-cloud fraction. The analysis considers four Pacific regions: the northern mid-latitude storm track, the northern subtropics near Hawaii, the warm pool region, and the southern subtropics off the coasts of Peru and Chile (Figure 5.1). Ground-based measurements of water vapor isotope ratios from the Mauna Loa Observatory (MLO) on the Big Island of Hawaii are also used to verify the relationships observed by satellite. These measurements provide an

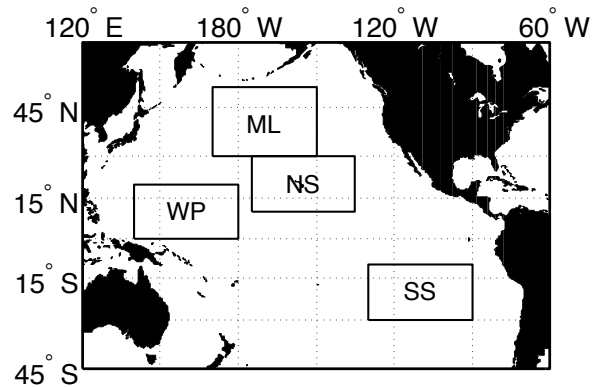


**Figure 5.1.** Map of the four study regions: the mid-latitude storm track region (ML), the western Pacific warm pool region (WP), the northern subtropics near Hawaii (NS), and the southern subtropics (SS). Each region spans 20° of latitude and 40° of longitude.

independent evaluation of the relationship between precipitation efficiency and cloud cover in the northern subtropical region while also helping verify that the TES retrievals effectively distinguish high and low precipitation efficiency convection.

## **2. Data Sets**

### ***2.1. Remotely sensed isotope ratios***

NASA's Tropospheric Emission Spectrometer (TES), aboard the Aura spacecraft, is a step-and-stare instrument, which has operated predominately in nadir-viewing mode since its launch in 2004. The combined horizontal footprint of the infrared detectors is 5.3 km by 8.4 km [Worden *et al.*, 2006]. Approximately every two days, Aura completes a global survey, during which time TES retrieves 500-2000 atmospheric profiles, including profiles of the water vapor volume mixing ratio and the HDO/H<sub>2</sub>O ratio.

The new version 5 data, which have increased the vertical resolution and information content of the lower atmosphere, make it possible to measure H<sub>2</sub>O and HDO variability in both the boundary layer and free troposphere—even when there is only one degree of freedom associated with HDO [Worden *et al.*, 2012]. Consequently, it is possible to derive not only a mean isotope ratio for the lower free troposphere, as previous studies have done [Worden *et al.*, 2007; Brown *et al.*, 2008; Lee *et al.*, 2011; Brown *et al.*, 2013], but also an isotopic gradient in the lower atmosphere. This study uses version 5 H<sub>2</sub>O and HDO volume mixing ratios from global surveys and special observations spanning 22 August 2004 through the end of 2012.

For the purposes of this analysis, the data are quality-controlled by selecting daytime profiles with at least one degree of freedom in HDO and at least three degrees of freedom in

H<sub>2</sub>O. Furthermore, because the height at which the retrieval sensitivity peaks changes under cloudy conditions [Lee *et al.*, 2011], only profiles with an effective cloud optical depth < 0.2 are considered. Though such filtering limits the analysis to clear-sky conditions, the isotopic profiles still provide information about recent cloud and precipitation formation, since isotope ratios record the condensation history of air masses [Gat, 1996]. The selected HDO data are corrected for a 6.3% bias, as recommended by Worden *et al.* [2011, 2012] based on comparison with Mauna Loa *in situ* data. Although a height-varying bias correction has recently been proposed for the version 5 data, this update is based on isotopic measurements made inflight in Alaska [Herman *et al.*, 2014]. Given this study's focus on latitudes south of 50°N (with a primary focus on the tropics and subtropics), the older Hawaii correction is preferred. The corrected HDO data are then averaged for a given region and time period and converted to delta notation following Worden *et al.* [2012]:  $\delta D = 1000[\text{HDO}/\text{H}_2\text{O}/(3.11 \times 10^{-4}) - 1]$ , where HDO and H<sub>2</sub>O are the volume mixing ratios of each species.

## ***2.2. Ground-based isotope ratios***

Both  $\delta D$  and  $\delta^{18}\text{O}$  have been measured continuously at Mauna Loa Observatory (MLO) since the fall of 2010 with a Picarro water vapor isotopic analyzer (model L1115-i). Using the peak daytime  $\delta^{18}\text{O}$  values observed by the Picarro analyzer during the period October 2010-September 2013, Chapter 4 characterized the precipitation efficiency ( $e=P/C$ , where  $P$ =the rate of precipitation and  $C$ =the rate of condensation) of strong convective events near Hawaii. While the specific humidity at MLO was used to define the strength of convection, relatively enriched humid days were classified as having low precipitation efficiency and relatively depleted humid days were classified as having high precipitation efficiency. Since this characterization was

extensively evaluated, it provides a unique opportunity to independently test the relationship between precipitation efficiency and cloud fraction near Hawaii and to evaluate the ability of TES profiles to distinguish high and low precipitation efficiency events.

### ***2.3. Remotely sensed cloud properties***

Mean daytime cloud fraction, cloud water path (liquid and ice), cloud top pressure, and cloud optical depth (liquid and ice) are investigated for the period 22 August 2004 through the end of 2012 using the level 3 daily data from MODIS on Aqua. MODIS, or the Moderate Resolution Imaging Spectroradiometer, scans across a 2330-km swath, with spectral bands ranging from 0.4  $\mu\text{m}$  to 14.4  $\mu\text{m}$ . Because Aqua is part of the same satellite constellation as Aura, it too provides global coverage every 1-2 days. While parts of this analysis use the native  $1^\circ \times 1^\circ$  grid of the level 3 data, others average the data to a  $5^\circ \times 5^\circ$  grid for a more robust statistical comparison with TES. Low-level cloud cover is evaluated by isolating those scenes in which the cloud top pressure exceeds 680 hPa—the pressure of the Mauna Loa Observatory.

## **3. Results**

### ***3.1. Linking precipitation efficiency and cloud cover near Hawaii***

To test whether precipitation efficiency is strongly correlated with cloud cover, we first investigate MODIS cloud properties near Hawaii for the high and low precipitation efficiency ( $e$ ) days defined in Chapter 4. Figure 5.2—which shows differences in total-column cloud properties for high minus low  $e$ —suggests that the higher the precipitation efficiency, the larger the mean daytime cloud fraction over the Hawaiian Islands. Cloud water path near the archipelago is also

greater for high  $e$  and is strongly correlated with a higher cloud optical depth, suggesting an enhanced shortwave cloud feedback. These findings are consistent with the idea that more mixing and lower precipitation efficiency should reduce cloud cover.

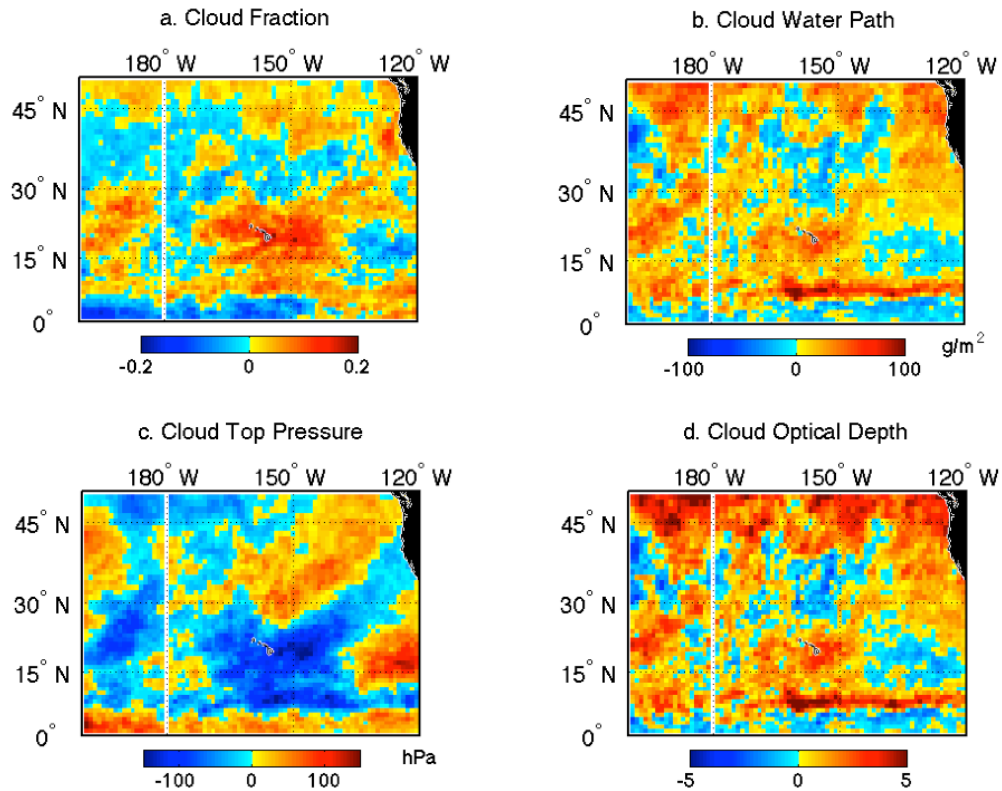


**Figure 5.2.** Differences for high minus low precipitation efficiency days at Mauna Loa Observatory in the following cloud properties: (a) total-column cloud fraction, (b) cloud water path, (c) cloud top pressure, and (d) cloud optical depth. Since pressure decreases with altitude, negative differences indicate higher cloud tops.

However, as Figure 5.1c demonstrates, increases in cloud fraction on MLO’s high  $e$  days are also correlated with reductions in cloud top pressure, which indicates deeper convection. These high clouds develop along a southwesterly trajectory, stretching from the Intertropical Convergence Zone (ITCZ) toward the United States. The pattern is reminiscent of tropical plumes and, in their more extreme manifestation, atmospheric rivers, which are known to induce

intense precipitation along the US West Coast [Ralph *et al.*, 2006; Neiman *et al.*, 2008; Leung and Qian, 2009; Dettinger *et al.*, 2011]. Consequently, it is not clear whether the positive correlation between precipitation efficiency and cloud cover simply reflects variations in the depth of convection. Limiting the analysis to low-clouds (cloud top > 680 hPa) results in a weaker correlation, and the plume-like pattern is no longer apparent. Nevertheless, high  $e$  days still show greater cloud cover and cloud water path over Hawaii (Figure 5.3). Therefore, precipitation efficiency and low-cloud fraction appear to be positively correlated near Hawaii, which suggests the same relationship ought to be observed when comparing TES and MODIS.

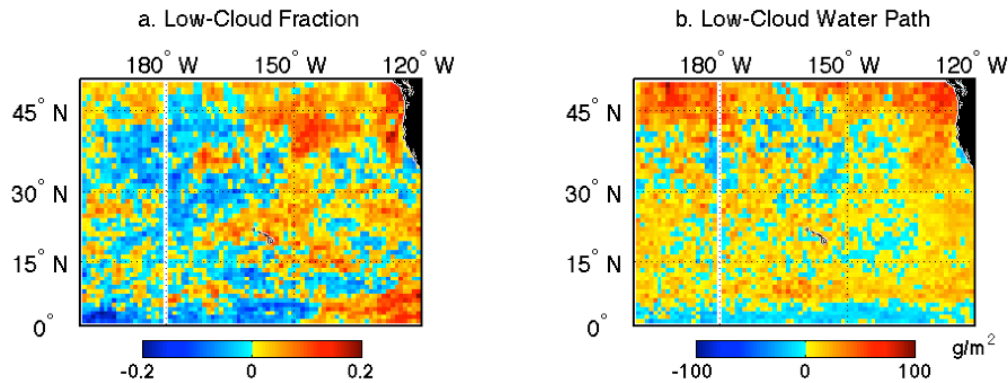


**Figure 5.3.** Differences for high minus low precipitation efficiency days at Mauna Loa Observatory in (a) the fraction and (b) cloud water path of low-level clouds (cloud top > 680 hPa) .

To verify that TES is also able to distinguish high from low  $e$  days at MLO, the remotely sensed isotopic retrievals are averaged across a  $10^\circ \times 10^\circ$  box with the Big Island at its center. When the ground-based measurements suggest the precipitation efficiency is high, TES detects a moister atmospheric column between approximately 950-600 hPa (Figure 5.4a). More moisture in the lower atmosphere is consistent with the notion that convective activity transports boundary-layer moisture upwards. TES also sees a more depleted atmospheric column between approximately 700-450 hPa (Figure 5.4b), suggesting a total water removal process (such as

precipitation) in the lower and mid-free troposphere.

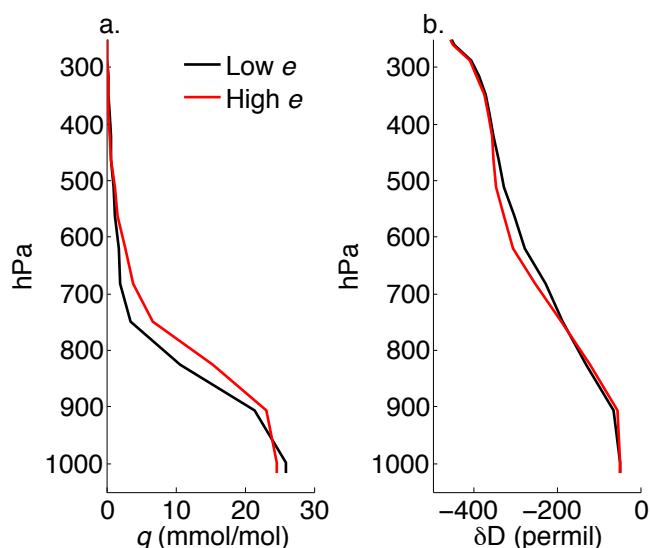


**Figure 5.4.** For the region spanning  $15^\circ$  to  $25^\circ\text{N}$  and  $150^\circ$  to  $160^\circ\text{W}$ , mean TES profiles of (a) the vapor volume mixing ratio ( $q$ ) and (b) the isotope ratio ( $\delta D$ ) for high (red) and low (black) precipitation efficiency days observed at the Mauna Loa Observatory between October 2010 and December 2012.

Plotting bivariate distributions of the TES vapor volume mixing ratio ( $q$ ) and isotope ratio profiles in  $\delta D$ - $q$  space helps accentuate the differences between high and low  $e$  days (Figure 5.5). On low  $e$  days, the isotope ratio changes gradually at high humidity but rapidly at low humidity, as one would expect during a mixing processes. In contrast, on high  $e$  days, the isotope ratio changes more nearly linearly with  $q$ , as might occur during Rayleigh distillation [Dansgaard, 1964]. Though not as distinct in their curvature as isotopic theory would predict, the average TES curves are nevertheless clearly distinguishable, which suggests TES is well-suited for classifying high and low precipitation efficiency across the four study regions (Figure 5.1).

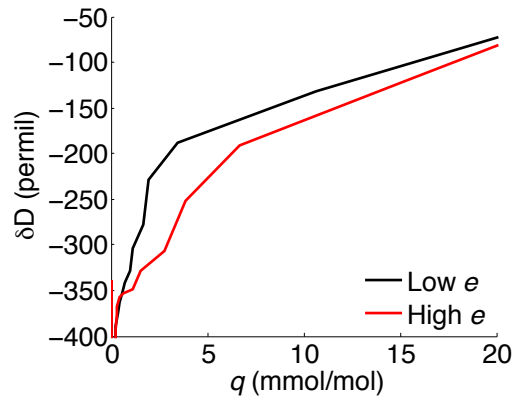


**Figure 5.5.** Bivariate distributions of the  $q$  and  $\delta D$  profiles shown in Figure 5.4 for high (red) and low (black) precipitation efficiency days at Mauna Loa Observatory.

### 3.2. Linking precipitation efficiency and cloud cover across four regions

Since the largest isotopic difference between the TES profiles near Hawaii occurs between approximately 3 and 5 mmol/mol (Figure 5.5), the precipitation efficiency of all TES profiles is characterized using the mean  $\delta D$  value of this humidity range. (For most profiles this involves only one data point.) Near Hawaii, 3-5 mmol/mol corresponds to the lower free troposphere ( $\sim 750$ -650 hPa, Figure 5.4). Therefore, for brevity's sake, the analysis refers to the associated  $\delta D$  value as  $\delta D_{LFT}$ .

An intercomparison of TES profiles under various cloud conditions provides additional justification for this choice. Figure 5.6 shows boxplots of  $\delta D_{LFT}$  for TES profiles associated with clear sky, non-precipitating cloud, and precipitating cloud. As explained in Section 2.1 of this chapter, an effective cloud optical depth less than 0.2 is used to define the clear-sky profiles. Non-precipitating and precipitating clouds are defined using the same International Satellite Cloud Climatology Project classifications as *Lee et al.* [2011]: non-precipitating cloudy conditions are those in which the optical depth exceeds 0.2 but is less than 3.6, while

precipitating cloudy conditions are those in which the optical depth exceeds 3.6. In both cases, the cloud top pressure is required to exceed 680 hPa so that the focus of the analysis is on low-level clouds. As Figure 5.6 demonstrates, in all four study regions, the median  $\delta D_{LFT}$  is lower under precipitating conditions than under non-precipitating conditions—a finding that is consistent with the prediction that higher precipitation efficiency convection should result in a lower  $\delta D$  value in the 3-5 mmol/mol humidity range.

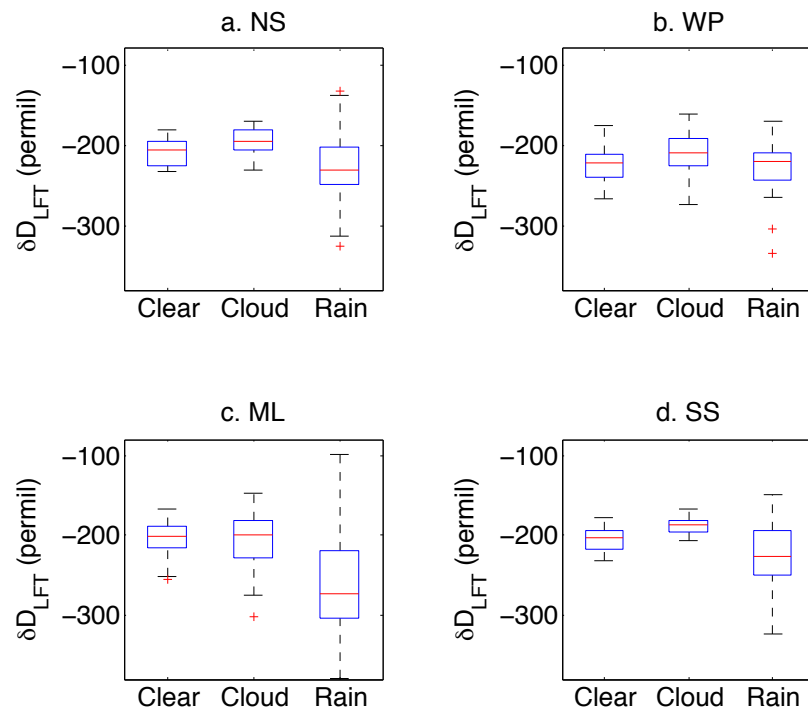


**Figure 5.6.** Distributions of the lower free tropospheric  $\delta D$  value ( $\delta D_{LFT}$ ) under clear sky (clear), non-precipitating cloud (cloud), and precipitating cloud (rain) in the four study regions: (a) the northern subtropics, (b) the mid-latitude storm track, (c) the western Pacific warm pool, and (d) the southern subtropics. Blue boxes mark the 25<sup>th</sup> ( $P_{25}$ ) and 75<sup>th</sup> ( $P_{75}$ ) percentiles, while red lines indicate the median. Whiskers extend to the most extreme points not considered outliers. Outliers are defined by  $P_{75}+1.5(P_{75}-P_{25})$  and  $P_{25}-1.5(P_{75}-P_{25})$ .

While the  $\delta D_{LFT}$  is used to characterize the precipitation efficiency of the study regions, a second metric, designed to capture the strength of mixing in the lower atmosphere, is also

considered as a possible correlate of low-level cloud cover. Since the isotope ratio will act as a conserved variable under mixing conditions [Bailey *et al.*, 2013], the isotopic profile should become more homogenous as mixing strengthens. Berkelhammer *et al.* [2012] provide additional evidence for this claim: they showed that as mixing strengthens during the buildup of the Madden Julian Oscillation (MJO)—a mesoscale convective feature known to drive intraseasonal variability in the tropics—the isotopic vertical gradient relaxes. They defined their vertical gradient by pairing TES free tropospheric retrievals with SCIAMACHY  $\delta D$  estimates for the boundary layer. When mixing and shallow convective detrainment during MJO increased, a smaller absolute  $\delta D$  difference with height was observed. This analysis defines a similar  $\delta D$  gradient by subtracting the TES  $\delta D$  estimate at 825 hPa from the estimate at 680 hPa. Thus, the more negative the gradient (the larger the absolute difference), the less active mixing is assumed to be.

Figure 5.7 shows  $5^\circ \times 5^\circ$  averages of the  $\delta D$  gradient and  $\delta D_{LFT}$  for the period 22 August 2004 through the end of 2012, with low-cloud fraction derived from MODIS averaged to the same grid in panel c. While the tropical warm pool region and the northern reaches of the mid-latitude storm track region exhibit the least negative gradients in  $\delta D$ , indicating the most mixing, the subtropical regions exhibit the most negative gradients. These negative gradients likely reflect the juxtaposition of a very dry free troposphere and moist tropical boundary layer, which is characteristic of trade wind regimes. In comparison, while the  $\delta D_{LFT}$  lies between -170 and -220 permil in most grid boxes, it is noticeably lower between  $0^\circ$  and  $10^\circ N$  in the warm pool region. Low-cloud fraction, meanwhile, tends to increase to the east in the subtropics, as one might expect with the transition from trade wind cumulus to stratocumulus; decrease to the north in the warm pool region, away from the ITCZ; and increase to the north in the mid-latitudes.

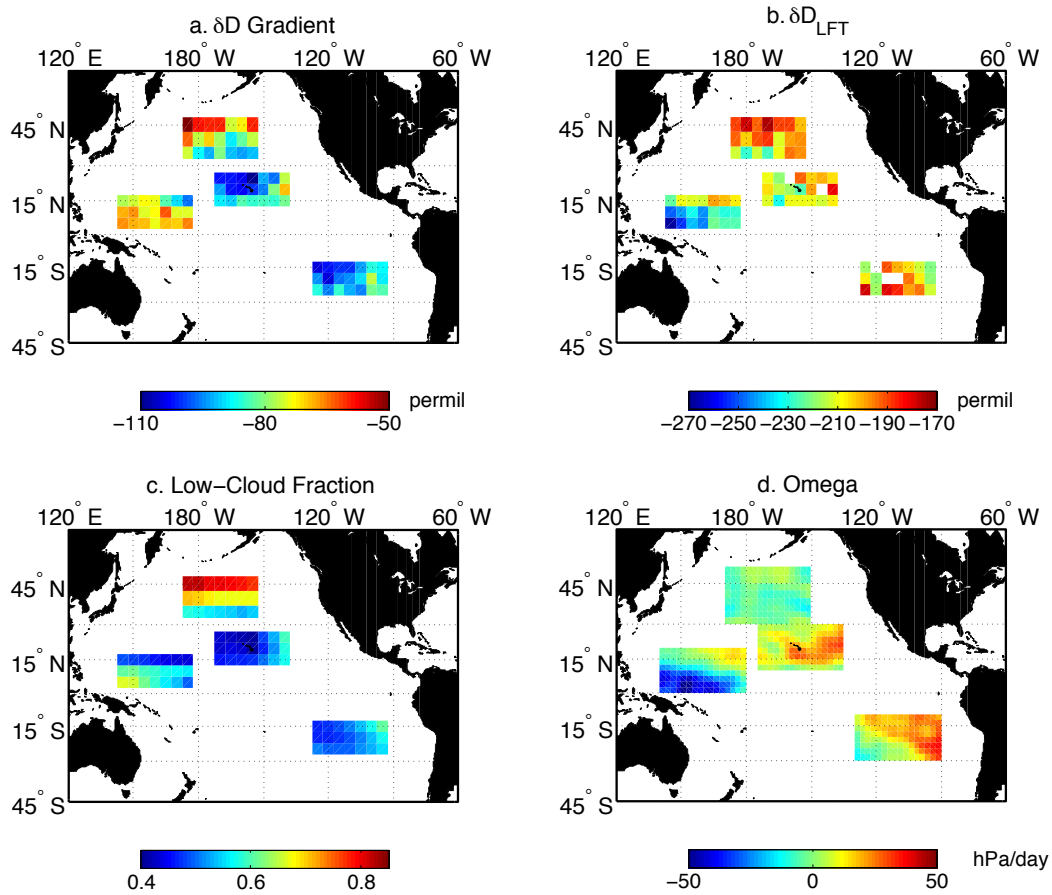


**Figure 5.7.** (a) The mean TES  $\delta D$  difference between 825 hPa and 680 hPa, (b) the mean TES  $\delta D$  value of the lower free troposphere ( $\delta D_{LFT}$ ), (c) the mean fraction of low-level cloud (cloud top > 680 hPa) from MODIS, and (d) the mean 700-hPa vertical pressure velocity (omega) from the NCEP-NCAR Reanalysis. The isotope ratios and cloud fraction are shown for the period 22 August 2004 through 2012 and are mapped to a  $5^\circ \times 5^\circ$  grid across the four study regions, while the vertical velocity is shown for the period 2004-2012 and mapped to the native NCEP-NCAR Reanalysis  $2.5^\circ \times 2.5^\circ$  grid.

Initially, these geographic patterns suggest the  $\delta D$  gradient correlates more strongly with low-cloud fraction (Figure 5.8) than  $\delta D_{LFT}$  (Figure 5.9) across all four regions. Yet the relationship is not the one anticipated. Recall that the MLO data showed that when the precipitation efficiency is low, and convection resembles a mixing process, low-cloud fraction is also low, compared with high  $e$  days. However, Figure 5.8 suggests low-cloud cover increases as

mixing strengthens.

In contrast,  $\delta D_{LFT}$  appears to correlate poorly with low-cloud cover in all regions but the warm pool (Figure 5.9). There, the relationship between  $\delta D_{LFT}$  and low-cloud fraction is as expected: the lower the precipitation efficiency, the less low-level cloud. These findings suggest 1) that TES estimates of precipitation efficiency and mixing must capture distinct processes and 2) that variations in precipitation efficiency only correlate with low-cloud cover in regions typified by deep convection. As shown in Figure 5.7d, the warm pool is the only region studied in which the mean 700-hPa vertical pressure velocity reaches values lower than -20 hPa/day. We thus consider the possibility that the mean vertical velocity of a region influences the extent to which TES profiles are able to predict low-cloud fraction.

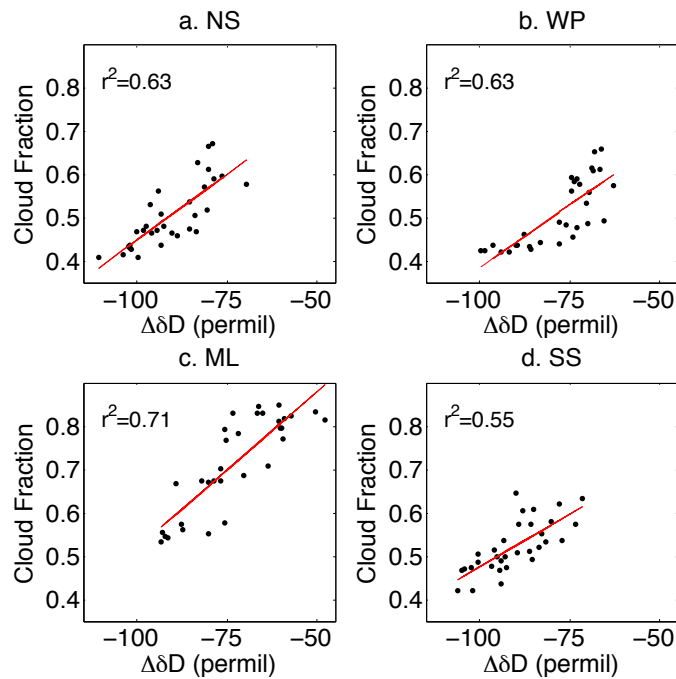


**Figure 5.8.** Low-level cloud fraction from MODIS versus the TES  $\delta D$  gradient across the four study regions: (a) the northern subtropics, (b) the mid-latitude storm track, (c) the western Pacific warm pool, and (d) the southern subtropics. Simple linear regressions are shown in red and the associated  $r^2$  values are listed on each panel.

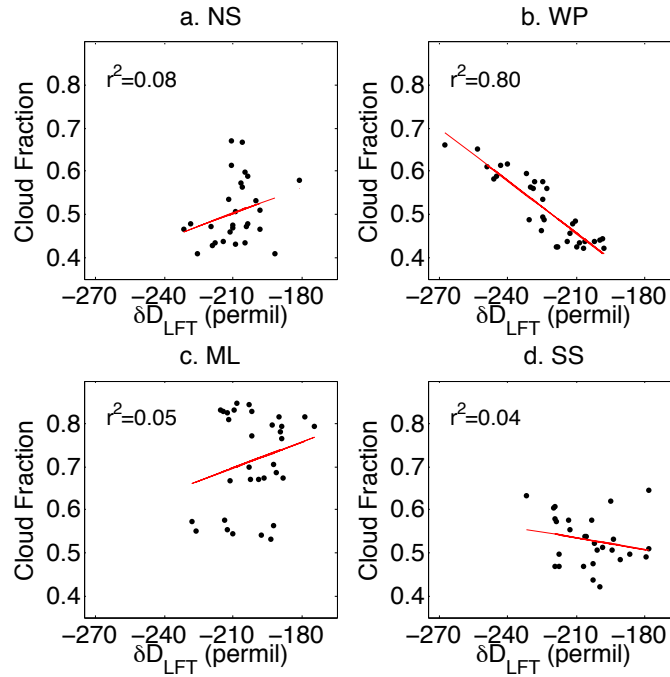


**Figure 5.9.** Low-level cloud fraction from MODIS versus the TES lower free tropospheric  $\delta D$  value ( $\delta D_{LFT}$ ) across the four study regions: (a) the northern subtropics, (b) the mid-latitude storm track, (c) the western Pacific warm pool, and (d) the southern subtropics. Simple linear regressions are shown in red and the associated  $r^2$  values are listed on each panel.

To determine whether the relationship between precipitation efficiency and low-cloud cover is sensitive to vertical ascent, convective periods are identified for each  $5^\circ \times 5^\circ$  grid box in the mid-latitude, northern subtropics, and southern subtropics regions. Using the higher resolution ECMWF Reanalysis ERA-Interim, days and grid boxes in which the mean vertical velocity is less than  $-20$  hPa/day are selected. Mean  $\delta D$  profiles and low-level cloud fraction are then recalculated for these convective periods, and the relationships between the  $\delta D$  gradient and cloud cover and  $\delta D_{LFT}$  and cloud cover are reassessed. The results are shown in Figures 5.10 and 5.11, respectively.

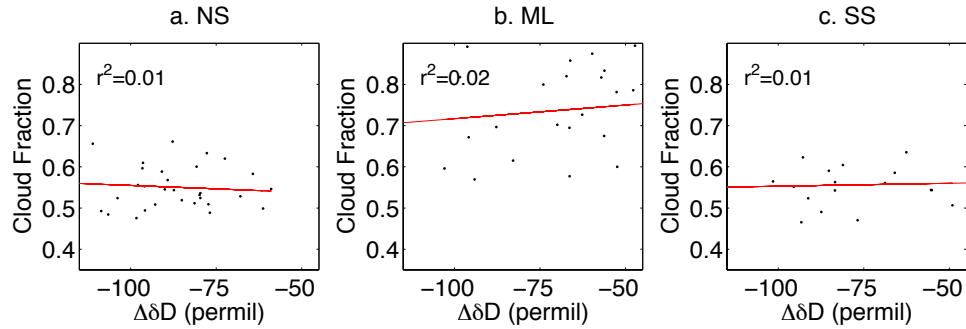


**Figure 5.10.** Low-level cloud fraction from MODIS versus the TES  $\delta D$  gradient for periods and grid boxes in which the mean daily vertical pressure velocity is less than  $-20$  hPa/day. Results are shown for three of the four study regions: (a) the northern subtropics, (b) the mid-latitude storm track, and (c) the southern subtropics. Simple linear regressions are shown in red and the associated  $r^2$  values are listed on each panel.

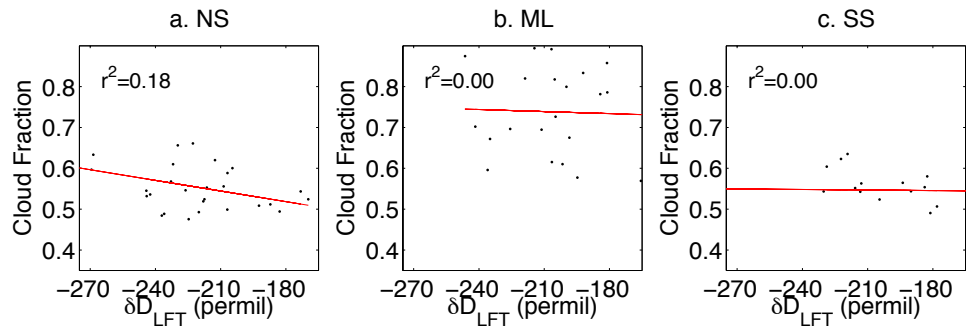


**Figure 5.11.** Low-level cloud fraction from MODIS versus the TES lower free tropospheric  $\delta D$  value ( $\delta D_{LFT}$ ) for periods and grid boxes in which the mean daily vertical pressure velocity is less than  $-20$  hPa/day. Results are shown for three of the four study regions: (a) the northern subtropics, (b) the mid-latitude storm track, and (c) the southern subtropics. Simple linear regressions are shown in red and the associated  $r^2$  values are listed on each panel.

These figures demonstrate that once one accounts for the mean vertical velocity, the positive correlation between the  $\delta D$  gradient and low-cloud fraction disappears (Figure 5.10), which suggests the homogenization of the lower-tropospheric profile is actually an indicator of upward vertical motion. Since upward motion is present during both shallow and deep convection, it is not clear that this metric accurately represents the lower-tropospheric mixing

process described by *Sherwood et al.* [2014]. In contrast, the relationship between  $\delta D_{LFT}$  and low-cloud fraction changes little, except in the northern subtropics. There, the correlation becomes negative and more significant. The resulting relationship between precipitation efficiency and cloud cover is consistent both with expectation and with earlier observations of the warm pool region (Figure 5.9b). The new Pearson  $r$  value of -0.42, however, is still much lower than the warm pool value of -0.89, which indicates that precipitation efficiency is not as strongly correlated with low-cloud fraction outside of deep convective regions.

#### 4. Discussion

While some argue that reducing the precipitation efficiency ( $e$ ) decreases the amount of low-level cloud [*Sherwood et al.*, 2014], not all studies agree [*Zhao*, 2014]. This study finds evidence that higher  $e$  is associated with lower fractions of low-level cloud, but only in the western Pacific warm pool region. Interestingly, *Sherwood et al.* [2014] also demonstrated a link between lower-tropospheric mixing and cloudiness only in regions of mean ascent; however, they did not discuss whether this was because their metric for mixing was less robust in areas of large-scale subsidence.

The fact that the isotopic metric highlighted in this research works best in broadly ascending regions may not be particularly surprising. After all, isotopic models of precipitation efficiency assume that the modeled air masses undergo moist adiabatic convection [*Dansgaard*, 1964; *Jouzel and Merlivat*, 1984; *Noone*, 2012; *Bailey et al.*, 2013]. Variations in  $\delta D_{LFT}$  in areas of large-scale subsidence, meanwhile, may simply reflect variations in the isotopic values of the boundary layer and free troposphere. For example, if the free troposphere is moister and the

boundary layer more depleted than on average, vertical mixing between such air masses will reduce the  $\delta D_{LFT}$  even under non-precipitating conditions.

Although TES failed to detect a strong relationship between precipitation efficiency and cloud cover in the subtropics, ground-based instrumentation did identify differences in cloudiness for high and low precipitation efficiency events near Hawaii. There are at least two possible explanations for these divergent findings. The first may be related to the fact that strong convection appears to be a necessary criterion for linking precipitation efficiency and low-cloud cover. Since daytime heating of the Hawaiian landmass amplifies local boundary-layer growth, and since the ground-based observations were used to classify high and low  $e$  days near Hawaii during strong convection only, the average daytime vertical velocity for these events was almost assuredly negative. In comparison, estimates of mean vertical ascent from the comparatively low-resolution NCEP-NCAR Reanalysis may not have represented the atmospheric columns profiled by TES as accurately as desired. In addition, the synoptic-scale systems that form convective features like atmospheric rivers are less common in the southeast Pacific than in the northern subtropics near Hawaii [Zhu and Newell, 1998], which may explain why the southern subtropics failed to exhibit a measureable correlation between  $e$  and cloudiness, even after controlling for mean vertical ascent. Second, Chapter 4 defined high and low  $e$  days using only the tails of the observational data distribution, while TES estimates of precipitation efficiency were calculated along a continuum; therefore the latter may not have distinguished high and low  $e$  as precisely. Notably, were only the more extreme of the TES  $\delta D_{LFT}$  considered, the variance in cloud fraction explained would be much higher for the northern subtropics, since most of the residual error appears associated with the center of the  $\delta D$  distribution (Figure 5.11a).

This analysis also considered whether the  $\delta D$  gradient of the lower atmosphere might

characterize mixing processes and serve as yet another indicator of low-cloud fraction. At first, the gradient appeared positively correlated with low-cloud fraction; however, this correlation vanished once mean vertical ascent was controlled for, implying that a relaxed  $\delta D$  gradient, in effect, reflects strong convective activity. Since stronger convection will enhance the vertical moisture fluxes necessary to sustain low-cloud fields, this could explain the positive correlation initially observed between the  $\delta D$  gradient and low-level cloudiness.

## 5. Conclusion

This chapter has examined the link between precipitation efficiency and low-cloud cover from an observational perspective using both ground-based and satellite measurements of the heavy-to-light isotope ratio in water vapor. The ground-based measurements indicated a positive relationship between precipitation efficiency and cloud cover near Hawaii, which was amplified when the total-column cloud cover was considered. These findings suggest that as cloud evaporation is favored over precipitation, the magnitude of the shortwave cloud forcing is reduced, and more sunlight reaches and warms Earth's surface.

Remote-sensing observations similarly identified a positive relationship between precipitation efficiency and low-cloud cover, but only in the western Pacific warm pool region. There, the strong correlation between the lower free tropospheric  $\delta D$  value ( $\delta D_{LFT}$ ) and low-cloud fraction suggests that this isotopic metric could readily serve as a diagnostic of low-cloud variations in regions of mean vertical ascent. Remotely sensed observations of  $\delta D_{LFT}$  might also serve as an independent evaluation of *Sherwood et al.* [2014]'s hypothesis that inter-model variations in precipitation efficiency—caused by variations in lower-tropospheric mixing—

create the large spread in climate model sensitivity. With several isotopically-enabled models currently in use or development [e.g. *Risi et al.*, 2012], a robust isotopic indicator of low-cloud cover—that can be verified with observations—would provide a powerful tool for fine-tuning model predictions of future climate.

## CHAPTER VI

### Conclusion

Using a novel atmospheric tracer—*isotope ratios in water vapor*—this thesis has evaluated how shallow convective mixing and precipitation processes influence cloud cover and vertical distributions of atmospheric constituents important for climate. Beginning with a case study, it was shown that isotopic tracers successfully model mixing between the boundary layer and free troposphere while identifying residual layers that modify the exchange of material in the vertical. Subsequent research characterized important biases and verified the long-term stability of new commercial isotopic measurements, lending confidence to new multi-year analyses. A three-year data set was then used to identify more than 1,000 strong convective events near Hawaii and characterize their precipitation efficiency—the efficiency with which cloud condensate is converted to precipitation. A clear link was made not only between the precipitation efficiency of convection and large-scale circulation, but also between precipitation processes and vertical distributions of atmospheric tracers. Finally, the effects of vertical mixing and precipitation efficiency on cloud fields were also investigated. A positive correlation was demonstrated between precipitation efficiency—as derived from satellite—and low-level cloud cover in regions of mean vertical ascent. Since low-level clouds continue to contribute large uncertainties to our understanding of climate [*Bony and Dufresne, 2005*], identifying metrics that can serve as diagnostics for low-cloud cover may prove particularly useful for improving model simulations of future change.

Although many tracers are capable of tracking large-scale transport pathways and airmass mixing, it was shown that isotope ratios in water vapor exhibit a dynamic range at low humidity

that more traditional tracers like ozone typically lack. Moreover, as a result of their sensitivity to water phase changes, isotopic tracers proved capable of distinguishing microphysical differences between convective events. By exploiting this unique attribute, the analysis identified two very distinct circulation patterns associated with strong convection near Hawaii, which water vapor measurements alone would have failed to detect. In addition, it was found that though mixing processes near Hawaii primarily influence vertical distributions of particle number concentration on low precipitation efficiency days, precipitation processes likely play a role in scavenging pre-existing aerosol and facilitating new particle formation when the precipitation efficiency is high.

Importantly, not only are isotopic tracers well suited for studying mixing and microphysical processes associated with convection, but also the technology to measure them is steadily improving and expanding. Field-deployable laser absorption instruments such as the Picarro analyzer, which only became commercially available in the last five years, continue to demonstrate reduced measurement biases and improved long-term precision with each new model version. These analyzers are thus creating numerous opportunities to study hydrological processes and their feedbacks on climate, albeit typically from a fixed point. (Airborne platforms, of course, allow sampling over a larger domain.) Meanwhile, satellite retrievals have created new opportunities to characterize isotope ratios over much larger geographic expanses. While the resolution of these measurements is still coarse, recent improvements in the vertical retrieval of NASA's Tropospheric Emission Spectrometer [*Worden et al.*, 2012] have increased their information content in the lower atmosphere, making it possible to evaluate key hypotheses about shallow convective mixing processes.

With expanding networks of satellite and ground-based isotopic instrumentation, a promising way forward for future research is to use the link between precipitation efficiency and

low-cloud cover to evaluate general circulation models and investigate cloud feedbacks on climate. Several well-known models now include isotopic tracers, including the National Center for Atmospheric Research's and the Goddard Institute for Space Studies'. Specifically, by comparing observed correlations between precipitation efficiency and low-cloud cover with those simulated, one might verify whether these models accurately capture key relationships between convection and clouds. The model environment would also provide the opportunity to study how variations in low-cloud cover influence shortwave cloud radiative forcing. In this manner, it would be possible to investigate how changes in the balance of cloud detrainment and precipitation influence cloud feedbacks and climate sensitivity. Ultimately, identifying which climate sensitivity is most representative of the Earth system is critical for narrowing the range of predicted future global temperatures. This thesis brings us one step closer to this goal by demonstrating a new observational approach for studying how convective mixing and microphysical processes influence spatiotemporal distributions of water vapor, aerosol, and low-level clouds.

## BIBLIOGRAPHY

- Aemisegger, F., P. Sturm, P. Graf, H. Sodemann, S. Pfahl, A. Knohl, and H. Wernli (2012), Measuring variations of  $\delta^{18}\text{O}$  and  $\delta^2\text{H}$  in atmospheric water vapour using two commercial laser-based spectrometers: an instrument characterisation study, *Atmos. Meas. Tech.*, *5*, 1491-1511.
- Aemisegger, F., S. Pfahl, H. Sodemann, I. Lehner, S. I. Seneviratne, and H. Wernli (2014), Deuterium excess as a proxy for continental moisture recycling and plant transpiration, *Atmos. Chem. Phys.*, *14*, 4029-4054, doi:10.5194/acp-14-4029-2014.
- Albrecht, B. (1989), Aerosols, cloud microphysics, and fractional cloudiness, *Science*, *245*, 1227–1230.
- Albrecht, B. A., A. K. Betts, W. H. Schubert, and S. K. Cox (1979), Model of the thermodynamic structure of the trade-wind boundary layer: Part I. Theoretical formulation and sensitivity tests, *J. Atmos. Sci.*, *36*, 73–89.
- Amante, C. and B. W. Eakins (2009), ETOPO1 1 Arc-Minute Global Relief Model: Procedures, Data Sources and Analysis, NOAA Technical Memorandum NESDIS NGDC-24, 19 pg.
- Ayotte, K. W., P. P. Sullivan, A. Andr n, S. C. Doney, A. A. M. Holslag, W. G. Large, J. C. McWilliams, C.-H. Moeng, M. J. Otte, J. J. Tribbia, and J. C. Wyngaard (1996), An evaluation of neutral and convective planetary boundary-layer parameterizations relative to large eddy simulations, *Boundary-Layer Metereol.*, *79*, 131-175.
- Bailey, A., D. Toohey, and D. Noone (2013), Characterizing moisture exchange between the Hawaiian convective boundary layer and free troposphere using stable isotopes in water, *J. Geophys. Res.*, *118*, 8208-8221, doi:10.1002/jgrd.50639.
- Barth, M. C., P. G. Hess, and S. Madronich (2002), Effect of marine boundary layer clouds on tropospheric chemistry as analyzed in a regional chemistry transport model, *J. Geophys. Res.*, *107*, AAC 7-1 – AAC 7-12, doi:10.1029.2001JD000468.
- Berkelhammer, M., C. Risi, N. Kurita, and D. C. Noone (2012), The moisture source sequence for the Madden-Julian Oscillation as derived from satellite retrievals of HDO and H<sub>2</sub>O, *J. Geophys. Res.*, *117*, D03106, doi:10.1029.2011JD016803.
- Berkelhammer, M., J. Hu, A. Bailey, D. Noone, C. Still, H. Barnard, D. Gochis, G. Hsiao, T. Rahn, and A. Turnipseed (2013), The nocturnal water cycle in an open-canopy forest, *J. Geophys. Res.*, *118*, 10225-10242, doi:10.1002/jgrd.50701.
- Betts, A. K. and B. A. Albrecht (1987), Conserved variable analysis of the convective boundary layer thermodynamic structure over the tropical oceans, *J. Atmos. Sci.*, *44*, 83–99.

- Bigeleisen, J. (1961), Statistical mechanics of isotope effects on the thermodynamic properties of condensed systems, *J. Chem. Phys.*, *34*, 1485-1493.
- Blossey, P. N., Z. Kuang, and D. M. Romps (2010), Isotopic composition of water in the tropical tropopause layer in cloud-resolving simulations of an idealized tropical circulation, *J. Geophys. Res.*, *115*, D24309 doi:10.1029/2010JD014554.
- Bodhaine, B. A. (1996), Aerosol measurements during the Mauna Loa Photochemistry Experiment 2, *J. Geophys. Res.*, *101*, 14,757-14,765, doi:10.1029/95JD02045.
- Bony, S., and J.-L. Dufresne (2005), Marine boundary layer clouds at the heart of tropical cloud feedback uncertainties in climate models, *Geophys. Res. Lett.*, *32*, L20806, doi:10.1029/2005GL023851.
- Bony, S., C. Risi, and F. Vimeux (2008), Influence of convective processes on the isotopic composition (d18O and dD) of precipitation and water vapor in the tropics: 1. Radiative-convective equilibrium and Tropical Ocean-Global Atmosphere-Coupled Ocean-Atmosphere Response Experiment (TOGA-COARE) simulations, *J. Geophys. Res.*, *113*, D19305 doi:10.1029/2008JD009942.
- Boucher, O., D. Randall, P. Artaxo, C. Bretherton, G. Feingold, P. Forster, V.-M. Kerminen, Y. Kondo, H. Liao, U. Lohmann, P. Rasch, S. K. Satheesh, S. Sherwood, B. Stevens and X. Y. Zhang (2013), Clouds and aerosols, in *Climate Change 2013: The Physical Science Basis. Contribution of Working Group I to the Fifth Assessment Report of the Intergovernmental Panel on Climate Change*, edited by T.F. Stocker et al., pp. 571-657, Cambridge Univ. Press, Cambridge and New York.
- Bretherton, C. S., P. Austin, and S. T. Siems (1995), Cloudiness and marine boundary layer dynamics in the ASTEX Lagrangian experiments: Cloudiness, drizzle, surface fluxes, and entrainment, *J. Atmos. Sci.*, *52*, 2724-2735.
- Brient, F., and S. Bony (2013), Interpretation of the positive low-cloud feedback predicted by a climate model under global warming, *Clim. Dyn.*, *40*, 2415-2431, doi:10.1007/s00382-011-1279-7.
- Brooks I. M. and A. M. Fowler (2012), An evaluation of boundary-layer depth, inversion and entrainment parameters by large-eddy simulation, *Boundary-Layer Meteorol.*, *142*, 245-263, doi:10.1007/s10546-011-9668-3.
- Brown, D., J. Worden, and D. Noone (2008), Comparison of atmospheric hydrology over convective continental regions using water vapor isotope measurements from space, *J. Geophys. Res.*, *113*, D15124, doi:10.1029/2007JD009676.
- Brown, D., J. Worden, and D. Noone (2013), Characteristics of tropical and subtropical atmospheric moistening derived from Lagrangian mass balance constrained by measurements of HDO and H2O, *J. Geophys. Res.*, *118*, 54-72,

doi:10.1029/2012JD018507.

- Cai, Y., D. C. Montague, W. Mooiweer-Bryan, and T. Deshler (2008), Performance characteristics of the ultra high sensitivity aerosol spectrometer for particles between 55 and 800 nm: Laboratory and field studies, *J. Aerosol Sci.*, *39*, 750-769.
- Cao, G., T. W. Giambelluca, D. E. Stevens, and T. A. Schroeder (2007), Inversion variability in the Hawaiian trade wind regime, *J. Climate*, *20*, 1145-1160.
- Cau, P., J. Methven, and B. Hoskins (2007), Origins of dry air in the tropics and subtropics, *J. Climate*, *20*, 2745–2759, doi: <http://dx.doi.org/10.1175/JCLI4176.1>.
- Chen, G., H. Xue, G. Feingold, and X. Zhou (2012), Vertical transport of pollutants by shallow cumuli from large eddy simulations, *Atmos. Chem. Phys.*, *12*, 11319-11327, doi:10.5194/acp-12-11319-2012.
- Clarke, A. D. (1993), Atmospheric nuclei in the Pacific midtroposphere: Their nature, concentration, and evolution, *J. Geophys. Res.*, *98*, 20,633-20,647.
- Coplen, T.B. (1994), Reporting of stable hydrogen, carbon, and oxygen isotopic abundances, *Pure Appl. Chem.*, *66*, 273-276.
- Cotton, W. R., G. D. Alexander, R. Hertenstein, R. L. Walko, R. L. M McAnelly, and M. Nicholls (1995), Cloud venting—A review and some new global annual estimates, *Earth Sci. Rev.*, *39*, 169-206.
- Craig, H. (1961), Isotopic variations in meteoric waters, *Science*, *133*, 1702-1703.
- Dansgaard, W. (1964), Stable isotopes in precipitation, *Tellus*, *16*, 436-468.
- Deardorff, J. W., G. E. Willis, and B. H. Stockton (1980), Laboratory studies of the entrainment zone of a convectively mixed layer, *J. Fluid Mech.*, *100*, 41-64, doi:10.1017/S0022112080001000.
- DeMaria, M. and J. Kaplan (1994), A Statistical Hurricane Intensity Prediction Scheme (SHIPS) for the Atlantic Basin, *Wea. Forecasting*, *9*, 209–220, doi: [http://dx.doi.org/10.1175/1520-0434\(1994\)009<0209:ASHIPS>2.0.CO;2](http://dx.doi.org/10.1175/1520-0434(1994)009<0209:ASHIPS>2.0.CO;2).
- Dettinger M. D., F. M. Ralph, T. Das, P. J. Neiman, and D. R. Cayan (2011), Atmospheric rivers, floods and the water resources of California, *Water*, *3*, 445-478, doi:10.3390/w3020445.
- Dlugokencky, E. J., A. M. Crotwell, P. M. Lang, and K. A. Masarie (2014), Atmospheric methane dry air mole fractions from quasi-continuous measurements at Barrow, Alaska and Mauna Loa, Hawaii, Version: 2014-08-12, October 2010 to September 2013, Natl. Oceanic and Atmos. Admin., Earth Systems Res. Lab. Global Monitoring Division, Boulder, Colo.

- Ehhalt, D. H. (1974), Vertical profiles of HTO, HDO, and H<sub>2</sub>O in the troposphere, NCAR Tech. Note NCAR–TN/STR–100, 131 pp., Natl. Cent. for Atmos. Res., Boulder, Colo.
- Faloona, I., D. H. Lenschow, T. Campos, B. Stevens, M. van Zanten, B. Blomquist, D. Thornton, A. Bandy, and H. Gerber (2005), Observations of entrainment in eastern Pacific marine stratocumulus using three conserved scalars, *J. Atmos. Sci.*, *62*, 3268–3285, doi: <http://dx.doi.org/10.1175/JAS3541.1>.
- Ferrier, B. S., J. Simpson, and W.-K. Tao (1996), Factors responsible for precipitation efficiencies in midlatitude and tropical squall simulations, *Mon. Wea. Rev.*, *124*, 2100–2125, doi: [http://dx.doi.org/10.1175/1520-0493\(1996\)124<2100:FRFPEI>2.0.CO;2](http://dx.doi.org/10.1175/1520-0493(1996)124<2100:FRFPEI>2.0.CO;2).
- Flato, G., J. Marotzke, B. Abiodun, P. Braconnot, S.C. Chou, W. Collins, P. Cox, F. Driouech, S. Emori, V. Eyring, C. Forest, P. Gleckler, E. Guilyardi, C. Jakob, V. Kattsov, C. Reason and M. Rummukainen (2013), Evaluation of climate models, in *Climate Change 2013: The Physical Science Basis. Contribution of Working Group I to the Fifth Assessment Report of the Intergovernmental Panel on Climate Change*, edited by T.F. Stocker et al., pp. 571-657, Cambridge Univ. Press, Cambridge and New York.
- Folkens, I., P. Bernath, C. Boone, L. J. Donner, A. Eldering, G. Lesins, R. V. Martin, B.-M. Sinnhuber, and K. Walker (2006), Testing convective parameterizations with tropical measurements of HNO<sub>3</sub>, CO, H<sub>2</sub>O, and O<sub>3</sub>: Implications for the water vapor budget, *J. Geophys. Res.*, *111*, D23304, doi:10.1029/2006JD007325.
- Galewsky, J., M. Strong, and Z. D. Sharp (2007), Measurements of water vapor D/H ratios from Mauna Kea, Hawaii, and implications for subtropical humidity dynamics, *Geophys. Res. Lett.*, *34*, L22808, doi:10.1029/2007GL031330.
- Galewsky, J., C. Rella, Z. Sharp, K. Samuels, and D. Ward (2011), Surface measurements of upper tropospheric water vapor isotopic composition on the Chajnantor Plateau, Chile, *Geophys. Res. Lett.*, *38*, L17803, doi:10.1029/2011GL048557.
- Garrett, A. J. (1980), Orographic cloud over the eastern slopes of Mauna Loa volcano, Hawaii, related to insolation and wind. *Mon. Weather Rev.*, *108*, 931-941.
- Gat, J. R. (1996), Oxygen and hydrogen isotopes in the hydrologic cycle, *Annu. Rev. Earth Planet. Sci.*, *24*, 225-262.
- Gedzelman, S. D. (1988), Deuterium in water vapor above the atmospheric boundary layer, *Tellus*, *40B*, 134-147.
- Gröning, M. (2011), Improved water  $\delta^2\text{H}$  and  $\delta^{18}\text{O}$  calibration and calculation of measurement uncertainty using a simple software tool, *Rapid Commun. Mass Spectrom.*, *25*, 2711-2720, doi:10.1002/rcm.5074.

- Gupta, P., D. Noone, J. Galewsky, C. Sweeney, and B. H. Vaughn (2009), Demonstration of high-precision continuous measurements of water vapor isotopologues in laboratory and remote field deployments using wavelength-scanned cavity ring-down spectroscopy (WS-CRDS) technology, *Rapid Commun. Mass Spectrom.*, *23*, 2534-2542.
- Harris, J. M., and J. D. Kahl (1990), A descriptive atmospheric transport climatology for the Mauna Loa Observatory, using clustered trajectories, *J. Geophys. Res.*, *95*(D9), 13651–13667, doi:10.1029/JD095iD09p13651.
- Harris, J. M., P. P. Tans, E. J. Dlugokencky, K. A. Masarie, P. M. Lang, S. Whittlestone, and L. P. Steele (1992), Variations in atmospheric methane at Mauna Loa Observatory related to long-range transport, *J. Geophys. Res.*, *97*(D5), 6003–6010, doi:10.1029/92JD00158.
- He, H. and R. B. Smith (1999), Stable isotope composition of water vapor in the atmospheric boundary layer above the forests of New England, *J. Geophys. Res.*, *104*, 11657–11673.
- Hegg, D. A., L. F. Radke, and P. V. Hobbs (1990), Particle production associated with marine clouds, *J. Geophys. Res.*, *95*, 13,917-13,926.
- Held, I. M., and B. J. Soden (2000), Water vapor feedback and global warming, *Annu. Rev. Energy Env.*, *25*, 441-475, doi:10.1146/annurev.energy.25.1.441.
- Herman, R. L., J. E. Cherry, J. Young, J. M. Welker, D. Noone, S. S. Kulawik, and J. Worden (2014), Aircraft validation of Aura Tropospheric Emission Spectrometer retrievals of HDO / H<sub>2</sub>O, *Atmos. Meas. Tech.*, *7*, 3127-3138, doi:10.5194/amt-7-3127-2014.
- Hoppel, W. A., G. M. Frick, and R. E. Larson (1986), Effect of nonprecipitating clouds on the aerosol size distribution in the marine boundary layer, *Geophys. Res. Lett.*, *13*, 125-128, doi:10.1029/GL013i002p00125.
- Hu, X.-M., J. W. Nielsen-Gammon, and F. Zhang (2010), Evaluation of three planetary boundary layer schemes in the WRF model, *J. Appl. Meteor. Climatol.*, *49*, 1831–1844.
- Hurley, J. V., J. Galewsky, J. Worden, and D. Noone (2012): A test of the advection-condensation model for subtropical water vapor using stable isotopologue observations from Mauna Loa Observatory, Hawaii, *J. Geophys. Res.*, *117*, D19118, doi:10.1029/2012JD018029.
- Johnson, L. R., Z. D. Sharp, J. Galewsky, M. Strong, A. D. Van Pelt, F. Dong, and D. Noone (2011), Hydrogen isotope correction for laser instrument measurement bias at low water vapor concentration using conventional isotope analyses: application to measurements from Mauna Loa Observatory, Hawaii, *Rapid Commun. Mass Spectrom.*, *25*, 608-616.
- Jouzel, J. and L. Merlivat (1984), Deuterium and oxygen 18 in precipitation: Modeling of the isotopic effects during snow formation. *J. Geophys. Res.*, *89*, 11749-11757.

- Kaufman, Y. J., A. Smirnov, B. N. Holben, and O. Dubovik (2001), Baseline maritime aerosol: methodology to derive the optical thickness and scattering properties, *Geophys. Res. Lett.*, *28*, 3251-3254.
- Laird, N. F. (2005), Humidity halos surrounding small cumulus clouds in a tropical environment, *J. Atmos. Sci.*, *62*, 3420-3425.
- Lau, K. M., and H. T. Wu (2003), Warm rain processes over tropical oceans and climate implications, *Geophys. Res. Lett.*, *30*, 2290, doi:10.1029/2003GL018567, 24.
- Lee, J., J. Worden, D. Noone, K. Bowman, A. Eldering, A. LeGrande, J.-L. F. Li, G. Schmidt, and H. Sodemann (2011), Relating tropical ocean clouds to moist processes using water vapor isotope measurements, *Atmos. Chem. Phys.*, *11*, 741-752, doi:10.5194/acp-11-741-2011.
- LeGrande, A. N., and G. A. Schmidt (2009), Sources of Holocene variability of oxygen isotopes in paleoclimate archives, *Clim. Past*, *5*, 441-455.
- Lenschow, D. H., P. B. Krummel, and S. T. Siems (1999), Measuring entrainment, divergence, and vorticity on the mesoscale from aircraft, *J. Atmos. Oceanic Technol.*, *16*, 1384-1400.
- Leopold, L. B. (1949), The interaction of trade wind and sea breeze, Hawaii, *J. Meteorol.*, *6*, 312-320.
- Leung, L. R., and Y. Qian (2009), Atmospheric rivers induced heavy precipitation and flooding in the western U.S. simulated by the WRF regional climate model, *Geophys. Res. Lett.*, *36*, L03820, doi:10.1029/2008GL036445.
- Lin, M., L. W. Horowitz, S. J. Oltmans, A. M. Fiore, and S. Fan (2014), Tropospheric ozone trends at Mauna Loa Observatory tied to decadal climate variability, *Nature Geosci.*, *7*, 136-143, doi:10.1038/ngeo2066.
- Lis, G., L. I. Wassenaar, and M. J. Hendry (2008), High-precision laser spectroscopy D/H and  $^{18}\text{O}/^{16}\text{O}$  measurements of microliter natural water samples, *Anal. Chem.*, *80*, 287-293, doi:10.1021/ac701716q.
- Lu, M.-L., J. Wang, A. Freedman, H. H. Jonsson, R. C. Flagan, P. A. McClatchey, and J. H. Seinfeld (2003), Humidity halos around trade wind cumulus clouds, *J. Atmos. Sci.*, *60*, 1041-1059.
- McClure-Begley, A., I. Petropavlovskikh, and S. Oltmans (2014), NOAA Global Monitoring Surface Ozone Network, October 2010 to September 2013, Natl. Oceanic and Atmos. Admin., Earth Systems Res. Lab. Global Monitoring Division, Boulder, Colo, <http://dx.doi.org/10.7289/>.
- Mendonca, B. G. and W. T. Iwaoka (1969), The trade wind inversion at the slopes of Mauna

- Loa, Hawaii, *J. Appl. Meteorol.*, 8, 213-219.
- Merrill, J. T., M. Uematsu, and R. Bleck (1989), Meteorological analysis of long range transport of mineral aerosols over the North Pacific, *J. Geophys. Res.*, 94(D6), 8584–8598, doi:10.1029/JD094iD06p08584.
- Myhre, G., D. Shindell, F.-M. Bréon, W. Collins, J. Fuglestedt, J. Huang, D. Koch, J.-F. Lamarque, D. Lee, B. Mendoza, T. Nakajima, A. Robock, G. Stephens, T. Takemura, and H. Zhang (2013), Anthropogenic and natural radiative forcing, in *Climate Change 2013: The Physical Science Basis. Contribution of Working Group I to the Fifth Assessment Report of the Intergovernmental Panel on Climate Change*, edited by T.F. Stocker et al., pp. 659-740, Cambridge Univ. Press, Cambridge and New York.
- Nassar, R., P. F. Bernath, C. D. Boone, A. Gettelman, S. D. McLeod, and C. P. Rinsland (2007), Variability in HDO/H<sub>2</sub>O abundance ratios in the tropical tropopause layer, *J. Geophys. Res.*, 112, D21305 doi:10.1029/2007JD008417.
- Neiman, P. J., F. M. Ralph, G. A. Wick, J. D. Lundquist, and M. D. Dettinger (2008), Meteorological characteristics and overland precipitation impacts of atmospheric rivers affecting the west coast of North America based on eight years of SSM/I satellite observations, *J. Hydrometeorol.*, 9, 22–47, doi: <http://dx.doi.org/10.1175/2007JHM855.1>.
- Nelson, E., R. Stull, and E. Eloranta (1989), A prognostic relationship for entrainment zone thickness, *J. Appl. Meteor.*, 28, 885–903.
- Nilsson, E. D., Ü. Rannik, M. Kulmala, G. Buzorius, and C. D. O’Dowd (2001), Effects of continental boundary layer evolution, convection, turbulence, and entrainment, on aerosol formation, *Tellus B*, 53, 441-461, doi:10.1034/j.1600-0889.2001.530409.x.
- Noone, D., J. Galewsky, Z. D. Sharp, J. Worden, J. Barnes, D. Baer, A. Bailey, D. P. Brown, L. Christensen, E. Crosson, F. Dong, J. V. Hurley, L. R. Johnson, M. Strong, D. Toohey, A. Van Pelt, and J. S. Wright (2011), Properties of air mass mixing and humidity in the subtropics from measurements of the D/H isotope ratio of water vapor at the Mauna Loa Observatory, *J. Geophys. Res.*, 116, doi:10.1029/2011JD015773.
- Noone, D. (2012), Pairing measurements of the water vapor isotope ratio with humidity to deduce atmospheric moistening and dehydration in the tropical midtroposphere, *J. Climate*, 25, 4476–4494.
- Noone, D., C., Risi, A. Bailey, M. Berkelhammer, D. P. Brown, N. Buening, S. Gregory, J. Nusbaumer, D. Schneider, J. Sykes, B. Vanderwende, J. Wong, Y. Meillier, and D. Wolfe (2013), Determining water sources in the boundary layer from tall tower profiles of water vapor and surface water isotope ratios after a snowstorm in Colorado, *Atmos. Chem. Phys.*, 13, 1607-1623.
- Oltmans, S. J., D. J. Hofmann, J. A. Lathrop, J. M. Harris, W. D. Komhyr, and D. Kuniyuki

- (1996), Tropospheric ozone during Mauna Loa Observatory Photochemistry Experiment 2 compared to long-term measurements from surface and ozonesonde observations, *J. Geophys. Res.*, *101*(D9), 14569–14580, doi:10.1029/95JD03004.
- Oltmans, S. J., B. J. Johnson, J. M. Harris, A. M. Thompson, H. Y. Liu, C. Y. Chan, H. Vömel, T. Fujimoto, V. G. Brackett, W. L. Change, J.-P. Chen, J. H. Kim, L. Y. Chang, and H.-W. Chang (2004), Tropospheric ozone over the North Pacific from ozonesonde observations, *J. Geophys. Res.*, *109*, D15S01, doi:10.1029/2003JD003466.
- Oltmans, S. J., A. S. Lefohn, J. M. Harris, I. Galbally, H. E. Scheel, G. Bodeker, E. Brunke, H. Claude, D. Tarasick, B. J. Johnson, P. Simmonds, D. Shadwick, K. Anlauf, K. Hayden, F. Schmidlin, T. Fujimoto, K. Akagi, C. Meyer, S. Nichol, J. Davies, A. Redondas, and E. Cuevas (2006), Long-term changes in tropospheric ozone, *Atmos. Environ.*, *40*, 3156–3173.
- Perry, K. D., and P. V. Hobbs (1994), Further evidence for particle nucleation in clear air adjacent to marine cumulus clouds, *J. Geophys. Res.*, *99*, 22,803–22,818.
- Perry, K. D., T. A. Cahill, R. C. Schnell, and J. M. Harris (1999), Long-range transport of anthropogenic aerosols to the National Oceanic and Atmospheric Administration baseline station at Mauna Loa Observatory, Hawaii, *J. Geophys. Res.*, *104*(D15), 18521–18533, doi:10.1029/1998JD100083.
- Price, S. and J. C. Pales (1963), Mauna Loa Observatory: The first five years, *Mon. Wea. Rev.*, *91*, 665–680.
- Ralph, F. M., P. J. Neiman, G. A. Wick, S. I. Gutman, M. D. Dettinger, D. R. Cayan, and A. B. White (2006), Flooding on California's Russian River: Role of atmospheric rivers, *Geophys. Res. Lett.*, *33*, L13801, doi:10.1029/2006GL026689.
- Ramanathan, V., P. J. Crutzen, J. T. Kiehl, and D. Rosenfeld (2001), Aerosols, climate, and the hydrological cycle, *Science*, *294*, 2119–2124, doi:10.1126/science.1064034.
- Rambo, J., C.-T. Lai, J. Farlin, M. Schroeder, and K. Bible (2011), On-site calibration for high precision measurements of water vapor isotope ratios using off-axis cavity-enhanced absorption spectroscopy, *J. Atmos. Oceanic Technol.*, *28*, 1448–1457, doi: <http://dx.doi.org/10.1175/JTECH-D-11-00053.1>.
- Ridley, B. A., E. L. Atlas, J. G. Walega, G. L. Kok, T. A. Staffelbach, J. P. Greenberg, F. E. Grahek, P. G. Hess, and D. D. Montzka (1997), Aircraft measurements made during the spring maximum of ozone over Hawaii: Peroxides, CO, O<sub>3</sub>, NO<sub>y</sub>, condensation nuclei, selected hydrocarbons, halocarbons, and alkyl nitrates between 0.5 and 9 km altitude, *J. Geophys. Res.*, *102*(D15), 18935–18961, doi:10.1029/97JD01345.
- Rieck M., L. Nuijens, and B. Stevens (2012), Marine boundary layer cloud feedbacks in a constant relative humidity atmosphere, *J. Atmos. Sci.*, *69*, 2538–2550.

- Risi, C., D. Noone, J. Worden, C. Frankenberg, G. Stiller, M. Kiefer, B. Funke, K. Walker, P. Bernath, M. Schneider, D. Wunch, V. Sherlock, N. Deutscher, D. Griffith, P. O. Wennberg, K. Strong, D. Smale, E. Mahieu, S. Barthlott, F. Hase, O. Garcia, J. Notholt, T. Warneke, G. Toon, D. Sayres, S. Bony, J. Lee, D. Brown, R. Uemura, and C. Sturm (2012), Process-evaluation of tropospheric humidity simulated by general circulation models using water vapor isotopologues: 1. Comparison between models and observations, *J. Geophys. Res.*, *117*, D05303, doi:10.1029/2011JD016621.
- Sayres, D. S., L. Pfister, T. F. Hanisco, E. J. Moyer, J. B. Smith, J. M. St. Clair, A. S. O'Brien, M. F. Witinski, M. Legg, and J. G. Anderson (2010), Influence of convection on the water isotopic composition of the tropical tropopause layer and tropical stratosphere, *J. Geophys. Res.*, *115*, D00J20 doi:10.1029/2009JD013100.
- Schmidt, M., K. Maseyk, C. Lett, P. Biron, P. Richard, T. Bariac, and U. Seibt (2010), Concentration effects on laser-based  $\delta^{18}\text{O}$  and  $\delta^2\text{H}$  measurements and implications for the calibration of vapour measurements with liquid standards, *Rapid Commun. Mass Spectrom.*, *24*, 3553-3561.
- Schuster, G. L., O. Dubovik, and B. N. Holben (2006), Angstrom exponent and bimodal aerosol size distributions, *J. Geophys. Res.*, *111*, D07207, doi:10.1029/2005JD006328.
- Sharp, Z. (2007), Principles of Stable Isotope Geochemistry, Pearson Prentice Hall, 344 pg.
- Sherwood, S. C., R. Roca, T. M. Weckwerth, and N. G. Andronova (2010), Tropospheric water vapor, convection, and climate, *Rev. Geophys.*, *48*, RG2001, doi:10.1029/2009RG000301.
- Sherwood, S. C., S. Bony, and J.-L. Dufresne (2014), Spread in model climate sensitivity traced to atmospheric convective mixing, *Nature*, *505*, 37-42, doi:10.1038/nature12829.
- Small, J. D., P. Y. Chuang, G. Feingold, and H. Jiang (2009), Can aerosol decrease cloud lifetime?, *Geophys. Res. Lett.*, *36*, L16806, doi:10.1029/2998GL038888.
- Steen-Larsen, H. C., S. J. Johnsen, V. Masson-Delmotte, B. Stenni, C. Risi, H. Sodemann, D. Balslev-Clausen, T. Blunier, D. Dahl-Jensen, M. D. Ellehøj, S. Falourd, A. Grindsted, V. Gkinis, J. Jouzel, T. Popp, S. Sheldon, S. B. Simonsen, J. Sjolte, J. P. Steffensen, P. Sperlich, A. E. Sveinbjörnsdóttir, B. M. Vinther, and J. W. C. Whilte (2013), Continuous monitoring of summer surface water vapor isotopic composition above the Greenland Ice Sheet, *Atmos. Chem. Phys.*, *13*, 4815-4828, doi:10.5194/acp-13-4815-2013.
- Stevens, B. (2002), Entrainment in stratocumulus topped mixed layers, *Quart. J. Roy. Meteorol. Soc.*, *128*, 2663-2690.
- Stevens, B. (2005), Atmospheric moist convection, *Annu. Rev. Earth Planet. Sci.*, *33*, 605-643, doi:10.1146/annurev.earth.33.092203.122658.

- Sturm, P., and A. Knohl (2010), Water vapor  $\delta^2\text{H}$  and  $\delta^{18}\text{O}$  measurements using off-axis integrated cavity output spectroscopy, *Atmos. Meas. Tech.*, *3*, 67-77.
- Sui, C.-H., X. Li, M.-J. Yang, and H.-L. Huang (2005), Estimation of oceanic precipitation efficiency in cloud models, *J. Atmos. Sci.*, *62*, 4358–4370, doi: <http://dx.doi.org/10.1175/JAS3587.1>.
- Sui, C.-H., X. Li, and M.-J. Yang (2007), On the definition of precipitation efficiency, *J. Atmos. Sci.*, *64*, 4506–4513, doi: <http://dx.doi.org/10.1175/2007JAS2332.1>.
- Sullivan, P. P., C.-H. Moeng, B. Stevens, D. H. Lenschow, and S. D. Mayor (1998), Structure of the entrainment zone capping the convective atmospheric boundary layer, *J. Atmos. Sci.*, *55*, 3042-3064.
- Tanweer, A., M. Gröning, M. van Duren, M. Jaklitsch, and L. Pöltenstein (2009), Stable isotope internal laboratory water standards: Preparation, calibration and storage, *Technical Procedure Note No. 43*, 12 pp., Isotope Hydrology Laboratory, International Atomic Energy Agency, Vienna, Austria.
- Thornton, D. C., A. R. Bandy, B. W. Blomquist, J. D. Bradshaw, and D. R. Blake (1997), Vertical transport of sulfur dioxide and dimethyl sulfide in deep convection and its role in new particle formation, *J. Geophys. Res.*, *102*(D23), 28501–28509, doi:10.1029/97JD01647.
- Träumner, K., Ch. Kottmeier, U. Corsmeier, and A. Wieser (2011), Convective boundary-layer entrainment: Short review and progress using doppler lidar, *Boundary-Layer Meteorol.*, *141*, 369–391, doi:10.1007/s10546-011-9657-6.
- Tremoy, G., F. Vimeux, O. Cattani, S. Mayaki, I. Souley, and G. Favreau (2011), Measurements of water vapor isotope ratios with wavelength-scanned cavity ring-down spectroscopy technology: new insights and important caveats for deuterium excess measurements in tropical areas in comparison with isotope-ratio mass spectrometry, *Rapid Commun. Mass Spectrom.*, *25*, 3469-3480.
- Tremoy, G., F. Vimeux, S. Mayaki, I. Souley, O. Cattani, C. Risi, G. Favreau, and M. Oi (2012), A 1-year long  $\delta^{18}\text{O}$  record of water vapor in Niamey (Niger) reveals insightful atmospheric processes at different timescales, *Geophys. Res. Lett.*, *39*, L08805, doi:10.1029/2012GL051298.
- Twomey, S. (1977), The influence of pollution on the shortwave albedo of clouds, *J. Atmos. Sci.*, *34*, 1149–1152.
- van Geldern, R., and J. A. C. Barth (2012), Optimization of instrument setup and post-run corrections for oxygen and hydrogen stable isotope measurements of water by isotope ratio infrared spectroscopy (IRIS), *Limnol. Oceanogr.: Methods*, *10*, 1024-1036, doi:10.4319/lom.2012.10.1024.

- Wang, L., K. K. Caylor, J. Camilo Villegas, G. A. Barron-Garfford, D. D. Breshears, and T. E. Huxman (2010), Partitioning evapotranspiration across gradients of woody plant cover: Assessment of a stable isotope technique, *Geophys. Res. Lett.*, *37*, L09401, doi:10.1029/2010GL043228.
- Wen, X.-F., X. Lee, X.-M. Sun, J.-L. Wang, Y.-K. Tang, S.-G. Li, G.-R. Yu (2012), Intercomparison of four commercial analyzers for water vapor isotope measurement, *J. Atmos. Oceanic Technol.*, *29*, 235-247.
- Wonaschuetz, A., A. Sorrosian, B. Ervens, P. Y. Chang, G. Feingold, S. M. Murphy, J. de Gouw, C. Warneke, and H. H. Jonsson (2012), Aerosol and gas re-distribution by shallow cumulus clouds: An investigation using airborne measurements, *J. Geophys. Res.*, *117*, D17202, doi:10.1029/2012JD018089.
- Wood, R., D. Leon, M. Lebsack, J. Snider, and A. D. Clarke (2012), Precipitation driving of droplet concentration variability in marine low clouds, *J. Geophys. Res.*, *117*, D19210, doi:10.1029/2012JD018305.
- Worden, J., K. Bowman, D. Noone, R. Beer, S. Clough, A. Eldering, B. Fisher, A. Goldman, M. Gunson, R. Herman, S. S. Kulawik, M. Lampel, M. Luo, G. Osterman, C. Rinsland, C. Rodgers, S. Sander, M. Shephard, and H. Worden (2006), Tropospheric Emission Spectrometer observations of the tropospheric HDO/H<sub>2</sub>O ratio: Estimation approach and characterization, *J. Geophys. Res.*, *111*, D16309, doi:10.1029/2005JD006606.
- Worden, J., D. Noone, K. Bowman, and TES Team Members (2007), Importance of rain evaporation and continental convection in the tropical water cycle, *Nature*, *445*, 528-532.
- Worden, J., D. Noone, J. Galewsky, A. Bailey, K. Bowman, D. Brown, J. Hurley, S. Kulawik, J. Lee, and M. Strong (2011), Estimates of bias in Aura TES HDO/H<sub>2</sub>O measurements at the Mauna Loa observatory, *Atmos. Chem. Phys.*, *11*, 4491-4503, doi:10.5194/acp-11-4491-2011.
- Worden, J., S. Kulawik, C. Frankenberg, V. Payne, K. Bowman, K. Cady-Peirara, K. Wecht, J.-E. Lee, and D. Noone (2012), Profiles of CH<sub>4</sub>, HDO, H<sub>2</sub>O, and N<sub>2</sub>O with improved lower tropospheric vertical resolution from Aura TES radiances, *Atmos. Meas. Tech.*, *5*, 397-411, doi:10.5194/amt-5-397-2012.
- Yang, Y., Y.-L. Chen, and F. M. Fujioka (2008), Effects of trade-wind strength and direction on the leeside circulation of the Island of Hawaii, *Mon. Wea. Rev.*, *136*, 4799-4818.
- Yokelson, R., S. Urbanski, E. Atlas, D. Toohey, E. Alvarado, J. Crouse, P. Wennberg, M. Fisher, C. Wold, T. Campos, K. Adachi, P. R. Buseck, and W. M. Hao (2007), Emissions from forest fires near Mexico City, *Atmos. Chem. Phys.*, *7*, 5569-5584.
- Yu, H., Y. J. Kaufman, M. Chin, G. Feingold, L. A. Remer, T. L. Anderson, Y. Balkanski, N. Bellouin, O. Boucher, S. Christopher, P. DeCola, R. Kahn, D. Koch, N. Loeb, M. S.

- Reddy, M. Schulz, T. Takemura, and M. Zhou (2006), A review of measurement-based assessments of the aerosol direct radiative effect and forcing, *Atmos. Chem. Phys.*, *6*, 613-666, doi:10.5194/acp-6-613-2006.
- Zhang J., and S. T. Rao (1999), The role of vertical mixing in the temporal evolution of ground-level ozone concentrations, *J. Appl. Meteorol.*, *38*, 1674-1691.
- Zhao, M. (2014), An investigation of the connections among convection, clouds, and climate sensitivity in a global climate model, *J. Climate*, *27*, 1845-1862, doi:10.1175/JCLI-D-13-00145.1.
- Zhu, Y., and R. E. Newell (1998), A proposed algorithm for moisture fluxes from atmospheric rivers, *Mon. Wea. Rev.*, *126*, 725–735, doi: [http://dx.doi.org/10.1175/1520-0493\(1998\)126<0725:APAFMF>2.0.CO;2](http://dx.doi.org/10.1175/1520-0493(1998)126<0725:APAFMF>2.0.CO;2).

## APPENDIX A

### Uncertainties related to calibration choices

Because statistical fitting choices can significantly affect the accuracy of bias corrections (see Chapter 3), a series of sensitivity tests was performed prior to conducting the analysis presented in Chapter 4. The control test—designated as 2D Surface (15) in Table A1—is the locally-weighted regression ultimately chosen to correct the MLO total isotopic bias. A second test—3D Surface (15)—added time as a third predictor and applied an additional concentration correction (once the predicted values from the 3-dimensional surface were subtracted from the data) to address remaining biases at low humidity. This test was designed to determine whether accounting for possible long-term drift significantly changes the scientific results presented. A third test—Sequential (15)—corrected the concentration dependence first (using a locally-weighted regression) and subsequently quantified the deviation from the VSMOW-SLAP scale using a simple linear regression [cf. *Steen-Larsen et al.*, 2013]. To minimize possible time-dependent biases, isotopic data were normalized in three-month segments. This third test was designed to evaluate if correcting the biases simultaneously or individually impacts the results. Finally, a fourth test—2D Surface (5)—investigated the importance of changing the data averaging time from 15 to 5 minutes. Otherwise, the statistical fitting procedure was the same as for the control.

Each calibration method was then used to generate a dataset from which strong convective events with either high or low precipitation efficiency could be identified (the selection procedure is discussed in the Methods and Results of Chapter 4). For each test, Table A1 shows the percentage of events selected by one method and shared with another. For all

pairings, the percentage of shared events is 90% or greater; and none of the large-scale composites or diurnal patterns presented in Chapter 4 changes qualitatively between tests. Thus, while uncertainties in the selection of high and low precipitation efficiency conditions may be at least 10%, the results presented throughout the chapter are robust. The advantage of the 2D Surface (15) method, which was ultimately selected to calibrate the ambient data, is that it involves a single calibration step (unlike the 3D Surface and Sequential methods), and it is computationally less intense than the 2D Surface (5) method.

**Table A1.** Percentage of the high or low precipitation efficiency events for the calibration methods listed in column 1 that are shared with methods in other columns.

	<b>2D Surface (15)</b>	<b>Sequential (15)</b>	<b>2D Surface (5)</b>
<b>3D Surface (15)</b>	89.7	94.3	89.9
<b>2D Surface (15)</b>	---	93.4	95.2